



**Politecnico
di Torino**

ScuDo

Scuola di Dottorato ~ Doctoral School

WHAT YOU ARE, TAKES YOU FAR

Doctoral Dissertation
Doctoral Program in Civil and Environmental Engineering (36th Cycle)

Next-Generation Microalgae Cultivation: Innovative flat panel photobioreactor with tailored light regulation and hybrid modelling approach

Michele Carone

Supervisors

Prof. Vincenzo A. Riggio, Supervisor

Prof. Mariachiara Zanetti, Co-Supervisor

Doctoral Examination Committee:

Prof. Tiziano Zarra, Università degli Studi di Salerno, Italy

Dr. Ulderico Di Caprio, Katholieke Universiteit Leuven, Belgium

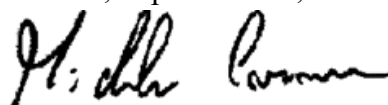
Politecnico di Torino
September 10, 2024

This thesis is licensed under a Creative Commons License, Attribution - Noncommercial - NoDerivative Works 4.0 International: see www.creativecommons.org. The text may be reproduced for non-commercial purposes, provided that credit is given to the original author.

I hereby declare that, the contents and organisation of this dissertation constitute my own original work and does not compromise in any way the rights of third parties, including those relating to the security of personal data.

Michele Carone

Turin, September 10, 2024

A handwritten signature in black ink, appearing to read 'Michele Carone', written in a cursive style.

Summary

The quest for sustainable microalgae production necessitates the development of advanced photobioreactor (PBR) systems that address current limitations in energy efficiency, light management, and process optimization. Microalgae offer immense potential as a sustainable resource, but existing PBR systems, particularly flat panel PBRs, are hampered by high energy costs and biofouling risks associated with traditional air bubbling methods for mixing. Additionally, the reliance on compressed air significantly contributes to the PBR's overall energy consumption. This research aims to enhance the technological efficacy and sustainability of PBRs through innovative design and advanced engineering solutions.

This PhD thesis introduces an innovative flat panel photobioreactor featuring a centrifugal pump-assisted hydraulic circuit designed to overcome these challenges. This design confines microalgae within a positive-pressurized serpentine directly exposed to artificial light, optimizing light distribution and enhancing growth efficiency. The flat panels, measuring 1.3 cm in width, are a critical feature that maximizes light penetration, essential for photosynthetic activity and biomass production. The research highlights the potential of this design for energy-efficient industrial applications, particularly in CO₂ bio-fixation.

An in-depth examination of the fluid dynamics within the new PBR reveals how the centrifugal pump-assisted hydraulic circuit influences microalgae movement and interaction. By optimizing hydrodynamic performance, the system aims to uniform exposure to light, thereby enhancing microalgae productivity. A key advancement in this work is the introduction of a tuneable LED lighting engine. Composed of 10 discrete LEDs covering the entire PAR range and 2 white light LEDs, this system allows for customized light spectra tailored to the specific needs of different microalgae species. This tailored lighting approach not only enhances microalgae growth by aligning with their photosynthetic requirements but also reduces energy consumption for artificial lighting.

Additionally, achieving a balance between high volumetric productivity and high biomass concentration is essential for PBR operations. This thesis presents a hybrid model approach developed using first-principle equations to streamline computational processes and reduce the need for extensive experimental data. The model was trained and validated with batch cultivations of the red microalga

Galdieria sulphuraria, grown under controlled conditions in the novel PBR. The precise control over process conditions, including light management and tailored spectra, demonstrated the model's robustness in predicting growth outcomes.

Lastly, as part of this PhD work, the technical feasibility of water reuse and nutrients recovery specifically for the cultivation of the polyextremophile *G. sulphuraria* is presented. This case study aims to demonstrate how these efforts can potentially yield significant resource savings and reduce environmental impact, thereby contributing to the advancement of sustainable practices in large-scale microalgae cultivation.

Overall, this thesis makes significant contributions to the field of microalgae cultivation by presenting an advanced PBR design with a detailed description of its fluid dynamics, enhancing light management, and developing a hybrid model for process optimization. This novel flat panel photobioreactor with a centrifugal pump-assisted hydraulic circuit and tailored LED lighting system demonstrates a promising pathway toward more efficient and sustainable microalgae production. Also, this PhD thesis lays the groundwork for future works focusing on the employment and refining of hybrid models as potent engineering tools to optimize microalgae cultivation processes, as well as emphasizing the importance of the freshwater footprint to ensure environmental compliance and maximize resource efficiency.

Acknowledgment

This work was financially supported by Politecnico di Torino and the Wearwe group @PoliTo (58_DIM21RIGVIN; 58_RCE19ZANMAR_03). The study presented in Chapter 5 is part part of the project NODES which has received funding from the MUR – M4C2 1.5 of PNRR funded by the European Union - NextGenerationEU (Grant agreement no. ECS00000036).

And I would like to express my gratitude to: Arcobaleno Cooperativa Sociale (Turin, Italy) in the person of Fabio Passarelli and Fabrizio De Bernardi for their technical support; Piero Santoro from MEG Science (Milan, Italy) for the realization of the LED lighting system; Dr. Andrea Occhipinti from Abel Nutraceuticals (Turin, Italy) for the technical assistance and insightful discussions; Prof. Marco Vanni and Dr. Graziano Frungieri (DISAT - PoliTo) for their huge assistance for the work described in Chapter 3; Prof. Mumin Enis Leblebici and Dr. Ulderico Di Caprio from KULeuven for the visiting opportunity and their guidance for the realization of the model described in Chapter 4; Prof. Alberto Tiraferri and Marco Malaguti (DIATI - PoliTo) for the immense contribution to the work presented in Chapter 5; Clara Derossi, Davis Alpe, Lorenzo Costamagna and Dr. Giovanna Zanetti (DIATI – PoliTo) for their incredible help in managing the microalgae collection, the PBR systems, and the experimental tests and setups; my co-supervisor Prof. Mariachiara Zanetti for her constant support; my supervisor Prof. Vincenzo A. Riggio for his contagious enthusiasm, guidance and unwavering belief in me.

*A Nicolò e Silvia,
la mia più grande forza*

Table of Contents

Chapter 1 - Large-scale Microalgae cultivation.....	1
1.1 Introduction.....	1
1.2 Light supply and availability	2
1.3 Nutrient supply	6
1.4 Culture conditions.....	7
1.5 Mixing and Gas Mass Transfer.....	7
1.6 Large-scale microalgae cultivation systems	10
1.6.1 Open systems	11
1.6.2 Photobioreactors	12
1.6.3 Flat Panel Photobioreactors	15
1.7 Modelling light-limited microalgae growth.....	19
1.7.1 Light absorption, Photosynthesis and Biomass Growth	23
1.7.2 Estimating Photobioreactor productivity	28
Chapter 2 - Design and characterization of a new pressurized flat panel photobioreactor for microalgae cultivation and CO₂ bio-fixation.	33
2.1 Introduction.....	33
2.2 Materials and Methods.....	36
2.2.1 The flat panel photobioreactor	36
2.2.2 Microalgae and cultivation conditions.....	38
2.2.3 Biomass concentration measurements	38

2.2.4	Hydraulic flow determination.....	39
2.2.5	CO ₂ mass transfer coefficient (k_{LaCO_2}).....	39
2.2.6	CO ₂ fixation yield	40
2.2.7	Mixing time.....	40
2.2.8	Energetic measurements	41
2.2.9	Radiance matrix	41
2.3	Results and discussion	41
2.3.1	Hydrodynamics flow description.....	41
2.3.2	Mixing characterization	43
2.3.3	CO ₂ mass transfer	44
2.3.4	Light homogeneity	47
2.3.5	Microalgae growth and CO ₂ bio-fixation efficiency	48
2.4	Conclusion	50
Chapter 3 - Advanced design and characterization of a flat panel photobioreactor equipped with a customizable LED lighting system.		52
3.1	Introduction.....	52
3.2	Materials and methods	55
3.2.1	The flat panel photobioreactor.....	55
3.2.2	LED lighting system	55
3.2.3	Computational Fluid Dynamics simulations setup	56
3.2.4	Microalgae-specific light spectra composition	59
3.2.5	Microalgae and cultivation conditions.....	60
3.2.6	Biomass concentration measurements	61

3.2.7	Radiance matrix	61
3.3	Results and discussion	61
3.3.1	CFD.....	61
3.3.2	Light spectra composition.....	67
3.3.3	Light homogeneity	70
3.3.4	Microalgae growth.....	71
3.4	Conclusion	73
Chapter 4 - Hybrid modelling of light-limited microalgae growth		76
4.1	Introduction.....	76
4.2	Materials and Methods.....	79
4.2.1	Batch cultivations	79
4.2.2	Sample measurements (C_x , $a_x/a_{x,\lambda}$).....	80
4.2.3	Elemental composition	80
4.2.4	Computational methods	80
4.2.5	a_x effect on model performances	83
4.3	Results and Discussion	84
4.3.1	<i>G. sulphuraria</i> elemental composition	84
4.3.2	Model training.....	84
4.3.3	Model analysis	89
4.4	Conclusion	93
Chapter 5 - Towards sustainable water management for <i>Galdieria sulphuraria</i> cultivation		95
5.1	Introduction.....	95

5.2	Materials and Methods.....	96
5.2.1	Microalgae growth and cultivation conditions	96
5.2.2	Microalgae harvesting methods	97
5.2.3	<i>C-PC</i> extraction and quantification	98
5.2.4	Macro- and micro-nutrients monitoring	98
5.3	Results and Discussion	98
5.3.1	Microalgae cultivation in partially reused water (25%)	98
5.3.2	Microalgae cultivation with highest recovered water volume	101
5.3.3	Analysis of water reuse energy consumption	105
5.3.4	Biomass quality and environmental benefits of water reuse	108
5.4	Conclusion	110
	Chapter 6 - General conclusion and future perspectives	112
	References.....	115
	Appendix.....	136

List of Figures

Figure 1: Emission spectra of different light sources: sun daylight, incandescent bulbs, fluorescent lamps, halogen lamps, and Light Emitting Diodes (LEDs).	4
Figure 2: Typical Photosynthesis-Irradiance response curve of microalgae. I_k = constant irradiance; I_s = saturation irradiance; I_i = inhibition irradiance.	5
Figure 3: Examples of different types of open systems for outdoor microalgae cultivation.	11
Figure 4: Schematic drawing of a raceway pond.....	12
Figure 5: Examples of different types of closed systems for both indoor and outdoor microalgae cultivation.....	13
Figure 6: Schematic drawing of serpentine (bottom right), spiral (top right), and helical (left) photobioreactors.....	14
Figure 7: Schematic drawing of an airlift flat panel photobioreactor.....	16
Figure 8: Simplified diagram of the chloroplast and the photosynthetic reactions.	20
Figure 9: Representation of most important specific consumption and production rates for the quantitative analysis of photoautotrophic growth.....	22
Figure 10: Wavelength specific absorption cross section of a sample of <i>G. sulphuraria</i> 074W taken from an autotrophic culture at Politecnico di Torino. ...	24
Figure 11: Example of the specific rate of photosynthesis a function of photon flux density I_{ph} according to the model of Jassby & Platt..	26
Figure 12: Example of the specific growth rate μ of a microalga as a function of photon flux density I_{ph} . The specific growth rate is derived from Pirt's law in combination with the photosynthesis models of Jassby & Platt.....	27
Figure 13: Example of a light (I_{ph}) penetration pattern in a microalgal culture as function of depth z	29
Figure 14: Schematic representation of the flat panel photobioreactor. A) 3D isometric view of the whole PBR. B) Schematic view of the mixing tank.	36

Figure 15: Schematic process diagram of the flat panel photobioreactor.....	37
Figure 16: Influence of liquid flow velocity on mixing time..	44
Figure 17: Graphical representation of the light intensity in a 3D space of the fluorescent source.	48
Figure 18: Biomass concentration of <i>Acutodesmus obliquus</i> in the flat panel photobioreactor.	50
Figure 19: The alveolar flat-panel PBR. A. 3D isometric representation of the PBR. B. Schematic representation of the lighting engine.	55
Figure 20: Visualization of the flow field in the mixing tank, by a contour plot representation of the velocity magnitude field and by fluid path lines. Three cross sections are reported together with a 3D representation.....	62
Figure 21: Visualization of the flow field in the flat panel. A. Velocity magnitude contour plot. B. Fluid path lines. C. Arrow representation of the flow field.....	64
Figure 22: Results of the tracer experiments. Top) Concentration contour plot at three subsequent times for the case of a step release from the inlet. Centre) Concentration at the outlet as a function of time for the two modes of release. Bottom) Concentration contour plot at three subsequent times for the case of a step release from the liquid-free surface.	66
Figure 23: Residence time distributions measured at the halfway of the length of each channel of the alveolar flat panel as obtained by an impulse tracer experiment.	67
Figure 24: Light spectra customization. A. Wavelength-specific normalized oxygen evolution response of <i>A. obliquus</i> . B. Resultant final spectrum employed for <i>A. obliquus</i> . C. Wavelength-specific normalized oxygen evolution response of <i>G. sulphuraria</i> . D. Resultant final spectrum employed for <i>G. sulphuraria</i>	69
Figure 25: Graphical representation of the light intensity in a 3D space of the LEDs lighting source. A. Light intensity distribution for the light spectrum employed for <i>A. obliquus</i> . B. Light intensity distribution for the light spectrum employed for <i>G. sulphuraria</i>	71
Figure 26: Photoautotrophic batches. A. Biomass concentration of <i>Acutodesmus obliquus</i> in the flat panel photobioreactor. B. Biomass concentration of <i>Galdieria sulphuraria</i> in the flat panel photobioreactor.	73

Figure 27: Hybrid model performances of three representative batches of the test set. A. The best obtained prediction. B. The worst obtained prediction. C. The on-average obtained prediction.	85
Figure 28: MAPE, MAE and R^2 box plots of the hybrid model performances for the train (white) and test (grey) data sets.	88
Figure 29: The trend of the specific sugar consumption rate for maintenance (m_s) as function of the biomass concentration C_x as described by Eq. 4.9.	89
Figure 30: Comparison of the model prediction implementing the adaptive m_s (orange line) and the predictions assuming a constant m_s value within the literature-reported range (grey region)..	90
Figure 31: Contour plot of the hybrid model derived growth rate (μ) as a function of biomass concentration (C_x) and the incident light intensity ($I_{ph}(0)$).....	91
Figure 32: Hybrid model derived growth rate (μ) sensitivity with a_x and averaged incident light intensity ($I_{ph}(0)$), assuming a_x stochastic behavior with uniform probability in the range [min = 1.4, max = 2.2 $m^2 mol_x^{-1}$].	92
Figure 33: Biomass concentration measured over time during cultivation. A. Cycles of partially reused water from centrifugation. B. Cycles of partially reused water from membrane microfiltration..	100
Figure 34: Water flux across the microfiltration membrane as a function of water recovery values. The reported water flux values were measured upon reaching flux stabilization for each recovery value	101
Figure 35: Biomass concentration over time during cultivation in reused water.	103
Figure 36: Measured water flux (y-axis) during microfiltration reported against time(x-axis).....	104
Figure A.1: Detailed view of the geometry of the mixing tank.....	136
Figure A.2: Qualitative representation of the flat panel.	137
Figure A.3: Fluorescence microscopy images of <i>A. obliquus</i> and <i>G. sulphuraria</i>	137
Figure A.4: Schematic diagram of the developed model.....	139

List of Tables

Table 1: Overview of the main microalgae cultivation systems.....	17
Table 2: Variation of hydraulic flow rates according to the manually chosen level of the hydraulic circulator and the CO ₂ flow injection.....	42
Table 3: Dependency of CO ₂ gas-liquid mass transfer coefficient (k_{La}) on the liquid flow velocities and CO ₂ flow rates tested.....	46
Table 4: Predictions and errors' metrics of the reported representative batches of the test set.....	86
Table 5: Concentration of metals and ions in the culture medium in different solutions, before and after cultivation, before and after water recovery with centrifugation or microfiltration.....	102
Table 6: <i>G. sulphuraria</i> C-PC accumulation as % weight/weight at the end of each cultivation cycle.....	109
Table A.1: Product performances of LUXEON CZ Colours at current 350 mA and junction Temperature 85°C.....	138

Scientific contributions and publications

The research described in this doctoral dissertation has been shared with the scientific community through the following scientific publications in peer-reviewed journals:

Chapter 2:

Carone, M.; Alpe, D.; Costantino, V.; Derossi, C.; Occhipinti, A.; Zanetti, M.; Riggio, V. A. Design and Characterization of a New Pressurized Flat Panel Photobioreactor for Microalgae Cultivation and CO₂ Bio-Fixation. *Chemosphere* **2022**, *307*. <https://doi.org/10.1016/j.chemosphere.2022.135755>.

Chapter 3:

Carone, M.; Frungieri, G.; Costamagna, L.; Zanetti, M.; Vanni, M.; Riggio, V. A. Advanced Design and Characterization of a Flat Panel Photobioreactor Equipped with a Customizable Light-Emitting Diode Lighting System. *ACS Sustainable Chemistry & Engineering* **2024** *12* (7), 2550-2562. <https://doi.org/10.1021/acssuschemeng.3c05176>

Chapter 5:

Carone, M.; Malaguti, M.; Zanetti, M.; Tiraferri, A.; Riggio, V. A. Towards sustainable water management for *Galdieria sulphuraria* cultivation. *Science of The Total Environment* **2024**, *950*, 175267. <https://doi.org/10.1016/j.scitotenv.2024.175267>

Chapter 1

Large-scale Microalgae cultivation

1.1 Introduction

Microalgae, a diverse group of photosynthetic organisms, have emerged as key players in sustainable development, harnessing their ability to sequester carbon dioxide and convert solar energy into valuable chemical compounds^{1,2}. The cultivation of microalgae as a sustainable process brings numerous advantages to different industrial sectors³. Indeed, the growth requirements of microalgae such as carbon dioxide, light, and water, target the most prominent industrial processes in which environmental impacts and renewable energy generation are of great concern. During the 1970's the importance of finding alternative energy sources instead of fossil fuels attracted global interest towards biological applications of solar energy⁴. Microalgae require sunlight for photosynthesis and the quality of light can significantly influence the synthesis of their biochemical compounds. Furthermore, increased awareness regarding waste disposal hazards and environmental pollution can be linked to the development of microalgae production technologies. Wastewater industry could potentially benefit from the use of microalgae. Depending on the species, microalgae can absorb various heavy metals and toxic components, and the wastewater can be used as culture media bringing advantages to the renewable energy sector. Microalgae are also potential sources of high-value components such as natural pigments, polyunsaturated fatty acids, proteins, and polysaccharides that are widely used in food, pharmaceutical and cosmetics industries³. This diverse range of applications necessitates a tailored approach, acknowledging the distinctive characteristics inherent to the different microorganisms.

Microalgae and cyanobacteria are very diverse groups of organisms with under-explored and under-valued potential. There are thousands of species that thrive in marine, freshwater, and even terrestrial environments. A conservative estimate is that there are 44,000 scientifically described microalgal and cyanobacterial species⁵. This vast number of species naturally encompasses diversity in biochemical

compounds as well. Environmental conditions also alter the biochemical composition and trigger the production of certain compounds, which means that the total biochemical potential for commercial exploitation is very high ⁶. These two groups are categorically different (e.g., microalgae are eukaryotic while cyanobacteria are prokaryotic). However, since microalgae and cyanobacteria are both groups of organisms with the capacity to perform photosynthesis, in the realm of applied phycology the cultivation principles and challenges overlap. Therefore, from a technical perspective, both groups can be grown in photobioreactors and ponds, however often with a variation in specific cultivation conditions.

Essential prerequisites for successful phototrophic microalgae-based processes include the provision of light and nutrients (carbon, nitrogen, phosphorus, etc.), the maintenance of optimal culture conditions (pH, temperature), the effective mixing to prevent parameter gradients that could diminish biological system yield ^{7,8}, and an adequate carbon dioxide supply and oxygen removal. A comprehensive understanding and precise manipulation of these parameters are imperative for the successful large-scale cultivation of microalgae, holding substantial implications for diverse industrial applications, although it poses greater challenges, especially concerning cost-effectiveness ^{9,10} and energy requirements.

1.2 Light supply and availability

The growth and productivity of photosynthetic microorganisms hinge on the availability and effective utilization of light, their primary energy source for photosynthesis. Achieving optimal light supply is critical for maximizing productivity, but careful consideration is necessary to avoid damage to the photosynthetic apparatus, especially under conditions of suboptimal temperature or high oxygen levels ¹¹.

In a scientific context, light is defined as electromagnetic radiation across all wavelengths, but for the visible spectrum (400-700 nm), it is commonly referred to as visible light. Microalgae utilize light across this entire visible range, called the *Photosynthetically Active Radiation* (PAR), although the sensitivity of microalgae for visible light of a specific wavelength differs dramatically from the human eye's heightened sensitivity to green light (555 nm). Consequently, the use of radiometric units (Watt) instead of photometric units (lumen) is essential in photosynthesis research to accurately represent the energy absorbed by microalgae, since the lumen is weighed by the sensitivity of the human eye. The conversion from radiant flux (*watt*) to photon flux ($mol_{ph} s^{-1}$) is governed by the Planck-Einstein relation.

Photosynthesis is a quantum process, and the actual absorption of quanta or photons by the microalgal photosystems sets in motion the cascade of reactions ultimately resulting in growth. As such, the radiant flux in Watts, $W = J s^{-1}$, is usually converted into a photon flux in $mol_{ph} s^{-1}$ employing the Planck-Einstein relation ($E = h \cdot \nu$). Nevertheless, all the light meters currently employed in photosynthesis research are adapted to immediately give the photon flux density in $mol_{ph} m^{-2} s^{-1}$ within the PAR wavelength range.

While sunlight serves as the natural source of light energy outdoors, the use of artificial light has emerged as an attractive option for cultivating algae, especially in the production of high-value compounds, a sort of “precision agriculture” for algae. Using sunlight as a light source is advantageous due to its cost-effectiveness and abundant availability, with approximately 42-43% of the sun's radiant flux reaching Earth falling within the PAR range. However, it comes with drawbacks such as location-specific day/night cycles, with the associated important changes of light intensity during day hours, unpredictable weather, and seasonal variations. On the other hand, the implications of employing artificial light extend beyond economic considerations and encompass energy-related factors. The conversion of electricity into photons results in substantial energy losses, amounting to 65% or more, depending on the specific light source utilized. Furthermore, the entire electrical demand must be generated, introducing an additional energy component. Various types of lamps are available for microalgae research, with the predominant choices being fluorescent tubes and light-emitting diodes (LEDs). LEDs offer numerous advantages compared to fluorescent tubes, such as lower heat dissipation, resulting in reduced energy consumption, and a narrow emission spectrum, just to cite a few^{12,13}. LEDs with luminous efficacy of 80 – 150 $lm W^{-1}$ (7 – 17 $mol_{ph} s^{-1} W^{-1}$) are largely available in the market. Combinations of monochromatic LEDs can also be used to produce specific spectra that may be completely utilized by the plants, thus making the useful luminous output equivalent to the total luminous output. Further, due to rapid advancements in LED lighting technology, it is expected that LEDs with an efficacy of $> 200 lm W^{-1}$ ($> 23 mol_{ph} s^{-1} W^{-1}$) will be developed within the next few years. The power requirement of a typical LED is 10–100 times less than most conventional lamps, thus making LED lamps highly cost-effective.

Despite advancements in LED lighting and improved photosynthetic efficiency, the incorporation of artificial light comes with additional costs. According to Blanken and co-authors¹⁴, the combined expenses for investing in lamps and the associated power consumption contribute approximately \$16 to the production

costs per kilogram of dry biomass. Given the negative energy balances, the electrical energy required for microalgae cultivation employing artificial light should be generated as ‘green’ energy instead of that derived from exploiting fossil fuels ¹⁴, or alternatively be used in compensation of sunlight to ensure a 24h production. By employing continuous and controlled illumination, productivity can be enhanced, as biomass is not lost during night-time periods ^{14,15}.

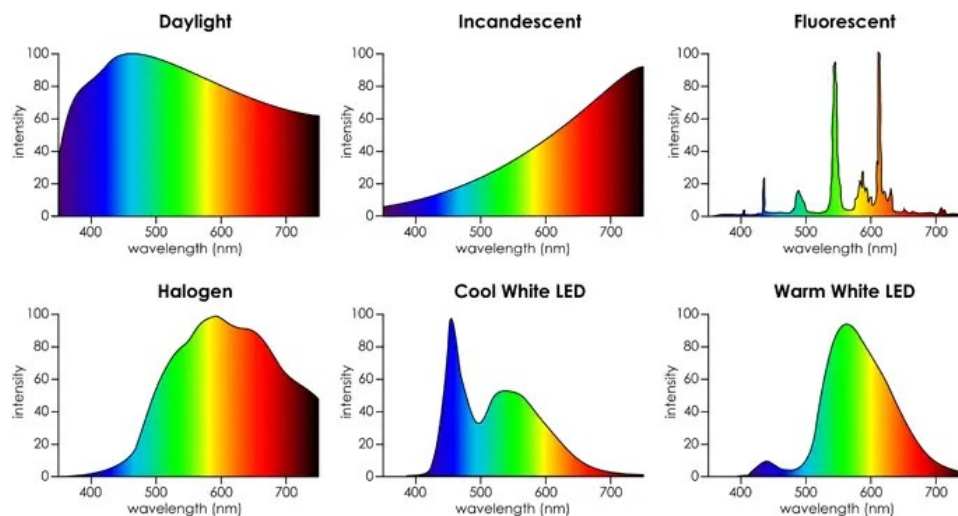


Figure 1: Emission spectra of different light sources: sun daylight, incandescent bulbs, fluorescent lamps, halogen lamps, and Light Emitting Diodes (LEDs).

Figure 1 illustrates the spectral distribution of some of these lamps, with a focus on the photosynthetically active radiation (PAR, 400-700 nm) range. All spectra are normalized to ensure unity in the integral photon flux density over the PAR range. Despite the very different spectral profiles of the different lamps and the sunlight, the photosynthesis can still be fueled by any photon within the PAR range. However, certain spectral effects cannot be ruled out, as demonstrated by studies showing the influence of light colour on phenomena such as the timing of cell division ¹⁶.

Light availability in microalgal cultivation is influenced by various factors, including the geometric and orientational design of the cultivation system ^{17,18}. Microalgal growth is directly linked to the photosynthesis rate, which, in turn, relies on the irradiance to which cells are exposed, regardless of the light source

employed, whether it be lamps, LEDs, or sunlight. However, achieving homogeneous irradiance within microalgae cultures presents challenges due to mutual shading, resulting in a spatial attenuation of light as function of its intensity, culture depth, and biomass concentration. Thus, cells in the outer part of the culture can be exposed to high irradiances, whereas in the inner part of the culture, cells can be in complete darkness. To address this, the concept of average irradiance was introduced by Fernandez-Sevilla *et al.*, 1998, enabling the calculation of the volumetric integral of irradiance across the entire culture¹⁹. This average irradiance serves as a crucial parameter for analyzing and modeling microalgal growth. Indeed, microalgae growth-irradiance response curves show a hyperbolic shape (Figure 2)^{19–21}, like those growth-substrate concentration curves used for bacteria or heterotrophic microorganisms.

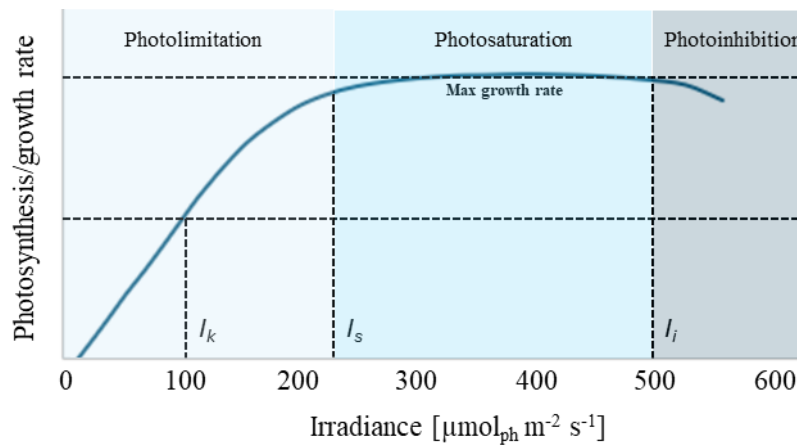


Figure 2: Typical Photosynthesis-Irradiance response curve of microalgae. I_k = constant irradiance; I_s = saturation irradiance; I_i = inhibition irradiance. Adapted from Tredici, 2010²².

In this curve the saturation irradiance (I_s) is the irradiance above which the growth is saturated, whereas constant irradiance (I_k) is the irradiance at which the growth is equal to half of the maximal specific growth rate. At very high irradiance the photosynthetic apparatus can be partially impaired and the photosynthesis rate decreases. The culture is then said to be photoinhibited. This irradiance is called the inhibition irradiance (I_i). For most microalgae, photosynthesis is saturated at $200 \mu\text{mol} \text{m}^{-2} \text{s}^{-1}$, although the maximal productivity is obtained at average irradiance values close to the I_k in the range of $50\text{--}100 \mu\text{mol}_{ph} \text{m}^{-2} \text{s}^{-1}$. Photoinhibition appears at irradiances over $500 \mu\text{mol}_{ph} \text{m}^{-2} \text{s}^{-1}$ in most strains, although some sensitive strains are photoinhibited at irradiances slightly higher than $300 \mu\text{mol}_{ph} \text{m}^{-2} \text{s}^{-1}$ ⁷. The influence of light on the growth of any strain must be studied in each particular

case. In this PhD work, instead of the average irradiance, the photosynthetic production has been volumetrically integrated across the culture as a function of the light attenuation for modeling purposes, as it will be described in section 1.7 of this introduction and following the methodology described in **Chapter 4**.

1.3 Nutrient supply

Microalgae biomass primarily consists of carbon (30%–50% dry weight (d.wt.)), oxygen (30%–50% d.wt.), hydrogen (3%–7% d.wt.), nitrogen (4%–9% d.wt.), phosphorus (1%–3% d.wt.), and minor elements such as sulphur, potassium, magnesium, and calcium. To optimize culture performance, the culture medium must incorporate these nutrients. Various culture media recipes, including f/2, Algal, BBM, BG11, Zarrouk, and Mann & Myers, have been proposed during the years²³. The approximate molecular formula of the microalgae biomass is $C O_{0.48} H_{1.83} N_{0.11} P_{0.01}$ ¹ and it can be used as estimation for minimal nutritional requirements²⁴. Nevertheless, the exact requirements of whatever microalgae culture can be determined by knowing the biomass productivity and the elemental composition of the biomass. Still, the supply of the exact calculated amount of nutrients could eventually lead to nutrient limiting conditions, which can reduce cell productivity. It is widely accepted that process operation under nutrient excess conditions allows maximizing the productivity of the cultures, and the determination of nutrient excess should adhere to economic and sustainability criteria, as nutrients in excess are usually released and lost from the system unless the cultivation medium is recirculated⁷. All nutrients must be supplied in dissolved form as microalgae thrive in aqueous media. The carbon is generally supplied as CO₂ gas, but only the part efficiently transferred to the liquid phase is available for the cells. Indeed, in the liquid phase the CO₂ reacts to form carbonic acid, bicarbonate, or carbonate based on the medium pH. Avoiding CO₂ shortage is crucial to maintain microalgae photosynthetically active. Alternatively, the carbon can be directly supplied as bicarbonate or carbonate. Microalgae acquire oxygen and hydrogen from the provided salts, with molecular oxygen being also generated in the process of photosynthesis. Elevated levels of O₂ beyond air saturation (0.2247 molO₂ m⁻³ at 20°C) could potentially impede photosynthesis in numerous microalgal species. Moreover, high O₂ concentrations, when coupled with intense irradiance, has the potential to induce severe photooxidation, as indicated by numerous studies^{25,26}. Nitrogen sources include urea, nitrate, or ammonium, with nitrate being a common choice. Although ammonium uptake is thermodynamically more favorable for microalgae than nitrate uptake, ammonium has been reported to

be toxic at concentrations exceeding 100 mg L^{-1} ²⁷. Phosphorus is usually supplied as phosphate, avoiding calcium phosphate due to its low solubility and potential precipitation in the culture medium.

In response to the challenges of high freshwater demand and its associated costs in microalgae cultivation, as well as the need to manage nutrient excess according to economic and sustainability criteria, **Chapter 5** of this PhD thesis investigates the technical feasibility of water reuse and nutrients recovery specifically for the red microalga *Galdieria sulphuraria* cultivation as a case study.

1.4 Culture conditions

Optimal culture conditions are essential for microalgae growth, with pH and temperature being crucial variables. Photobioreactors must be designed to control these factors effectively^{25,28}. Microalgae typically thrive in a neutral to slightly alkaline pH range (7.0–10.0), although some species tolerate acidic values below 3.0. Controlling pH is often achieved by dosing acid/alkaline buffers. Despite this is the predominant practice, a less prevalent method within the field, requiring a finer regulation and equipment, involves the control of pH through the injection of CO₂, concurrently supporting carbon supply. Temperature influences growth, with the optimal range being 20°C to 35°C for most cultivated microalgae. Heat absorption from the light source can lead to increased temperature, and adequate control mechanisms are necessary to prevent overheating, especially in large-scale outdoor reactors. Water spray and heat exchangers are common methods to avoid overheating, considering factors like air humidity and location-specific conditions^{29,30}.

1.5 Mixing and Gas Mass Transfer

Effective turbulence within microalgae cultures is imperative to mitigate gradients that could hinder cell performance. Mixing plays a pivotal role in reducing nutrient gradients, preventing cell sedimentation, and facilitating the movement of cells between light and dark zones, thereby enhancing photosynthesis³¹. Different methods, such as air bubbling, stirring, or liquid circulation through pumps, can achieve culture mixing. However, the energy invested in mixing comes with a cost that needs careful optimization and strategic considerations. Excessive mixing may lead to cell damage and hinder overall culture growth. Factors influencing shear sensitivity include the microalgae type, cell wall composition and thickness, intensity and nature of shear stress, and the adequacy of culture conditions (pH,

temperature, irradiance, etc.)³¹. Aerating cultures with air can cause cell damage during bubble ejection, breakup, coalescence, or bursting at the culture surface. Small bubbles are more damaging than larger ones, and controlling the air flow rate is crucial. Recommended values for whatever aerated photobioreactor are below $0.1 \text{ v } \text{v}^{-1} \text{ min}^{-1}$. Additionally, the use of surface tension agents like carboxymethyl cellulose can reduce shear stress-associated damage. Mechanical stirring and the use of devices like paddle wheels and pumps can also stress cells based on their type and speed. Shear rate and stress depend on factors such as the frequency of revolutions, impeller diameter, Reynolds number, and friction coefficient. Turbulence within the liquid bulk, determined by the energy supplied, is critical; the length scale of micro eddies relative to cell size can either cause damage or safely transport cells based on energy dissipation per unit of mass. An essential aspect of mixing in microalgae cultures is its impact on the light/dark regime or frequency to which cells are exposed. Studies indicate that exposing cells to saturating light at frequencies higher than 1 Hz allows light integration, maximizing light use efficiency by the cells³². While demonstrated at the laboratory scale in diluted cultures, achieving light integration in large-scale reactors poses challenges. Reducing culture depth and increasing liquid velocity may support light integration, but these conditions limit system volume and complicate process scale-up³³.

Apart reducing nutrient gradients and preventing cell sedimentation, enhancing the mass transfer capacity of any cultivation system is a crucial aspect to be optimized. For autotrophic growth, efficient supply of CO_2 and removal of O_2 are critical. The mass transfer capacity (N) between a gas and liquid phase involves three variables: the volumetric global mass transfer coefficient ($k_L a$), the driving force, and volume of the system (V) (Eq. 1.1). Dissolved oxygen accumulation has adverse effects, and values above 250% Sat. can decrease biomass productivity, and maintaining optimal levels is critical for culture productivity. The driving force for O_2 is the difference between the dissolved O_2 concentration within the culture and that in equilibrium with the gas in contact with the liquid (O_2^*), typically air, as described by the Henry's law (Eq. 1.2). Throughout the microalgae growth, photosynthesis occurs ($R\text{O}_2$), resulting in the production and accumulation of oxygen within the liquid ($d[\text{O}_2]/dt$). Should the rate of removal be insufficient to counterbalance the generation via photosynthesis, then dissolved oxygen will be accumulated as a function of light irradiance and mass transfer capacity of the system. A mass balance enables the establishment of the interrelation between these processes (Eq. 1.3)⁷.

$$N_{O_2} = k_L a_{O_2} \cdot ([O_2] - [O_2^*]) \cdot V_l \quad (1.1)$$

$$[O_2^*] = P_T \cdot H_{O_2} \cdot y_{O_2} \quad (1.2)$$

$$V_l \cdot \frac{d[O_2]}{dt} = R_{O_2} - k_L a_{O_2} \cdot ([O_2] - [O_2^*]) \cdot V_l \quad (1.3)$$

where P_T is the total pressure of the gas phase in contact with the liquid, H_{O_2} the Henry's law constant for oxygen, and y_{O_2} the mole fraction of oxygen in the gas phase.

The CO_2 transfer capacity (N_{CO_2}) is characterized by equations akin to those delineated for oxygen transfer, and thus function of the CO_2 mass transfer coefficient ($k_L a_{CO_2}$), the driving force, and the liquid volume (V_l) (Eq. 1.4). The driving force is likewise influenced by the CO_2 concentration in the liquid phase, in equilibrium with the gas phase (CO_2^*), as defined by Henry's law (Eq. 1.5). However, CO_2 concentration in the culture is influenced by the presence of a carbonate/bicarbonate buffer, and therefore is dependent on the total inorganic carbon (TIC) and the pH, considering the equilibrium constants K_1 and K_2 (Eq. 1.6). A net balance may also be employed to ascertain the accumulation of carbon dioxide, considering the photosynthesis rate (R_{CO_2}) and mass transfer (Eq. 1.7).

$$N_{CO_2} = k_L a_{CO_2} \cdot ([CO_2] - [CO_2^*]) \cdot V_l \quad (1.4)$$

$$[CO_2^*] = P_T \cdot H_{CO_2} \cdot y_{CO_2} \quad (1.5)$$

$$[CO_2] = \frac{[TIC]}{1 + \left(\frac{k_1}{[H^+]}\right) + \left(\frac{k_1 \cdot k_2}{[H^+]^2}\right)} \quad (1.6)$$

$$V_l \cdot \frac{d[CO_2]}{dt} = R_{CO_2} - k_L a_{CO_2} \cdot ([CO_2] - [CO_2^*]) \cdot V_l \quad (1.7)$$

where H_{CO_2} is the Henry's law constant for carbon dioxide, and y_{CO_2} the mole fraction of CO_2 in the gas phase.

The CO_2 mass transfer coefficient can be correlated with the oxygen mass transfer coefficient using the diffusivity ratio of both compounds in water (0.91). Notably, substantial differences arise in the driving force for mass transfer. Specifically, while Henry's constant for O_2 stands at $1.07 \text{ mol m}^{-3} \text{ atm}^{-1}$, for CO_2 it is 33.8 mol

$m^{-3} atm^{-1}$, indicating CO₂'s 30-fold higher solubility compared to O₂. Furthermore, the partial pressure of O₂ in air is 0.21 *atm*, whereas when pure CO₂ is used, it rises by 20-fold to 1.0 *atm*. This partial pressure diminishes when utilizing flue gases proportionate to the molar fraction of CO₂.

Achieving optimal CO₂ concentration is crucial for maximizing microalgae productivity. Supplying CO₂ is usually preferred, with flue gases used to reduce production costs. Optimizing CO₂ supply systems to maximize dissolution and minimize release to the atmosphere is essential, and operating on-demand CO₂ injection at a controlled pH is recommended to improve CO₂ utilization efficiency.

1.6 Large-scale microalgae cultivation systems

Microalgae cultivation is the core of a long trajectory of research, innovation, and development in the field of microalgal biotechnology. Historically, open culture systems, known as raceway ponds, have been developed on small and large scales since the mid-1950s. However, given the rise in the exploitation of microalgal biomass, these cultivations have not been able to compete with the global demand for biomass. Therefore, the search for vigorous research initiatives for new alternatives that alleviated the exclusive dependence on open systems was necessary³⁴. Faced with this scenario, photobioreactors emerged as a potentially viable alternative to serve the microalgal market demands. However, given the complexity of establishing an ideal model, the state of the art in photobioreactor technologies covers a wide range of geometric configurations, each with different benefits and disadvantages³⁵. While numerous photobioreactor designs exist, none are universally optimal or adopted as commercial standard. Consequently, the starting point for any microalga-based process is the establishment of the biological system's requirements to inform the design of the most suitable photobioreactor.

Photobioreactors fall into two primary categories: open and closed systems. Open systems, such as ponds, tanks, raceways, and thin-layer platforms, interact directly with the environment. Closed systems, comprising bubble columns, tubular loops, and flat panels, maintain no direct contact between the culture and the atmosphere.

1.6.1 Open systems

Currently, open systems offer a cost-effective means of producing biomass, being significantly cheaper than closed systems³⁶ (Fig. 3). Open systems present advantages like easy cleaning, direct sun exposure, self-cooling through evaporation, and reduced oxygen accumulation released into the atmosphere. However, they are weather-dependent, prone to microbial contamination, incur high CO₂ losses, and demand more significant space compared to closed systems. Despite these drawbacks, their construction cost is approximately one order of magnitude lower than that of closed systems³⁷. Open cultivation units are limited to a select group of robust microalgae strains (*e.g.*, *Chlorella*, *Scenedesmus*), characterized by rapid growth or thriving under specific conditions (*e.g.*, *Arthrospira*, *Dunaliella*). Conversely, closed photobioreactors, offering controlled environments with minimized contaminants, accommodate a broader range of strains. Consequently, closed systems are conducive to cultivating sensitive strains like *Haematococcus pluvialis*, *Isochrysis galbana*, and *Porphyridium cruentum*, among others⁷.

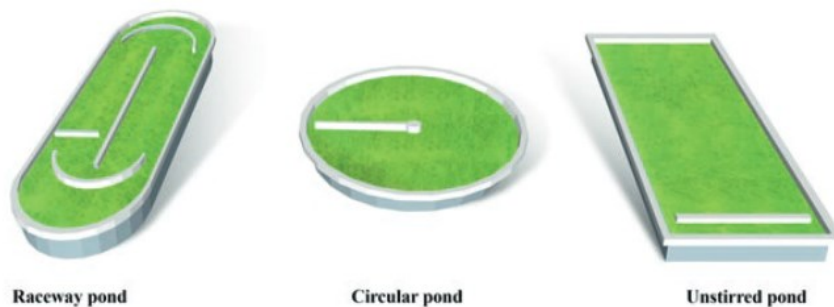


Figure 3: Examples of different types of open systems for outdoor microalgae cultivation. Adapted from Zerrouki and Henni, 2019³⁸.

The raceway pond (Fig. 4) is the most used design, which is a rectangular area divided into several channels with oval shapes³⁹. The pivotal factor in raceway design is the total area, which ranges from 100 to 5000 m². Larger facilities are created by multiplying the number of ponds, and the total surface is divided into two or four channels for culture recirculation. Channel length is proportional to width, typically with ratios of 10–20, favouring lower length/width ratios to minimize head losses and bends. Water channel depths fall within the range of 0.2–0.4 m. Higher water depths result in reduced light penetration and lower biomass concentration during continuous operation. Operating at lower water layers is recommended to enhance light penetration, biomass concentration, and culture

stability. The surface-to-total-volume ratio in these systems is generally low ($S_f/V = 5\text{--}10\text{ m}^{-1}$), and the total volume is calculated by multiplying the total area by the culture layer depth. Baffles are recommended in bends to minimize pressure drop, and sumps, often integrated into the channel, can be utilized for gas bubbling to supply CO_2 or remove O_2 .

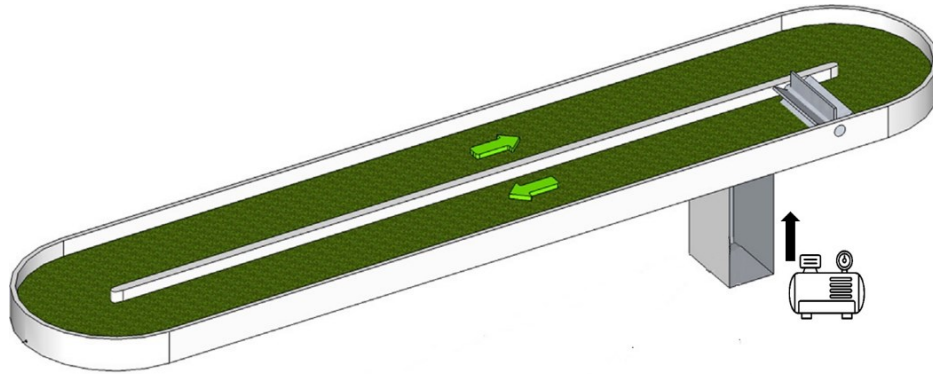


Figure 4: Schematic drawing of a raceway pond. A raceway reactor typically features two channels linked by bends, through which water is circulated with the help of a paddle wheel. The system often includes a sump for gas bubbling, and the bends are designed to minimize head loss. This setup can be scaled up by combining two or three units to create a larger pond. Adapted from Acién *et al.*, 2017⁷.

The liquid velocity plays a crucial role in power consumption of raceway ponds and maintaining it within certain limits is essential for culture performance. Reducing liquid velocity may impact mixing and cycling time, influencing cell exposure to light. The criterion for setting a fixed liquid velocity is often to prevent cell settling, with 0.2 m s^{-1} commonly reported⁷. However, the settling velocity of microalgae is much lower, and the discrepancy is attributed to flocculation in open raceways. Power consumption varies based on the energy supply system, with paddle wheels being widely used but having low efficiency (10–60%). Efforts are ongoing to improve efficiency and reduce power consumption, with alternatives such as propellers proposed.

1.6.2 Photobioreactors

Photobioreactors (PBRs) are closed systems used for cultivation of microalgae (Fig. 5). These devices provide a protected environment which isolates the microalgae culture and prevents the exchange of gases or contaminants from the atmosphere. Culture parameters such as temperature, oxygen and carbon dioxide concentration, and pH can be controlled in photobioreactors.

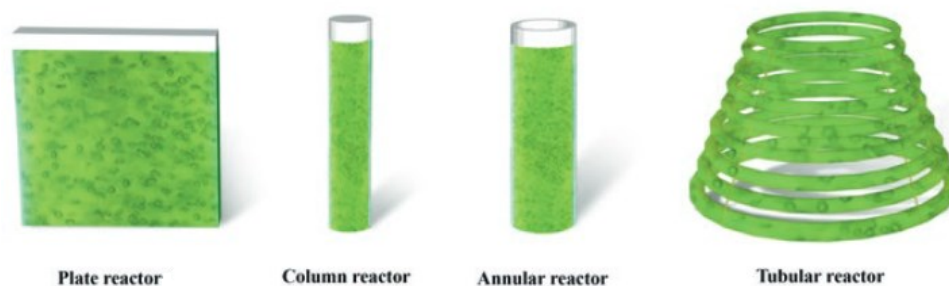


Figure 5: Examples of different types of closed systems for both indoor and outdoor microalgae cultivation. Adapted from Zerrouki and Henni, 2019³⁸.

Tubular photobioreactors are the most common choice for closed systems in large-scale microalgae cultivation^{40,41}. Typically crafted from glass or different types of plastic tubes, these systems often utilize pumps or air streams (airlift) to circulate the culture. Tubular photobioreactors feature S/V ratios that can reach up to $80\ m^{-1}$, allowing for the cultivation at high biomass concentrations. Transparent tubes, with diameters of $0.1\ m$ and lengths ranging from 10 to $400\ m$, are commonly employed in these reactors. The design of tube length and diameter plays a critical role in preventing oxygen accumulation and minimizing photobioreactor head loss⁴². Even in optimal sunlight conditions for efficient light harvesting, there is a risk of significant heat absorption by the culture without proper temperature control⁴³. Cooling strategies for photobioreactors include water spraying on tube surfaces, shading through tube overlapping, immersion of the photostage in a temperature-controlled water bath, and the use of heat exchangers⁴⁴.

Irrespective of the specific reactor design, tubular PBR are commonly divided into two major sections that demand careful attention: (1) the photostage loop and (2) the mixing (retention) tank. The photostage loop, where photosynthesis and biomass growth occur, is the primary section, while the mixing tank is mainly used to eliminate oxygen and regulate culture variables. The determination of the tube diameter in the photostage is the initial variable, influenced by the reactor surface irradiance and the photosynthetic efficiency of the strain, typically ranging from 0.03 to $0.09\ m$. Once the tube diameter is chosen, the total loop length (L) is estimated to prevent inhibiting dissolved oxygen concentrations due to photosynthesis⁷.

To minimize power consumption and prevent cell damage, the liquid velocity is reported to vary between 0.1 to 0.8 $m s^{-1}$, resulting in a total tube length from 10 to 400 m . Mechanical or airlift systems are the common options for liquid circulation, with the power requirements for liquid handling in tubular photobioreactors ranging from 10 to 100 $W m^{-2}$. Regardless of the method chosen for culture circulation, preventing cell damage is crucial, emphasizing the importance of selecting a suitable pumping device (centrifugal, peristaltic, airlift, etc.)³¹.

In general, tubular photobioreactors can be categorized into three main groups: (1) serpentine, (2) spiral, and (3) helical (Fig. 6). Serpentine and manifold photobioreactors may have horizontal, vertical, inclined, or conical arrangements, as indicated by Zittelli and co-authors⁴¹. Nevertheless, the detailed description and comparisons between the different tubular configurations goes beyond the scope of this introduction. Assessing the advantages and limitations of the several tubular PBRs has been the focus of reviews by^{7,40,41,44}, to which the reader is redirected to.

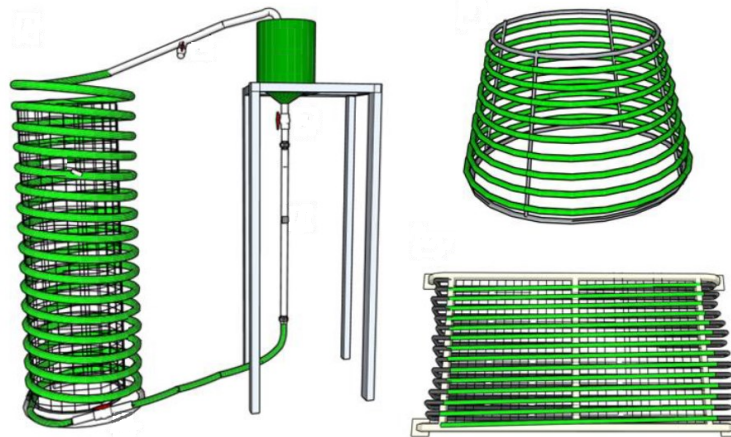


Figure 6: Schematic drawing of serpentine (bottom right), spiral (top right), and helical (left) photobioreactors.

While tubular photobioreactors are crucial for generating high-quality biomass, their implementation cost significantly exceeds that of raceway ponds, reported at 0.51 $M\text{€}/ha$ for a 100 ha scale¹⁰. Indeed, the high investment costs and energy requirements make tubular systems suitable primarily for high-value/niche products and industrial-scale inoculum production, rather than for low-value commodities. Microalgae productivity in tubular photobioreactors depends on various factors, including algae species, location, tube diameter, biomass concentration, distance between tubes, and the number of horizontal tubes per stack.

1.6.3 Flat Panel Photobioreactors

Flat panel photobioreactors represent a conceptually designed system utilizing transparent materials to harness solar radiation effectively. These reactors consist of narrow panels, offering high area-to-volume ratios usually ranging from 16 to 80 m^{-1} , and achieving impressive volumetric biomass productivities. The typical design comprises two parallel panels with a thin layer of microalgal suspension flowing in between ⁴⁵. Transparent panels, commonly made of materials like PVC, polycarbonate, polymethyl methacrylate, glass, or polyethylene, facilitate efficient light transfer with a few centimetres of separation. This configuration's primary advantage lies in its extensive illumination surface compared to the volume of the culture medium required for biomass production. The flat-chamber design, alongside variations such as alveolar reactors, where flat panels are partitioned into internal rectangular channels (alveoli), has been extensively explored. Alveolar reactors offer higher structural rigidity, improved culture flow, enhanced versatility, and commercial availability at lower building costs due to standard thicknesses of the sheets ⁴⁶.

Mixing in flat-plate reactors is usually achieved through gas bubbling or an open gas exchange unit, and with a less extent through pump-assisted circulation. Pump-assisted circulation involves circulating the culture from an open gas exchange unit, often placed horizontally to address oxygen buildup issues. High linear speeds (1.2 $m s^{-1}$) have been reported for pump-driven culture flow, maintaining cell integrity within a safe operating range. In contrast, for pneumatic mixed reactors, even low aeration rates (0.004 $m s^{-1}$) transform the flat-plate into a mixed-tank system ⁴⁷.

Flat-panel reactors operate similarly to bubble columns concerning mass transfer, with the vertical axis being the primary transport axis. The airlift principle can also be applied to these reactors (Fig. 7). Hydrodynamic parameters, crucial for understanding fluid dynamics, have gained attention in recent years. Researchers have characterized flat panel photobioreactors, studying factors such as orientation, gas holdup, mass transfer, mixing time, and heat transfer. Engineering modifications, such as shape alterations and the introduction of horizontal baffles, have been explored to enhance mixing and minimize dead volume. Transparent baffles, in addition to acting as static mixers, increase the surface-to-volume ratio.

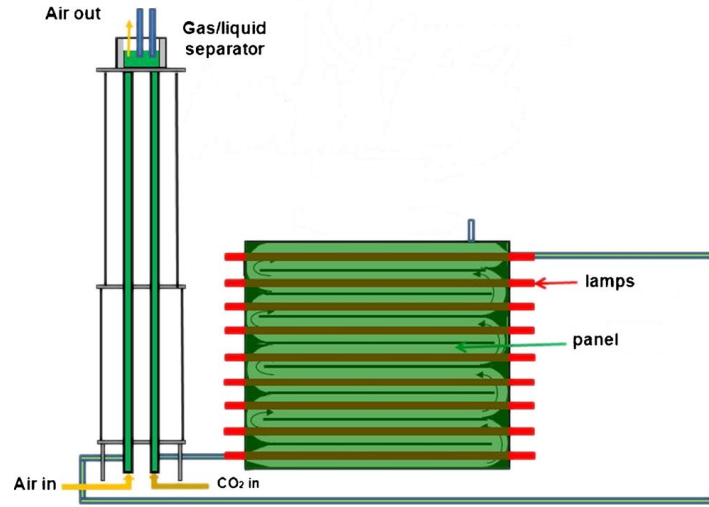


Figure 7: Schematic drawing of an airlift flat panel photobioreactor. Adapted from Li *et al.*, 2015⁴⁸.

Air supply is a pivotal factor governing the energy consumption and mass transfer capacity of flat plate photobioreactors. Power input per volume unit due to aeration (P_G/V_L) can be calculated as function of the liquid density (ρ_L), the gravitational acceleration (g), and the superficial gas velocity in the aerated zone (U_G), with the volumetric gas-liquid mass transfer coefficient governed by the power supply. The relationship between these parameters is expressed through equations (Eq. 1.8 and Eq. 1.9)⁴⁹.

$$\frac{P_G}{V_L} = \rho_L \cdot g \cdot U_g \quad (1.8)$$

$$k_L a = 2.39 \cdot 10^{-4} \left(\frac{P_G}{V_L} \right) \quad (1.9)$$

Flat-plate photobioreactors exhibit versatility in cultivating a diverse range of microalgae, from *Botryococcus braunii* to *Nannochloropsis*, with productivities spanning 5 to 15 $g\ m^{-2}\ day^{-1}$ ⁵⁰. These reactors are acknowledged for achieving high photosynthetic efficiencies. However, they pose challenges, including temperature fluctuations and overheating due to their compact design. Cooling methods involve spraying the surface with water or using double-layered panels with a thermoregulation system. The scale-up of flat-panel photobioreactors presents challenges such as increased costs, fouling, and hydrodynamic stress on sensitive microalgal strains. The main features as well as the advantages and disadvantages of the various cultivation systems are provided in Table 1.

Table 2: Overview of the main microalgae cultivation systems. Adapted from Deprá *et al.*, 2022³⁵.

Cultivation system	Mixing	Gas exchange	Advantages	Limitations
Raceway ponds	Paddle wheel	Poor, mainly achieved through surface aeration	Cost effective; Simple and flexible design; Beneficial for mass cultivation; Already available on the market.	Low biomass productivity; Less control over cultivation conditions; Susceptible to contamination; Large land area required; Low mass transfer Water and CO ₂ loss due to evaporation.
Bubble column PBRs	Airlift/Bubble	Open gas exchange at head space	High mass transfer; Lack of moving parts; Good mixing with low shear stress.	Low surface area for illumination; Biofilm formation on reactor walls; Limited scale up due to design constrains; Shading effect issues; Energy costs.
Tubular PBRs	Recirculation via pumps/Airlift	Injection into feed, dedicated degassing unit	High surface to volume ratio; Good mixing with low hydrodynamic stress; Suitable for outdoor cultivation; High biomass productivity; Reduced photoinhibition.	Dissolved oxygen build-up; Support costs; Fouling due to algal growth; Large space requirement; Poor temperature regulation. Low light penetration along the tubes.
Flat panel PBRs	Airlift/Bubble from bottoms or side	Open gas exchange at head space	High surface to volume ratio; Low space requirements; High photosynthetic efficiency; More uniform distribution of light.	Low mixing efficiencies; Frequent fouling and clean up issues; Poor temperature regulation; Dissolved oxygen build-up; Possibility of shear stress to some algal strains.

Oxygen buildup is a recognized issue in flat panel photobioreactors, especially alveolar ones, attributed to high photosynthetic activity in narrow reactors. The volumetric biomass productivities are higher with minimal light path, but this must be balanced against increased material costs. A thin layer photobioreactor allows better diffusion and light distribution, enhancing optimal cell density and volumetric biomass productivity. However, constructing thin photobioreactors is more expensive, challenging to clean, and susceptible to light inhibition and temperature fluctuations. Despite their apparent simplicity, few flat-panel systems have been utilized for mass algal cultivation due to scale-up limitations and cost concerns. Indeed, currently employed flat panel PBRs are characterized by low mixing efficiency, high energy costs, serious biofouling, and shading effect and light penetration issues, necessitating innovative solutions. Addressing some of these challenges forms the backdrop for the optimization of a novel photobioreactor presented in **Chapter 2** and **Chapter 3** of this PhD thesis.

The design and development of a novel photobioreactor tailored to overcome the limitations of existing systems could unlock unprecedented advancements in sustainable microalgae production. In the existing landscape, the primary method of mixing in flat panel PBRs involves air bubbling directly from the bottom of the panels. This method is associated with elevated energy costs and the risk of biofouling^{18,49}. The reliance on compressed air for mixing constitutes a substantial portion of the PBR's energy consumption, with factors such as compressor type, gas pressure, blower type, and aeration rate influencing power supply⁵¹. While centrifugal pumps offer a more energy-efficient alternative, concerns about cell shear damage have limited their application in tubular PBRs, and literature lacks reports on pilot-scale flat panel PBRs utilizing centrifugal pumps.

In response to these challenges, this PhD research introduces a pioneering flat panel photobioreactor design featuring a centrifugal pump-assisted hydraulic circuit. This innovative system confines microalgae within a positive-pressurized serpentine directly exposed to an artificial light source, with the primary aim of maximizing light distribution through the microalgae culture. The flat panels, measuring 1.3 *cm* in width, are a key feature of this new design. **Chapter 2** of this thesis delves into the design, characterization, and assessment of the proposed photobioreactor, offering valuable insights to enhance its technological efficacy and evaluating its potential applicability in energy-efficient industrial scenarios, with particular emphasis on the CO₂ bio fixation capabilities of the system.

In **Chapter 3**, a comprehensive examination of the proposed photobioreactor's fluid dynamics is described, providing understanding of how the innovative centrifugal pump-assisted hydraulic circuit influences the movement and interaction of microalgae within the positive-pressurized serpentine exposed to artificial light. By elucidating the fluid dynamic intricacies, this chapter aims to contribute valuable insights into optimizing the hydrodynamic performance of the system.

Additionally, **Chapter 3** introduces a pivotal advancement of the lighting system. A tunable LED lighting engine, composed of 10 discrete LEDs characterized by different peaks of dominant wavelength, covering the whole *PAR* range, and 2 white light LEDs, allows for the realization of tailored spectra, wherein the light spectrum emitted is customized to suit the specific requirements of the microalgae being cultivated. These tailored spectra approach not only aims to enhance microalgae growth by aligning the light spectrum with the photosynthetic preferences of the microalgae, but also seeks to minimize the power supply needed for lighting, thereby addressing energy efficiency concerns.

1.7 Modelling light-limited microalgae growth

The exploration of large-scale microalgae and cyanobacteria production holds tremendous potential as a sustainable feedstock for diverse applications like food, feed, chemicals, and potentially, fuels. However, the current landscape of large-scale production is in its infancy, with existing plants covering only a few hectares.

Understanding the intricacies of the microalgal production process is crucial for facilitating successful scale-up. This paragraph reviews a straightforward methodology focused on analysing microalgal production systems, with a particular emphasis on light exposure. This theoretical framework served as the foundation for the work of Blanken and co-authors, who based their modelling approach on these principles ⁵².

Microalgae exploit photosynthesis to convert water and carbon dioxide into sugars by means of light energy. These sugars are subsequently used to support biomass growth. Current light-limited microalgae growth models can be divided in photosynthesis-irradiance (PI) curve-based models ⁵³⁻⁵⁷ and empirical models that are fitted to measured relations between specific growth rate and irradiance ⁵⁸⁻⁶⁰. Although these models often include a respiratory term, Geider and co-authors ⁵⁶ included a growth-related respiratory term. However, sugar is respired for energy to support cellular maintenance and anabolic reactions. Consequently, when neglecting this partitioning, respiration is often identified as energy loss. What is

lacking in the current models used for engineering studies is a simple microalgae growth model which considers compartmentalization between chloroplast and mitochondria.

Microalgae growth in a photobioreactor can thus be calculated based on a model describing light-dependent sugar production by photosynthesis in combination with a model describing aerobic chemoheterotrophic growth on sugar. The model parameters are all independently measurable in dedicated small-scale experiments in addition to the actual process to be predicted. To be suitable as a tool for photobioreactor engineers, the model should be as uncomplicated as possible while still including the most important reactions and providing sufficient accuracy.

In the chloroplast, where the photosynthesis occurs, light energy is absorbed by photosystems located on thylakoid membranes (Fig. 8). These photosystems are equipped with antenna complexes comprising pigment molecules like chlorophylls and carotenoids. The absorbed photons fall within the 400 to 700 nm wavelength range, known as *Photosynthetic Active Radiation (PAR)*.

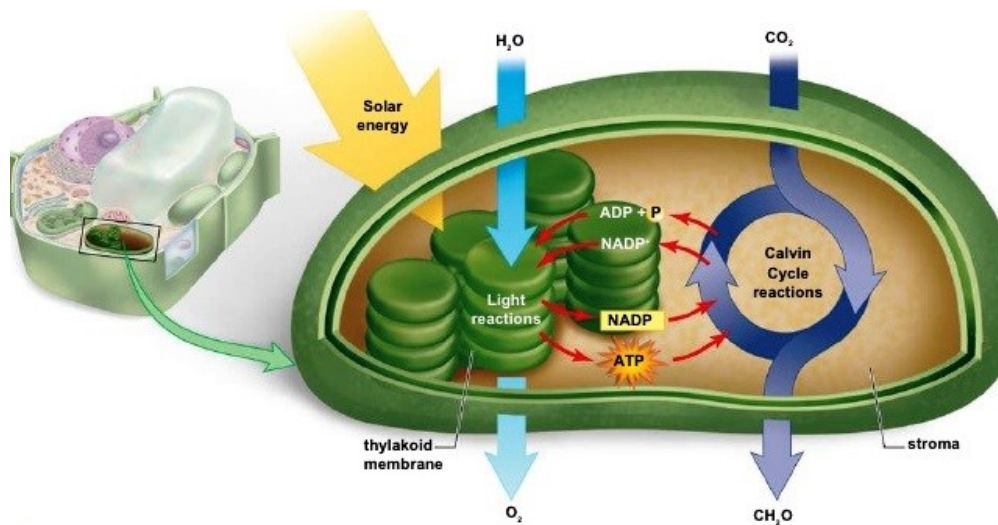
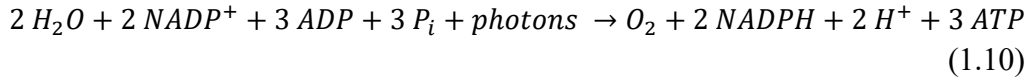


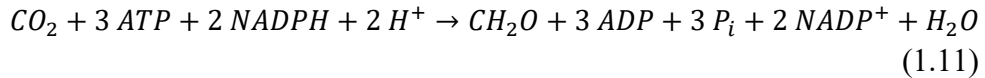
Figure 8: Simplified diagram of the chloroplast and the photosynthetic reactions. (Copyright © McGraw Hill)

The energy derived from absorbed photons is utilized within the photosystems to facilitate the transfer of electrons from water (H₂O) to oxidized nicotinamide adenine dinucleotide phosphate (NADP⁺), resulting in the production of reduced NADPH and oxygen (O₂). Concurrently, adenosine triphosphate (ATP) is generated through a proton motive force over the thylakoid membranes, a process

termed linear photosynthetic electron transport (Eq. 1.10). This intricate process necessitates the coordinated action of two types of photosystems, PSII followed by PSI, to generate sufficient driving force for electron movement from water to NADP^+ .



The NADPH and ATP generated are then utilized within the chloroplast to fix the carbon dioxide (CO_2) and convert it into sugar through the Calvin–Benson–Bassham cycle (Eq. 1.11) (Fig. 8). The resulting sugar, often denoted as CH_2O when normalized to 1 carbon atom, serves as the fundamental building block for microalgal biomass in growth reactions, as it is broken down and oxidized (respired) in the mitochondria to generate ATP. This ATP is needed to drive, or ‘push’, the growth reactions, as well as the maintenance reactions. Maintenance is defined as the collection of cellular processes needed to survive not including growth-related processes.



The stoichiometry of these reactions reveals that the amount of ATP and NADPH needed to fix one mole of CO_2 corresponds to the amount generated in the light reactions when two moles of H_2O are split, leading to the release of one mole of O_2 . The theoretical minimum amount of light (photons) required for this process is 8 photons, based on the functioning of linear photosynthetic electron transport. However, in realistic laboratory conditions, a quantum requirement of 10 is commonly accepted for O_2 production or CO_2 fixation, considering various measurement techniques. This quantum requirement of 10 implies that the maximal yield of sugar (CH_2O) on photons ($Y_{s/ph,m}^c$) is 0.10, a critical parameter for subsequent mathematical modelling of photoautotrophic growth.

The analysis of microalgal growth involves the introduction of specific rates (q), representing biomass-specific production and consumption rates (Fig. 9). The specific rate of sugar production in the chloroplast (q_s^c) is a direct measure of the photosynthetic rate, and it is equivalent to the specific rate of oxygen production ($q_{\text{O}_2}^c$) or carbon dioxide fixation ($-q_{\text{CO}_2}^c$), all serving as measures of photosynthesis (Eq. 1.12). This dynamic process within the chloroplast is denoted by the

superscript 'c', whereas the subscript 's' stands for sugar, and the subscript 'x' for biomass.

$$-q_{CO_2}^c = q_s^c = q_{O_2}^c \quad (1.12)$$

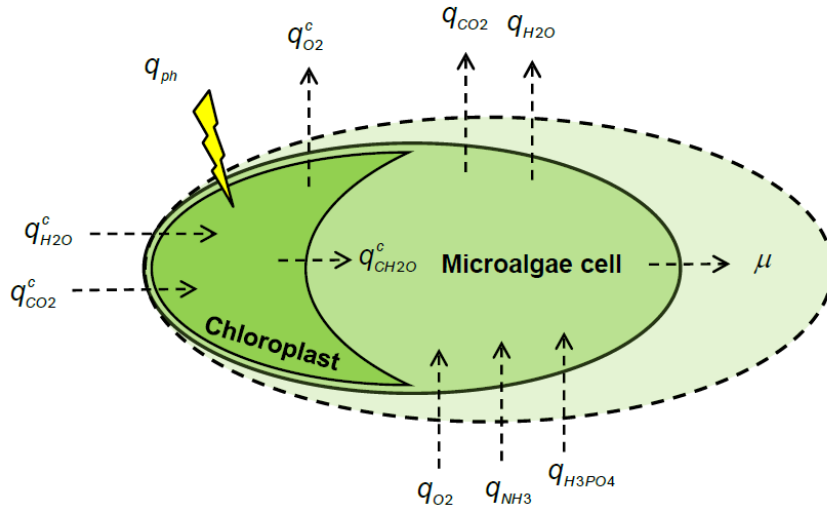


Figure 9: Representation of most important specific consumption and production rates for the quantitative analysis of photoautotrophic growth. The superscript 'c' stands for chloroplast.

The sugar consumption associated with microalgal growth plays a crucial role in accurately quantifying the growth process. Triose sugar within the mitochondria of microalgae undergoes degradation in the citric acid cycle, leading to the oxidation of generated reductant through oxidative phosphorylation. This process produces a substantial amount of ATP, essential for driving various growth reactions. While some analyses assume a constant respiration in microalgal growth, it is well-documented that respiration is intricately linked to growth^{61,62}. Notably, the chloroplast functions as a sugar factory, and the overall process outside the chloroplast can be effectively described as aerobic chemoheterotrophic growth. This connection between sugar metabolism, respiration, and growth highlights the complexity of microalgal growth dynamics.

To delve into the specifics of microalgal growth, Pirt's substrate balance is introduced⁶³. This balance couples the specific sugar consumption rate outside the chloroplast (q_s) to the specific growth rate (μ) of microalgae (Eq. 1.13). The specific sugar consumption rate for maintenance (m_s) is a challenging parameter to measure and is dependent on the microalgal species and growth conditions.

$$q_s = -\frac{\mu}{Y_{x/s}} - m_s \quad (1.13)$$

Where $Y_{x/s}$ is the yield of microalgal biomass on sugar, reflecting the biomass growth on sugar with units $mol_x mol_s^{-1}$. Studies under various conditions have shown a maximal yield of about $0.625 mol_x mol_s^{-1}$ ⁶⁴⁻⁶⁷. Whereas typical values for m_s in laboratory settings range from 1×10^{-6} to $5 \times 10^{-6} mol_s mol_x^{-1} s^{-1}$.

In summary, this chapter has introduced three crucial constants necessary for a quantitative model describing microalgal growth:

1. $Y_{s/ph,m}^c$ - the maximal yield of sugar (CH₂O) on photons in the chloroplast [$mol_s mol_{ph}^{-1}$].
2. $Y_{x/s}$ - the yield of biomass on sugar (CH₂O) [$mol_x mol_s^{-1}$].
3. m_s - the specific sugar consumption rate for maintenance [$mol_s mol_x^{-1} s^{-1}$].

Additionally, two significant variables have been presented, which will play a pivotal role in a comprehensive growth model:

1. q_s^c - the specific sugar (CH₂O) production rate in the chloroplast [$mol_s mol_x^{-1} s^{-1}$].
2. μ - the specific growth rate of microalgae [s^{-1}].

It is important to note that $q_s^c = -q_s$, highlighting the inverse relationship between specific sugar production and consumption rates.

1.7.1 Light absorption, Photosynthesis and Biomass Growth

As already stated, microalgae absorb and use light from the whole *PAR* range. However, microalgal light absorption also varies over the *PAR* wavelength range. This implies that when calculating light absorption we have to take this distribution into account and thus consider two parameters: the total photon flux density (I_{ph}) within the *PAR* range, expressed in $mol_{ph} m^{-2} s^{-1}$, and the wavelength-dependent photon flux density ($I_{ph,\lambda}$), representing the flux at a specific wavelength (λ) within a 1 nm interval, with units $mol_{ph} m^{-2} s^{-1} nm^{-1}$.

The calculation of I_{ph} from $I_{ph,\lambda}$ involves integrating $I_{ph,\lambda}$ over the *PAR* range (Eq. 1.14):

$$I_{ph} = \int_{\lambda=400}^{\lambda=700} I_{ph,\lambda} \cdot d\lambda \quad (1.14)$$

Light absorption, a critical process in photosynthesis, occurs in the pigments of photosystems, situated on the thylakoid membranes within the chloroplast. The specific light absorption coefficient, also termed the optical cross section ($a_{x,\lambda}$), dictates the fraction of incident light absorbed by a microalgal cell. This coefficient, dependent on pigment composition and varying with wavelength, plays a focal role in determining the light absorption capacity.

When light interacts with a microalgal cell, a portion is absorbed by pigments, while the remainder may either pass through the cell, refract due to differences in refractive indices, or be reflected at the cellular surface. This interplay of absorption, refraction, and reflection collectively constitutes scattering. Light absorption by microalgal cells is quantified based on the size of the light-absorbing surface perpendicular to the light beam, encapsulated by the wavelength specific optical cross section coefficient $a_{x,\lambda}$ (Fig. 10).

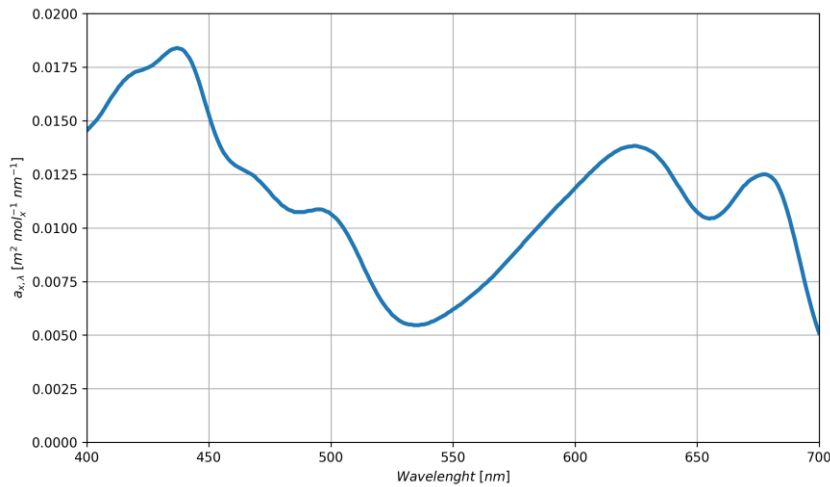


Figure 10: Wavelength specific absorption cross section of a sample of *G. sulphuraria* 074W taken from an autotrophic culture at Politecnico di Torino.

The spectral distribution of light and the photoacclimation process, wherein microalgae adjust their pigmentation in response to light conditions, are integral considerations. In the event of light limitation, microalgae engage in photoacclimation by increasing their specific absorption coefficient $a_{x,\lambda}$. High-light acclimated cells exhibit a smaller absorption coefficient compared to low-light acclimated cells. This underscores the dynamic nature of microalgal light

absorption characteristics. The specific light absorption coefficient $a_{x,\lambda}$ proves pivotal in analysing microalgal production processes, including estimating light penetration in photobioreactors, even while temporarily neglecting light scattering effects. Additionally, this coefficient allows the calculation of the specific photon absorption rate (q_{ph}) of microalgae, considering the spectral distribution of light. The formulation for calculating q_{ph} involves accounting for the wavelength-dependent nature of light, emphasizing the intricate relationship between microalgae and their light environment (Eq. 1.15).

$$-q_{ph} = \sum_{\lambda=400}^{\lambda=700} a_{x,\lambda} \cdot I_{ph,\lambda} \cdot \Delta\lambda \quad (1.15)$$

In the realm of well-designed photobioreactors, light stands out as the primary growth-limiting factor. A profound understanding of how microalgal growth correlates with light becomes pivotal. Initial models aim to elucidate the photosynthetic sugar production rate within the chloroplast, scrutinizing its dependence on photon flux density. The synthesized triose sugar, originating in the chloroplast, plays a key role in cellular processes. By understanding the specific sugar consumption rate, one can derive the microalgae's specific growth rate, thus establishing a vital connection between sugar production and overall biomass growth.

The specific sugar production rate in the chloroplast (q_s^c) is contingent upon the photon flux density (I_{ph}), and the model proposed by Jassby & Platt⁶⁸, employing the hyperbolic tangent function, provides a comprehensive depiction of this relationship (Eq. 1.16).

$$q_s^c = q_{s,m}^c \cdot \tanh\left(\frac{\alpha \cdot I_{ph}}{q_{s,m}^c}\right) \quad (1.16)$$

This model portrays the specific rate of photosynthesis, illustrating an initial rapid increase with rising photon flux density, followed by a slowing down, eventually reaching the maximum rate denoted as $q_{s,m}^c$ (Fig. 11).

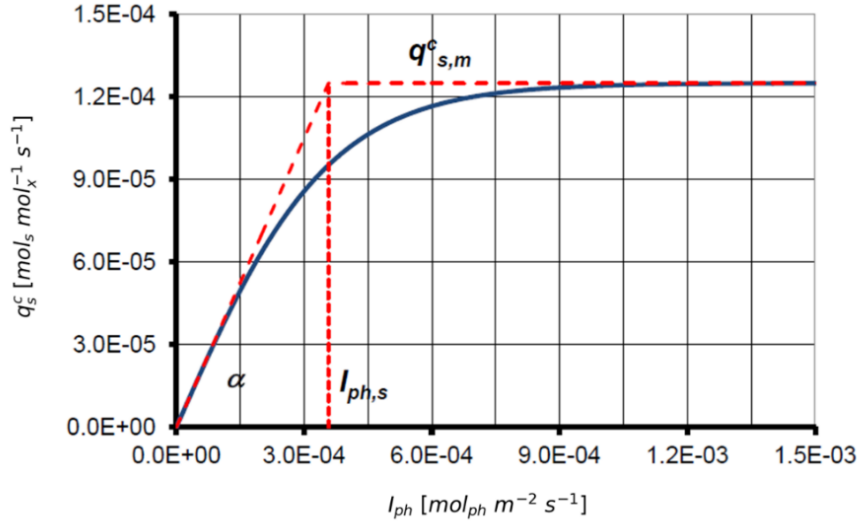


Figure 11: Example of the specific rate of photosynthesis a function of photon flux density I_{ph} according to the model of Jassby & Platt. The specific sugar production rate in the chloroplast q_s^c represents photosynthesis.

Parameters such as α hold significance, representing the initial slope of the curve. α , defined as the product of the maximal yield of sugar on photons ($Y_{s/ph,m}^c$) and the spectrally averaged absorption coefficient a_x , contributes to the biological interpretation of the system (Eq. 1.17):

$$\alpha = Y_{s/ph,m}^c \cdot a_x \quad (1.17)$$

As in Eq. 1.15, the specific photon absorption rate (q_{ph}) is calculated from a_x and I_{ph} (or $a_{x,\lambda}$ and $I_{ph,\lambda}$), and by combining Eq. 15,16 and 17, It follows that (Eq. 1.18):

$$q_s^c = q_{s,m}^c \cdot \tanh\left(\frac{Y_{s/ph,m}^c \cdot a_x \cdot I_{ph}}{q_{s,m}^c}\right) = q_{s,m}^c \cdot \tanh\left(\frac{-q_{ph} \cdot Y_{s/ph,m}^c}{q_{s,m}^c}\right) \quad (1.18)$$

Although simpler alternative models exist (e.g., Blackman, Monod, Webb), the model of Jassby & Platt is reported to best describe the photosynthetic response to light ^{68,69}.

Given that the specific sugar consumption rate outside the chloroplast is equal to the photosynthetic sugar production rate ($-q_s = q_s^c$), Pirt's formula (Eq. 1.13) can be rewritten to couple the microalgal growth to the photosynthetic sugar production (Eq. 1.19).

$$\mu = (q_s^c - m_s) \cdot Y_{x/s} \quad (1.19)$$

The variable q_s^c depends on the photon flux density I_{ph} as in Eq. 1.18, thus it follows that:

$$\mu = f(I_{ph}) = (q_s^c(I_{ph}) - m_s) \cdot Y_{x/s} \quad (1.20)$$

Not surprisingly, the relation between specific growth rate and photon flux density (Eq. 1.20) has an almost identical shape as the relation between the specific rate of photosynthesis and photon flux density. But, because of the maintenance requirement for sugar m_s there will be ‘negative growth’ in darkness meaning that sugar reserves are slowly depleted. In order to achieve positive growth the photon flux density I_{ph} needs to be higher than the so-called compensation point of photoautotrophic growth $I_{ph,c}$ (Fig. 12). At this photon flux density $I_{ph,c}$, just enough sugar is produced in the chloroplast to compensate for the amount lost due to cellular maintenance.

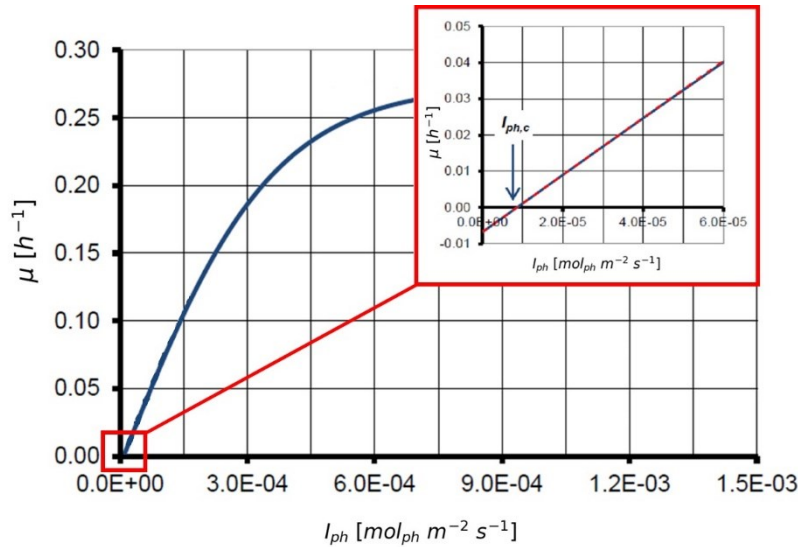


Figure 12: Example of the specific growth rate μ of a microalga as a function of photon flux density I_{ph} . The specific growth rate is derived from Pirt's law in combination with the photosynthesis models of Jassby & Platt. The insert illustrates the compensation point $I_{ph,c}$ where photosynthesis q_s^c is compensated by maintenance associated respiration m_s .

1.7.2 Estimating Photobioreactor productivity

Estimating photobioreactor productivity involves a nuanced understanding of light absorption dynamics within a microalgal culture. The local photon flux density relies on the wavelength-dependent specific light absorption coefficient ($a_{x,\lambda}$), determining light penetration. The Law of Lambert-Beer facilitates the calculation of photon flux density ($I_{ph,\lambda}(z)$) at various locations z within the culture, assuming a uni-directional light field (e.g., raceway ponds or flat-panels) (Eq. 1.21).

$$\frac{dI_{ph,\lambda}}{dz} = -a_{x,\lambda} \cdot C_x \cdot I_{ph,\lambda} \quad (1.21)$$

Integrating from the light exposed surface ($z = 0$) to any location z then delivers an exponential decrease of the photon flux density over z (Eq. 1.22).

$$I_{ph,\lambda}(z) = I_{ph,\lambda}(0) \cdot e^{-a_{x,\lambda} \cdot C_x \cdot z} \quad (1.22)$$

This approach can be also simplified by adopting the spectrally averaged specific absorption coefficient a_x (Eq. 1.23, 1.24) (Fig. 13).

$$a_x = \sum_{\lambda=400}^{\lambda=700} a_{x,\lambda} \cdot E_{n,\lambda} \cdot \Delta\lambda \quad (1.23)$$

$$I_{ph}(z) = I_{ph}(0) \cdot e^{-a_x \cdot C_x \cdot z} \quad (1.24)$$

Where $E_{n,\lambda}$ is the PAR-normalized spectrum of light source used: $E_{n,\lambda} = \frac{I_{ph,\lambda}}{I_{ph}}$

In theory an error is introduced when assuming a constant specific absorption coefficient a_x . This is related to the fact that the spectral distribution of light $E_{n,\lambda}$ changes when moving deeper inside a microalgal culture.

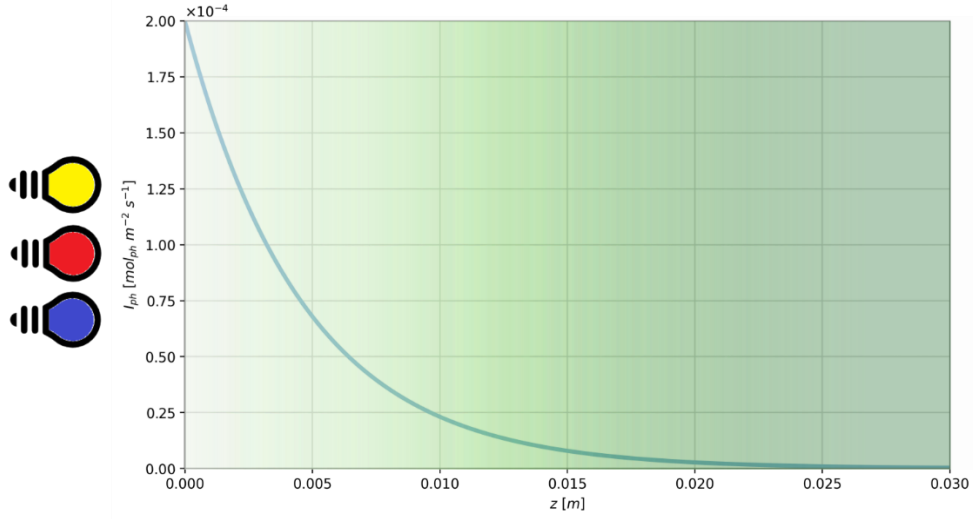


Figure 13: Example of a light (I_{ph}) penetration pattern in a microalgal culture as function of depth z . The calculation of I_{ph} is based on Lambert-Beer with a constant specific light absorption coefficient a_x , neglecting wavelength dependency of light absorption.

According to the Jassby & Platt model, to assess volumetric productivity accurately, the average specific sugar production rate within the microalgal culture must be computed as Eq. 1.25.

$$\overline{q_s^c} = \frac{\int_0^d q_s^c(z) \cdot dz}{d} \quad (1.25)$$

With Eq. 1.18 rewritten as function of z (Eq. 1.26):

$$q_s^c(z) = q_{s,m}^c \cdot \tanh\left(\frac{Y_{s/ph,m}^c \cdot a_x \cdot I_{ph}(z)}{q_{s,m}^c}\right) \quad (1.26)$$

In this approach it is assumed that q_{ph} , and q_s^c , are constant over the finite layer Δz . This assumption is only valid when the number of layers N is sufficiently large and Δz sufficiently small. Having calculated the average specific rate of photosynthesis, the average specific growth rate can be calculated (as in equation 1.20), and from that volumetric productivity starting from the following biomass balance over the photobioreactor (Eq. 1.27):

$$V_r \cdot \frac{dC_x}{dt} = F_{in} \cdot C_{x,in} - F_{out} \cdot C_{x,out} + r_x \cdot V_r \quad (1.27)$$

where V_r is the volume of the PBR, F_{in} the inlet flow rate, $C_{x,in}$ the biomass concentration in the inlet stream, F_{out} the outlet flow rate, $C_{x,out}$ the biomass concentration in the outlet stream, and r_x the biomass productivity.

In a batch wise cultivation, there is no dilution with water and nutrients, and the biomass balance can be simplified to the following relation (Eq. 1.28):

$$\frac{dC_x}{dt} = \mu \cdot C_x \quad (1.28)$$

Microalgae can also be grown continuously meaning that the microalgal culture is continuously harvested and the liquid volume removed is continuously replaced with fresh water with nutrients. In the case of chemostat operation the dilution rate (D) is fixed. Assuming a constant photon flux density a steady state will be reached where the biomass concentration does not change anymore and is constant. The influent, water with nutrients, usually does not contain any microalgae. Furthermore, the liquid volume is usually maintained constant, so: $F_{in} = F_{out} = F$. Finally, it will be assumed that the liquid inside the photobioreactor is perfectly mixed, so: $C_{x,out} = C_x$. Then the biomass balance over the photobioreactor from Eq. 1.27 can be simplified as follows (Eq. 1.29):

$$F \cdot C_x = \mu \cdot C_x \cdot V_r \quad (1.29)$$

And thus:

$$\mu = \frac{F}{V_r} = D \quad (1.30)$$

When operating a photobioreactor as a chemostat the dilution rate is fixed, and the microalgae are forced to grow with a specific growth rate equalling the dilution rate (Eq. 1.30). The optimal dilution rate can be selected based on the relations derived before coupling the average specific growth and the biomass concentration in a photobioreactor. Please note that the product of biomass concentration and specific growth rate gives the volumetric productivity of the photobioreactor.

In whatever the process is carried out, a balance needs to be found between achieving a high volumetric productivity of the photobioreactor and a high biomass concentration in the outflow. This underscores the paramount role of models in determining the most economical and sustainable operational processes for photobioreactors.

The first-principle equations described in this paragraph have been used for the hybrid model approach developed in **Chapter 4** of this PhD thesis, providing a straightforward and engineering-friendly method that not only streamlines computational processes, but also eliminates the need for experimental exploration of some of the parameters in the absence of relevant literature data.

The hybrid model has been trained and validated using batch cultivations of the red microalga *Galdieria sulphuraria* grown within the specific flat panel reactor described in this thesis. These experiments adhere to the culture and spectra conditions expounded in **Chapter 3**. The accurate control over all the process conditions provided by the flat panel reactor, including the light supply management and tailored light spectra, allowed for the robust performance of the hybrid model applied to this microalga, yielding insights into optimal process conditions and striking a balance between biomass concentration and volumetric productivity.

Nevertheless, while the hybrid model exhibits robust performance for the specific conditions of the *Galdieria sulphuraria* cultivations and the assumptions detailed in **Chapter 4**, its validation for other microalgae species, as well as a more accurate integration of the mixing and light exposure, remain necessary steps to ensure the reliability and applicability of the model across a broader range of microalgae in the pursuit of comprehensive and reliable results in the field.

Chapter 2

Design and characterization of a new pressurized flat panel photobioreactor for microalgae cultivation and CO₂ bio-fixation.

2.1 Introduction

Since the 20th century, the concentration of greenhouse gases in the atmosphere continued to increase as result of anthropogenic activities related to the use of fossil fuels, deforestation, and agricultural activities. The annual global average carbon dioxide concentration at Earth's surface in 2020 has reached 412.5 ± 0.1 ppm, the highest value in modern atmospheric records, increasing by 2.5 ± 0.1 ppm from 2019, a value comparable to the average rate of increase during the last decade⁷⁰. Therefore, the development of renewable and clean technologies is needed to sustain a considerable fraction of the global economy and to reduce the impact of human activities. In parallel, major efforts are needed to improve CO₂ Capture and Utilization (CCU) technologies that can effectively reduce carbon dioxide emissions mainly from power plants and different industrial processes.

In this context, microalgae-based refinery concepts have gained importance over the last few decades. Microalgae are considered promising biochemical factories and excellent CO₂ fixers⁷¹. Their simple cellular structure, large surface-to-volume ratio, and aquatic lifestyle allow these organisms an easy access to water, CO₂ and other nutrients, and thus a more efficient conversion of solar energy into chemical energy, showing 10-50 higher CO₂ fixation rates than land plants⁷²⁻⁷⁴. Moreover, compared to higher plants, microalgae also show faster growth rates, and their cultivation does not compete for arable lands^{75,76}. As a result of CO₂ fixation, microalgae accumulate significant amounts of carbohydrates, proteins, lipids, and other valuable compounds, such as pigments and vitamins. Hence, microalgal

biomass is considered a promising energy feedstock with multifaceted applications in the production of dietary supplements, cosmetics, food and animal feed and biofuels^{77–80}. Algal cultivation technologies are traditionally classified as open or closed systems (PBRs). Open cultivation systems (*e.g.*, artificial ponds, raceways, thin layer) produce algal biomass at lower costs thanks to their lower investment and management costs in terms of Capital Expenditure (CapEx) and Operating Expense (OpEx)³⁶. The open raceway pond is currently the most frequently used and cheapest cultivation system for commercial production of microalgae⁷. Despite this, the open pond technology is limited by several disadvantages such as low biomass productivities, mainly related to poor mixing, low CO₂ mass transfer, high risk of biological and chemical contamination and high consumption of water. Moreover, its dependence on climatic conditions limits its application to tropical and subtropical regions^{44,81,82}. On the other hand, closed photobioreactors allow precise control of the operating conditions and show higher biomass productivities. The confined space limits contaminations and assures higher biomass quality but requires higher CapEx and OpEx^{10,83}. Currently, tubular photobioreactors are the most common closed system configurations for industrial-scale microalgae cultivation, mainly related to high-value applications^{7,40,81}. However, all types of closed systems present major constraints in the process scale-up, mainly due to the difficulty in increasing the sizes of PBRs while keeping optimal culture and hydrodynamic parameters. The choice of the circulating device and design of the PBR influences important operating parameters such as mixing time, turbulence degree, O₂ build-up, and CO₂ supply, thus impacting on both the overall performance of the process⁸⁴ and the final cost. An extensive comparison of the strengths and limitations of the different cultivation systems, together with the importance of illumination and hydrodynamic parameters, has been thoroughly analysed in several reviews^{7,40,44,45,85,86}. It is important to note that, although many PBRs and open system setups have been proposed at laboratory and industrial levels, there is no optimal design for all applications. Moreover, the overall negative energy balance of the processes still poses limitations in the scale-up of microalgal culture technologies, making them profitable only for applications with high added value goods such as dietary supplement and cosmetic raw materials^{9,18,87}. Recently, several studies have focused on the development of many simulation approaches coupling computational fluid dynamics, mass transport phenomena and microbial growth kinetics, to identify the best conditions to maximize microalgae productivity^{88–92}. Likewise, several new design of open, closed, and hybrid PBRs setups based on different hydrodynamics, mass transfer mechanisms and illumination strategies have been proposed to improve the global cultivation efficiency and the scale-up

feasibility^{15,18,49,92–101}. Particularly, more attention was given to flat panel PBRs due to the high photosynthetic efficiencies that can be reached¹⁰². However, currently employed flat panel PBRs still present some limitations mainly due to the low mixing efficiency, being the air bubbled mainly directly from the bottom of the panels, which brings to high energy costs and can lead to the occurrence of serious biofouling^{18,49}. Moreover, the use of compressed air for mixing constitutes a major part of the PBR energy consumption. Indeed, the power supply associated to air compression is function of the type of compressor, gas pressure, type of blower, and the aeration rate⁵¹. Centrifugal pumps, which are considerably more efficient than air compressors, have been mainly employed in tubular PBRs, although the concern for cell shear damage has led more frequently to the use of air-lift pumps. Nevertheless, as pointed out by Norsker and co-authors, the use of centrifugal pumps would be not recommended only for the cultivation of very shear sensitive algae¹⁰. To our knowledge, no literature reports are present concerning pilot-scale flat panel PBRs with a centrifugal pump. In this research, it is presented the design and characterization of a novel alveolar flat panel photobioreactor with a pump-assisted hydraulic circuit, that constrains microalgae to flow inside a positive-pressurized serpentine directly exposed to the artificial light source. The system has been realized to maximize the distribution of light through the microalgae culture as the width of the flat panels is equal to 1.3 cm. The main purpose of this work was to assess the hydrodynamic and cultivation performances of the proposed PBR. The results will help to improve the actual proposed technology and to evaluate its possible use in an industrial scenario, in which the application of energy-efficient technologies is nowadays a priority.

Therefore, the hydraulic, lighting and energetic behaviour of the new flat-panel PBR were investigated through the experimental characterization of the hydraulic flow, mixing time, CO₂ gas-liquid mass transfer coefficient, and irradiance matrix. The biological performances of this new prototype were tested by cultivating the green microalga *Acutodesmus obliquus*.

2.2 Materials and Methods

2.2.1 The flat panel photobioreactor

The photobioreactor used in this research was kindly provided by Arcobaleno Cooperativa Sociale (Turin, Italy), the patent holder of the PBR (EP2830413A1). A representative scheme of the PBR is reported in Figure 14A. Briefly, it is composed by two interconnected units: a photostage loop and a mixing tank. The photostage loop consists of two parallel alveolar flat panels illuminated by an interposed array of seven fluorescent lamps (58W, OSRAM, Germany). The alveolar flat panels are made of transparent polycarbonate with a light exposed surface area of 1.5 m^2 each and an internal path of 13 mm . Each panel is partitioned into 28 internal channels (alveoli) for a total length of the illuminated path of about 40 m and total volume of about 17 L . The mixing tank is made up with a darkened HDPE (High density polyethylene) material with a total volume of 50 L . Its truncated-cone shape has been designed to minimize biomass sedimentation (Fig. 14B). The tank is equipped on its top of a hydraulic inlet and a removable lock cap. A hydraulic circulator (ALPHA1 L - 45W, Grundfos, Denmark) is connected at the bottom of the mixing tank and upstream of the photostage loop. The hydraulic circulator drives the liquid flow into both flat panels, from the bottom to the top. Moreover, the hydraulic circulator allows to manually set up three different factory-defined liquid flow rates operating with constant performance curves.

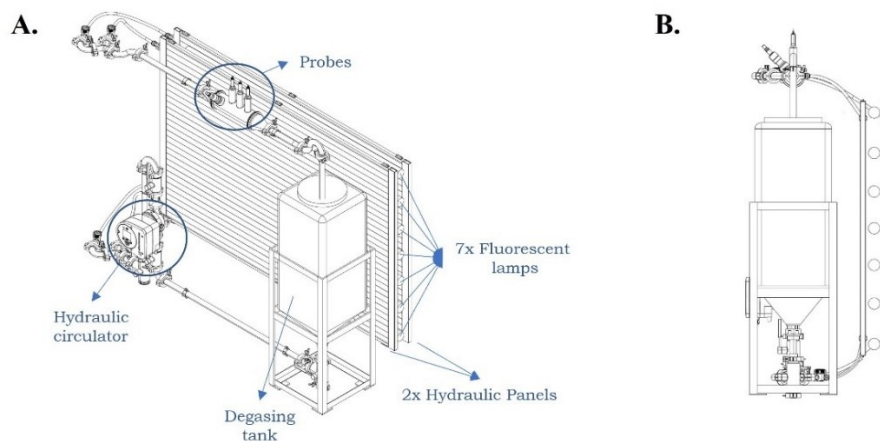


Figure 14: Schematic representation of the flat panel photobioreactor. A) 3D isometric view of the whole PBR. B) Schematic view of the mixing tank.

Gas inlet coming from a food grade CO₂ tank is located between the bottom of mixing tank and the hydraulic circulator. This configuration maximizes gas dissolution in the liquid phase thanks to the turbulence generated by the circulation system. CO₂ flow rates are finely regulated by a thermal flow meter (Red-y smart controller GSC, Vögtlin Instruments GmbH Switzerland), whereas temperature/pH, conductivity, dissolved oxygen, and carbon dioxide are constantly monitored by a InPro 325Xi pH electrodes, Four-electrode conductivity sensor, InPro 6000 Optical O₂ sensor and a InPro 5000i CO₂ sensor (Mettler-Toledo®, USA), respectively. The probes are located at the output of the flat panels. The PBR is equipped with a Mettler-Toledo® multi-parameter transducer M800 and the signals from the sensors are transmitted to a Programmable Logical Controller (PLC, Unitronics, Israel) through industrial standard analogic signal protocol (4-20 mA). The PLC controls a dedicated solenoid valve for the CO₂ injection, allowing the regulation of the CO₂ flow based on pH or carbon dioxide concentration threshold, according to the experimental setup. A schematic overview of the whole PBR working process is reported in Figure 15.

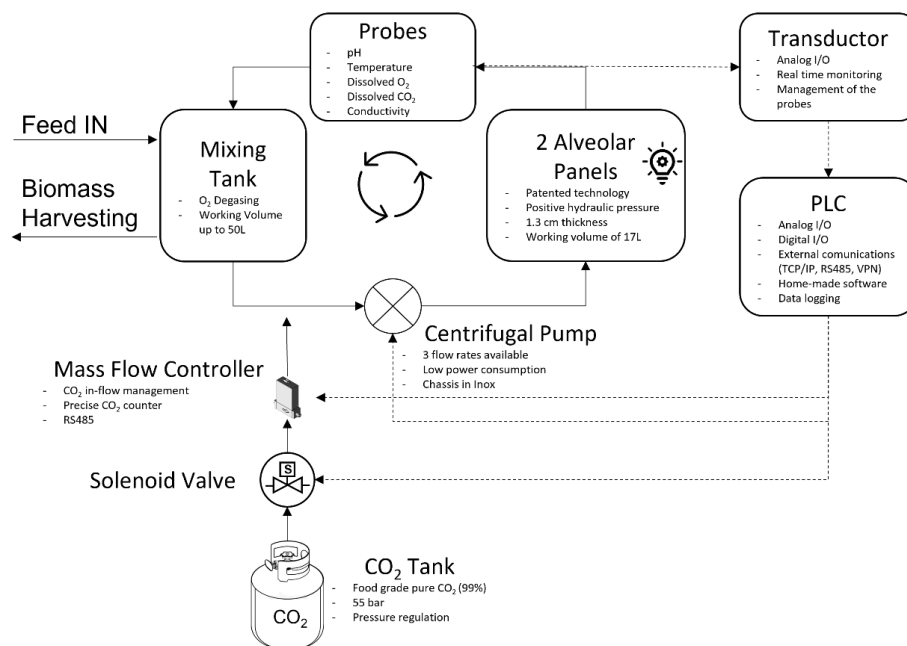


Figure 15: Schematic process diagram of the flat panel photobioreactor.

2.2.2 Microalgae and cultivation conditions

Acutodesmus obliquus strain 276-3b, formally *Scenedesmus obliquus* (Turpin) Kützing, was obtained from the SAG Culture Collection of Algae (Göttingen, Germany). The inoculum preparation was carried out in batch mode and axenic conditions in 2 L disposable culture chambers by using a 1.5 L volume of sterile BG-11 medium¹⁰³. The cultures were maintained at constant temperature ($23^{\circ}\text{C} \pm 2$), pH 7.00-7.50, and under constant (24/24 h of illumination) artificial illumination ($120 \mu\text{mol}_{ph} \text{m}^{-2} \text{s}^{-1}$) by fluorescence tubes (Osram, Germany). Aeration and mixing of the cells were guaranteed by flowing air at the bottom of the chambers. The microalgal cells were used to inoculate the flat panel photobioreactor when they just reached the stationary phase. The PBR was inoculated with BG-11 medium and microalgae cells for a total volume of 60 L, corresponding to a surface area-to-volume ratio (S_f/V) of 50m^{-1} , and an initial cell concentration of 0.25g L^{-1} of dry weight. Each experiment in the PBR was conducted in batch mode for 7 days. The injection of CO_2 was carried out with a flow rate of 0.12NL min^{-1} , keeping constant the CO_2 concentration threshold in the PBR at 25mg L^{-1} using the combination of solenoid valve and mass flow meter.

2.2.3 Biomass concentration measurements

Microalgae growth was gravimetrically quantified as dry biomass concentration as previously reported¹⁰⁴. Briefly, 10-20 mL of microalgae culture was filtered using pre-weighted $1.5 \mu\text{m}$ pore size glass fibre filters (Hahnemühle, Germany). The filters were then dried using a thermobalance (MLS-N, Kern, Germany) until stable weight, and then weighted with an analytical balance (Kern, Germany).

The biomass volumetric productivity (P_x) was then calculated as Eq. 2.1:

$$P_x = \frac{X_t - X_0}{t - t_0} \quad (2.1)$$

where X_t is the biomass concentration [g L^{-1}] at time t [d], and X_0 is the biomass concentration [g L^{-1}] at time t_0 [d].

2.2.4 Hydraulic flow determination

The hydraulic flow rate of the hydraulic circulator was measured using an electromagnetic flow meter (FD-Q20C, Keyence, Japan). All measurements were carried out by placing the flow meter at the outlet of the hydraulic panels.

2.2.5 CO₂ mass transfer coefficient ($k_L a_{CO_2}$)

To estimate gas-liquid transfer efficiencies of the photobioreactor, the $k_L a_{CO_2}$ was measured using 60 L of distilled water (without microalgal cells) to avoid interferences of biological activity. The test was conducted at room temperature and atmospheric pressure ($25 \pm 2^\circ C$ and $101.325 Pa$).

The tests were conducted by blowing a constant and continuous flow rate of CO₂ inside the PBR and monitoring, through the CO₂ probe, the carbon dioxide concentration over time. Different carbon dioxide flow rates were tested at different hydraulic circulator powers (different hydraulic flow rate). As indicated in paragraph 2.2.1, the PBR employs a circulation system that allows to choose between three different levels of power flows corresponding to three different liquid rates. For each circulation level, the $k_L a$ value was identified for different carbon dioxide flow rates.

The $k_L a_{CO_2}$ parameter was determined using a slightly different equation compared to Eq. 1.7 reported in [section 1.5](#), not including the photosynthetic CO₂ consumption rate since the measurements were performed without microalgae (Eq. 2.2)⁴⁹:

$$\frac{dC}{dt} = k_L a_{CO_2} * (C^* - C) \quad (2.2)$$

where integration for $C = C_0$ at $t = 0$ lead to Eq. 2.3:

$$\ln\left(\frac{C^* - C}{C^* - C_0}\right) = -k_L a_{CO_2} * t \quad (2.3)$$

where C_0 is the initial CO₂ concentration [$mg L^{-1}$], C is the dissolved CO₂ concentration [$mg L^{-1}$] at time t , C^* is the CO₂ saturation concentration in water [$mg L^{-1}$] and t is time [min]. Since dissolved carbon dioxide is in equilibrium with carbonate and bicarbonate species, to determine the exact concentration of carbon

dissolved into the aqueous phase the relevant equilibrium and corresponding equilibrium constants were calculated as previously reported ⁹⁵.

2.2.6 CO₂ fixation yield

The CO₂ fixation yield (η_{CO_2}) expresses the CO₂ bio-fixation rate of the culture in terms of percentage ¹⁰⁵. It is calculated as the ratio between the kilograms of carbon accumulated within the algal biomass at the end of the cultivation and the kg of carbon supplied to the microalgae through the injection of CO₂ at a known flow rate (Eq. 2.4), as previously reported ¹⁰⁵.

$$\eta_{CO_2} = \frac{W_{C \text{ biomass}}}{W_{C \text{ in}}} * 100 \quad (2.4)$$

with $W_{C \text{ biomass}}$ and $W_{C \text{ in}}$ deriving respectively from Eq. 2.5 and Eq. 2.6:

$$W_{C \text{ biomass}} = W_{\text{biomass}} * C_{C \text{ biomass}} \quad (2.5)$$

$$W_{C \text{ in}} = (W_{CO_2 \text{ in}} - W_{CO_2 \text{ water}}) * (M_C / M_{CO_2}) \quad (2.6)$$

where $W_{C \text{ biomass}}$ is the kg of carbon accumulated in the biomass; W_{biomass} the kg of biomass obtained during the cultivation; $C_{C \text{ biomass}}$ is the fraction of carbon within the cells obtained through experimental elemental analysis of *A. obliquus*; $W_{C \text{ in}}$ is the kg of carbon injected into the PBR as CO₂ flow; $W_{CO_2 \text{ in}}$ is the total kg of CO₂ injected; $W_{CO_2 \text{ water}}$ is the kg of CO₂ dissolved in water at the end of the batch; M_C and M_{CO_2} represent respectively the molar mass of carbon (12 g mol⁻¹) and carbon dioxide (44 g mol⁻¹).

2.2.7 Mixing time

The mixing time (t_m) is defined as the time required to attain a given uniformity close to the fully mixed state after the injection of a tracer ¹⁰⁶ and it was evaluated by a pH tracing test. To estimate the mixing time of the photobioreactor, the experiments were performed using 60 L of distilled water (without microalgal cells) to avoid interferences of biological activity. Diluted hydrochloric acid (5 mL HCl; with a final concentration in the PBR of 10⁻³ M) was poured into the mixing tank of the photobioreactor, and the pH was recorded every minute by the pH probe located at the output of the flat panels. The t_m was determined as the time required to reach the 95% of complete homogeneity after the injection of the HCl solution ¹⁰⁷.

2.2.8 Energetic measurements

The energy consumption of the PBR main components (hydraulic circulator and lighting system) was measured using a digital multimeter (Siglent SDM3065X-SC, Germany). Voltage and current intensity measured for each unit were used to calculate the power input expressed in Watt [W]. These data, together with the hydraulic flow measurements, were further computed to evaluate the net energy consumption for the fluid handling as $W m^{-3}$.

2.2.9 Radiance matrix

The PBR was illuminated by an artificial lighting system based on an array of seven fluorescent tubes interposed between the two flat panels. To evaluate the uniformity of incident light on both exposed surfaces of the panels, the light intensity was determined by a PAR spectroradiometer (PLA 20, Everfine, China). A matrix array was imposed on the artificial lighting system to fix and homogeneously distribute the sampling points along the radiant surface. The data obtained from the measurements were interpolated using the software Matlab[®] to create the pattern of light intensity for the whole exposed panel surface.

The light uniformity coefficient was calculated using Eq. 2.7:

$$U_I = \frac{I_{min}}{I_{mean}} \times 100 \quad (2.7)$$

where U_I is the light uniformity coefficient [%], I_{min} is the minimum value of light intensity [$\mu mol_{ph} m^{-2} s^{-1}$] and I_{mean} is the mean value of light intensity [$\mu mol_{ph} m^{-2} s^{-1}$].

2.3 Results and discussion

2.3.1 Hydrodynamics flow description

This study has described, for the first time in the literature, the hydrodynamics, mass transfer and mixing time parameters of an innovative and patented flat panel photobioreactor. The experimental characterization of biological performance parameters has been also reported. Key hydrodynamic parameters have been explored in order to compare the pump-assisted setup of the cultivation system here reported to traditional flat panel photobioreactors. In the latter, mixing and liquid

flow is typically achieved by air bubbling or through an external airlift system. Whereas the hydrodynamics of the described PBR is function of the pump-driven culture flow, and thus is linked to the gross power of the hydraulic circulator. Therefore, the hydrodynamics characterization of the reactor included the measurements, at the three default pump setups and at various CO₂ injection rates, of the different liquid flow rates and the effects on the mixing time and the CO₂ volumetric mass transfer coefficient ($k_L a_{CO_2}$).

The hydraulic flow rates calculated using the available standard setups on the circulator system (hereafter named level I, II, III), and their variations at increasing flow of injected CO₂ gas were measured. As shown in Table 2, the experimental results showed that, without any gas injection, the hydraulic flow varies greatly from 4 L min⁻¹ for the lower configuration of the circulator to values of 14 and 18 L min⁻¹ for level II and level III, respectively. The calculated liquid flow velocity (U_L) within the alveoli is 0.17, 0.60 and 0.77 m s⁻¹ at level I, II and III, respectively.

Table 2: Variation of hydraulic flow rates according to the manually chosen level of the hydraulic circulator and the CO₂ flow injection. Liquid flow rates for the higher levels of the circulation system, at low CO₂ flow rates, were not measured assuming a negligible reduction of the rates according to the data for level I. Liquid flow rates (L min⁻¹) are shown as the average of three replicates ± standard deviation. U_L = liquid flow velocity (m s⁻¹).

Liquid flow rate [L min⁻¹]			
CO₂ flow rate [NL min⁻¹]	Circulator level I $U_L = 0.17 \text{ m s}^{-1}$	Circulator level II $U_L = 0.60 \text{ m s}^{-1}$	Circulator level III $U_L = 0.77 \text{ m s}^{-1}$
None	4.05 ± 0.03 (100%)	14.11 ± 0.15 (100%)	18.10 ± 0.33 (100%)
0.06	3.66 ± 0.11 (90.4%)	n.d.	n.d.
0.12	3.69 ± 0.09 (91.1%)	n.d.	n.d.
0.48	3.58 ± 0.02 (88.4%)	13.52 ± 0.31 (95.8%)	n.d.
0.60	3.62 ± 0.05 (89.4%)	11.23 ± 0.61 (79.6%)	n.d.
0.84	n.d.	8.61 ± 0.09 (61%)	18 ± 0.05 (99.4%)
1.08	n.d.	n.d.	16.95 ± 0.56 (93.6%)

Since the CO₂ is injected immediately upstream of the circulator, the hydraulic flow is affected by the gas flow, and it is reduced as the gas flow rate increases. This is mostly evident at level II of the circulator. Gas flow rates above 0.48 NL min⁻¹ reduce the hydraulic flow rate to values below 90% of the hydraulic load without CO₂ injection. On the contrary, the liquid flow rate at level III (18 L min⁻¹) is not significantly reduced by even higher CO₂ rates. Whereas no significant reductions in the liquid flow occur at the lower configuration of the circulator (level I). In the latter case, the low liquid flow (4 L min⁻¹) could favor a gas leak toward the tank rather than being swallowed up by the circulator and dissolved within the bulk flow to the hydraulic panels.

2.3.2 Mixing characterization

The mixing time (t_m) has been calculated at the three nominal liquid velocities, without CO₂ gas injection, to identify the relationship between t_m and U_L in the characterized cultivation system. The data showed that, by increasing the liquid velocity from 0.17 m s⁻¹ (level I) to 0.60 m s⁻¹ (level II), the mixing time decreases from 814 s to 246 s. Whereas above $U_L = 0.60$ m s⁻¹ the slope of the curve decreases, and the t_m is not consistently reduced (194 s) (Fig. 16). The best fitting curve of the experimental data has an exponential trend (Fig. 16).

The computed energy consumption for the fluid handling at the three different liquid velocities was calculated to be 46, 27 and 38 W m⁻³, respectively. Therefore, the reported power consumption values suggest that working at U_L values above 0.60 m s⁻¹, the inflexion point of t_m and U_L curve, is energetically disadvantageous since mixing time remains comparable with the one measured at 0.60 m s⁻¹ (level II).

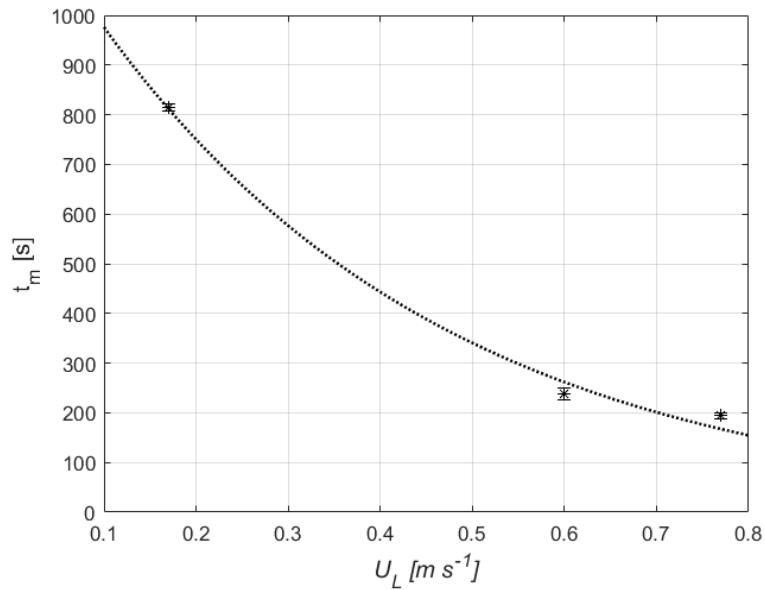


Figure 16: Influence of liquid flow velocity on mixing time. Data are shown as the average of three replicates \pm standard deviation. Dotted line represents the exponential fitting ($y = 328.9 \cdot e^{-0.814 \cdot x}$, $R^2 = 0.9946$) obtained with the software Matlab®.

The reactor hydrodynamic behavior of other flat panel PBRs described in the literature is based on different engineering solutions that affect hydrodynamic characteristics^{49,100}. The authors reported the trend of mixing time in correlation with the gas velocity which drives the liquid handling. In the PBR prototype here described, the photosynthetic loop can be assimilated mainly to a plug flow reactor, although a continued stirred situation may be assumed since the estimated Reynolds number within the alveoli ($Re \sim 10,000$) indicates a turbulent state. Meanwhile, the mixing tank can be described as a CSTR (Continued Stirred Tank Reactor). Despite the different liquid handling solution, adopted in this study, with respect to the reported literature, the t_m values measured at 0.60 (level II) and 0.77 $m s^{-1}$ (level III) fall into the ranges of mixing times reported in the above-mentioned works^{49,100}.

2.3.3 CO₂ mass transfer

Carbon dioxide uptake is one of the main target of microalgae cultivation technologies exploitation, therefore the CO₂ mass transfer coefficient ($k_L a_{CO_2}$) in the new PBR prototype was investigated. As described in [section 2.2.1](#), CO₂ is directly injected upstream of the circulation system and the bubbles are swallowed up and broken by the circulator to smaller sizes. Moreover, the gas circulates within

the fluid in the flat panels with a CO₂ bubbles residence time that is linked to the total length of the alveoli in the photostage loop (around 40 m).

The injection of CO₂ causes a reduction in the hydraulic flow rate since the gas flow interferes with the liquid handling of circulator, as discussed in [section 2.3.1](#). Therefore, $k_L a$ values were not measured for the CO₂ flow rates reducing the hydraulic flow below the 90% of nominal value (Table 2) and the results are reported in Table 3. As expected, the data showed a significant increase of $k_L a_{CO_2}$ values from $1.21 \cdot 10^{-5}$ to $2.99 \cdot 10^{-4} s^{-1}$ along with the increase of the CO₂ flow injected for each hydraulic flow. Experimental results indicate that circulator level II ($0.60 m s^{-1}$) achieved the highest mass transfer coefficient among the evaluated conditions. While the level III leads to a higher liquid flow velocity ($0.77 m s^{-1}$), it did not yield a proportional increase in the $k_L a_{CO_2}$ or overall system performance. Moreover, level III requires a higher energy consumption ([section 2.3.2](#)) without providing substantial advantages. Circulator level I, on the other hand, operates at an excessively low liquid flow velocity, limiting its applicability to the lowest CO₂ flow rates and consequently demonstrating the lowest mass transfer capabilities. Although an increase in the $k_L a_{CO_2}$ was observed at circulator level III under the highest gas flow rates ($1.08 NL min^{-1}$) - operating condition not feasible for the level II due to the significant liquid flow reduction discussed in [section 2.3.1](#) - the necessity of such a high flow rate is not necessary given the precise dissolved CO₂ control capabilities of the presented prototype. Consequently, based on the comparative analysis of mass transfer efficiency, energy consumption, and operational requirements, circulator Level II emerges as the most favourable operating parameter.

In the presented prototype, being the system's hydrodynamics based on a mechanical circulation of the liquid, there is no need to inject air to support the movement of the liquid culture and guarantee a certain degree of mixing and gas transfers. Thus, it is possible to inject only pure low CO₂ flow rates achieving a high solubilization in the photostage loop. In this way, CO₂ losses in atmosphere are limited, and the only cost to obtain an efficient mixing and gas transfer is the one associated to the hydraulic circulator, as in real scale application pure CO₂ comes already pressurized by previous industrial stages. In literature, few examples of $k_L a_{CO_2}$ experimental measurements were reported.

Table 3: Dependency of CO₂ gas-liquid mass transfer coefficient ($k_L a$) on the liquid flow velocities and CO₂ flow rates tested.

$k_L a_{CO_2} [s^{-1}]$			
CO ₂ flow rate [NL min ⁻¹]	Circulator level I $U_L = 0.17 \text{ m s}^{-1}$	Circulator level II $U_L = 0.60 \text{ m s}^{-1}$	Circulator level III $U_L = 0.77 \text{ m s}^{-1}$
0.06	$1.21 \cdot 10^{-5}$	$1.89 \cdot 10^{-5}$	$1.64 \cdot 10^{-5}$
0.12	$1.47 \cdot 10^{-5}$	$3.43 \cdot 10^{-5}$	$3.20 \cdot 10^{-5}$
0.48	n.d.	$1.30 \cdot 10^{-4}$	$1.24 \cdot 10^{-4}$
1.08	n.d.	n.d.	$2.99 \cdot 10^{-4}$

This configuration makes difficult to directly compare this PBR with other flat panel systems described in literature, in terms of hydrodynamics and mass transfer efficiencies. Nevertheless, comparisons could be possible by addressing the problem from an energy point of view, in terms of energy required per unit volume operating in the unit of time. The energy consumption related to the substrate handling was evaluated as effective power (at the wall socket) amounting to 27 W m^{-3} for level II of the hydraulic circulator, without any further cost associated to the CO₂ supply and stripping-out of O₂. On the contrary, in the majority of flat panel PBRs described in the literature, air is injected directly from the bottom of the flat-panels with the triple function of provide adequate mixing, CO₂ and favour the stripping-out of O₂. Therefore, the air supply parameter governs the energy consumption and the mass transfer capacity^{49,108}. A large volume of compressed air is therefore consumed to achieve the described triple function.

A power supply of 53 W m^{-3} was estimated by Sierra *et al.*, 2008⁴⁹ to reach a mass transfer rate high enough to avoid excessive O₂ accumulation. More recently, Li *et al.*, 2015⁹⁶ proposed a new design of flat panel PBR coupled to an external airlift module to overcome the major limitation of the mixing and improve the energy efficiency of the process by estimating a power supply of 31.6 W m^{-3} . However, the effective energy consumption of the system must include the efficiency of the associated air compressor, as also highlighted by Norsker *et al.*, 2012⁵¹. Therefore, direct comparisons with traditional flat-panel PBRs are difficult due to the absence of gross energy data concerning the power consumption of compressed air flat panels.

2.3.4 Light homogeneity

The lighting exposure (natural or artificial light) in photoautotrophic cultivation systems is a major factor influencing the performances of the process. Therefore, in the present study, we investigated the homogeneity of the artificial lighting system of the PBR prototype to assess the average light intensity at which microalgae cells are exposed. Light measurements on the surface exposed to the incident light have been used to build up a radiant matrix (Fig. 17). The computation of the different measurements on the surface established a mean incident light intensity of $120 \mu\text{mol}_{ph} m^{-2} s^{-1}$ with a light uniformity coefficient U_I of 40%. The trend of light distribution presents a wave shape, with the peaks corresponding to the fluorescent tubes positioning along the surface. Considering the light uniformity coefficient of 40%, a linear liquid velocity of $0.60 m s^{-1}$ (level II), and the length of each alveolus within the flat-panels (around $1.5 m$), microalgae cells take about 10 s to move between two adjacent light intensity peaks. Therefore, it can be concluded that light fluctuations within the photostage loop do not significantly affect the overall biomass growth performance.

The use of fluorescent tubes as artificial lighting system has some disadvantages. Fluorescent tubes are omnidirectional light sources, emitting at 360° . Therefore, only half of the emitted light is directed to the microalgae suspension, whereas the other half might need to be redirected to the desired area with the use of reflecting surfaces, requiring additional accessory parts. Moreover, their emitting light intensity, as well as the light spectrum quality, cannot be tuned if not by increasing the number of tubes (for the light intensity).

The energy consumption of the lighting system, measured as described in [section 2.2.8](#), was found to be $455 W$, a value which must be considered in order to estimate the global efficiencies of the cultivation system, and to investigate alternative artificial light sources to overcome the above-reported disadvantages reducing the energy requirements.

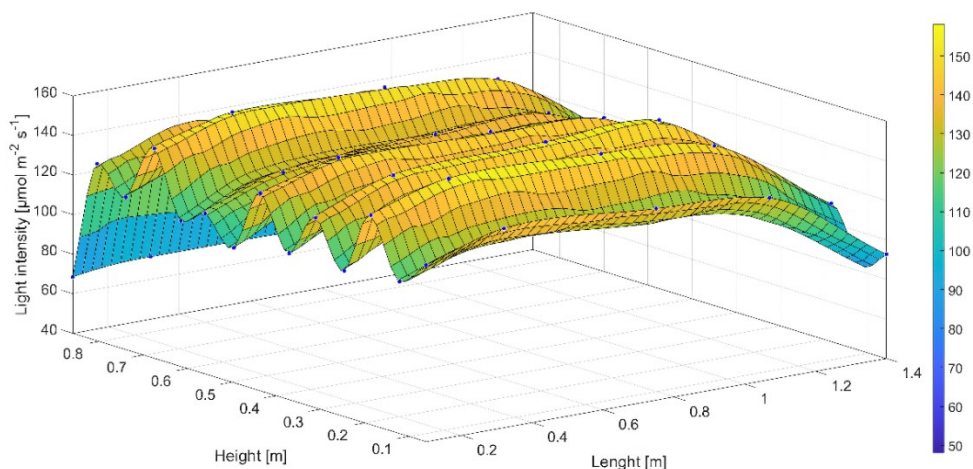


Figure 17: Graphical representation of the light intensity in a 3D space of the fluorescent source. $f(x,y)$ = piecewise cubic surface computed with the software Matlab® from p (structure coefficient), where x is normalized by mean 0.728 and std 0.4788 and where y is normalized by mean 0.4625 and std 0.2507.

2.3.5 Microalgae growth and CO₂ bio-fixation efficiency

Based on the data obtained for what concern the system's hydrodynamics and energy consumption, it has been decided to assess the growth of the green microalga *Acutodesmus obliquus* (*Scenedesmus obliquus*) operating at a liquid velocity of 0.60 m s^{-1} (level II) and with a CO₂ flow rate of 0.12 NL min^{-1} . As mentioned in previous sections, these hydraulic parameters have been identified among the best performing setups. Moreover, it has been decided to work at constant dissolved CO₂ concentration of 25 mg L^{-1} , corresponding to a carbon dioxide partial pressure (P_{CO_2}) of 0.017 bar . This value has been chosen to guarantee a relatively high CO₂/O₂ ratio, which may reduce the potential negative effects of O₂ accumulation via photorespiration, as suggested by ¹⁰⁹, and to assure a constant control on pH in the range between 7 and 7.5.

After 7 days of cultivation, the cells reached a final concentration of 1.9 g L^{-1} (Fig. 18). The analysis of the growth curves showed a mean daily volumetric productivity (P_x) of $0.21 \text{ g L}^{-1} \text{ d}^{-1} \pm 0.01$ ($n = 3$, where n is the number of replicates). The CO₂ fixation yield (η_{CO_2}), calculated as in Eq. 2.4 and based on elemental composition analysis of *A. obliquus* previously performed in our laboratory with the same cultivation setup (C 53.8 %, H 8.88 %, O 37.3% by weight), accounted for the 64% of the total CO₂ injected.

The cultivation of *A. obliquus* was successful in the PBR, and an axenic homogeneous cell culture could be developed to high cell concentrations. Using fluorescent microscopy, microalgae cells were found in good shape for the whole batch cultivation (data not shown), indicating no apparent shear stress despite the use of the mechanical circulating device set to obtain $U_L = 0.60 \text{ m s}^{-1}$. Finally, as shown in [section 2.3.2](#), the average light intensity on the surface of the flat panels was about $120 \mu\text{mol}_{ph} \text{ m}^{-2} \text{ s}^{-1}$, and the biomass yield on light energy ranged from 0.3 to 0.6 g mol^{-1} during the whole cultivation period, values comparable with data reported for several green microalgae grown in flat panel reactors ^{48,110}.

A recently published review by Lim and co-authors extensively analyzed the CO₂ bio-fixation results available in literature ¹⁰⁵. The authors analyzed several approaches to evaluate the effective CO₂ bio-fixation by microalgae culture and reported that most of the scientific literature investigated the CO₂ fixation only at laboratory scale. In this work, for CO₂ bio-fixation calculations we used the elementary analysis approach. Moreover, the experiments described in this work were performed on volumes higher than laboratory scale, and additionally a pure CO₂ stream was used to feed the PBR in a way that could be compatible with already available industrial streams. The obtained results place the new flat-panel PBR among the most promising prototypal technology to implement a microalgae CO₂ fixation approach at industrial scale. Furthermore, the hardware components of the PBR, equipped with a multi-probes system connected via transducer to an integrated PLC (see [section 2.2.1](#)), make this pilot-scale prototype already suitable for remote monitoring and control of cultivation parameters to incorporate the Internet of Things (IoT). This, as extensively highlighted in recent literature, is becoming a relevant aspect as both academic research and industry are gradually moving towards process automation and remote operation ^{111,112}.

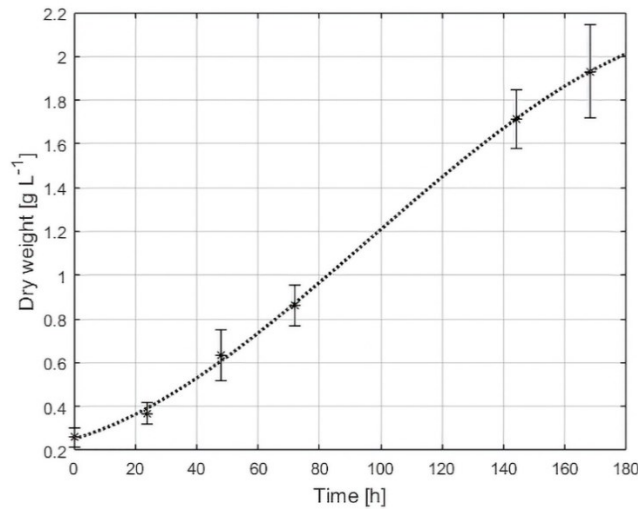


Figure 18: Biomass concentration of *Acutodesmus obliquus* in the flat panel photobioreactor. Stars represent the dry weight measurements \pm standard deviation ($n = 3$). Dotted line represents the third-degree polynomial interpolation ($R^2 = 0.9985$) obtained with the software Matlab®.

2.4 Conclusion

This chapter depicts the characterization of a new flat panel PBR prototype regarding the main hydrodynamic parameters, the CO₂ supply strategy and the artificial lighting system. An innovative liquid handling strategy based on pump-assisted circulation has been proposed and tested in this work. The liquid culture is moved by a centrifugal pump that allows appropriate culture mixing and enhance CO₂ mass transfer with a lower power consumption compared to the majority of flat panels described in the literature. The biological performances of the system have been successfully tested by cultivating the green microalga *Acutodesmus obliquus*, which showed a mean daily volumetric productivity (P_x) of $0.21 \text{ g L}^{-1} \text{ d}^{-1}$ and a biomass yield on light energy comparable to those reported for several green microalgae in flat-panel PBRs. Furthermore, the CO₂ bio-fixation efficiency was found to be higher (64 %) than those reported in literature for several microalgae species grown in large-scale setups. Taken all together, the energetic and biological performances of this pilot-scale PBR may constitute an important step toward the development of industrial-scale technologies to mitigate CO₂ while obtaining high quality microalgal biomass.

Chapter 3

Advanced design and characterization of a flat panel photobioreactor equipped with a customizable LED lighting system.

3.1 Introduction

Microalgae have become increasingly important as a source of biomass for various applications, including biofuels, animal feed, food, cosmetics, and dietary supplements. Compared to land plants, microalgae are better at fixing carbon dioxide and converting solar energy into chemical energy, and they can grow faster and do not compete with arable land for cultivation⁷²⁻⁷⁴. Closed systems allow for precise control of operating conditions and show higher biomass productivities compared to open systems, but they require higher capital and operating costs, as well as it is challenging to scale up their size while maintaining optimal culture and hydrodynamic parameters^{10,83}. The yield of microalgae growth processes strongly depends on the design and operative conditions of the PBR. Dark and light zones typically coexist inside photobioreactors, i) because microalgal cultures are optically dense and hinder light penetration, and ii) because systems are often designed in such a way as to have microalgae experiencing alternate light cycles. This requires the microalgae to move between light and dark zones at a frequency that is high enough to support growth and not remain in dark fluid dead zones too long up to suffer a decrease in photosynthetic activity. As such, a PBR must be well-designed from the standpoint of hydrodynamics. CFD (computational fluid dynamics) simulations have emerged as a low-cost and highly efficient strategy for designing microalgal growth equipment, as they can serve either the initial design stage of the PBR or the optimization of its operative conditions, eventually allowing one to reduce efforts on expensive and time-consuming experiments. CFD simulations can be used to obtain an accurate characterization of the flow field, possibly leading to the detection of a fluid dead zone, to get the statistics of shear

stress and light absorbance along microalgae trajectories, or to detect the sedimentation and adhesion dynamics. By using CFD, Belolhava *et al.*, 2021¹¹³ for instance evaluated the hydrodynamics of a hybrid horizontal tubular PBR, showing that even at large flow velocities, low-velocity regions, prone to solid settling, can be expected. By a similar approach, Wang *et al.*, 2021¹¹⁴ and Hinterholz *et al.*, 2019¹¹⁵ developed and optimized the internal structure of a bioreactor by introducing inclined baffles which were seen to improve the swirling features of the flow. Through Lagrangian cell tracking combined with a solar radiation transfer model, Laifa *et al.*, 2021¹¹⁶ related the overall growth rate to the broth velocity, as well as by applying CFD simulations, Zhang *et al.*, 2020¹¹⁷, studied the adhesion of cells and the biofilm growth on the walls of a bioreactor at varying surface roughness. Also, models aimed at coupling the bio-kinetics of microalgae growth and the equipment hydrodynamics have been devised^{118–120} and seem to compare well with experimental data.

Managing light is another fundamental aspect in the design of photobioreactors, as it plays a crucial role in the growth and productivity of microalgae or cyanobacteria. Precise control of light parameters such as intensity, duration, and spectral composition is essential to optimize the desired physiological responses in these photosynthetic organisms and the energy supply. The provision of light energy can be achieved through natural sunlight or the use of artificial lamps. Utilizing sunlight as a light source offers the advantage of being free and readily available in abundance. However, it also presents certain drawbacks, including the presence of location-specific day/night cycles, unpredictable weather conditions, and seasonal variations. These fluctuations in irradiance levels can be mitigated by implementing artificial lighting. By employing continuous and controlled illumination, productivity can be enhanced, as biomass is not lost during night-time periods^{14,15}. In the context of artificial lighting, the predominant choices are fluorescent tubes and light-emitting diodes (LEDs). LEDs offer numerous advantages compared to fluorescent tubes. They exhibit lower heat dissipation, resulting in reduced energy consumption, and possess a narrow emission spectrum, just to cite a few^{12,13}. The utilization of light by phototrophic microalgae relies on their specific pigment composition, primarily chlorophylls, carotenoids, and phycobiliproteins, characterized by different absorption properties across distinct spectral regions^{121,122}. Furthermore, microalgae and their pigments are gaining increasing commercial interest as a source of natural high-value products^{123,124}. The growth and metabolism of microalgae, including pigment content, can be influenced by the quality of light they receive, as determined by their spectral characteristics. Numerous studies have investigated the growth behaviour and

product formation of microalgae and cyanobacteria under various light conditions^{12,122,125,126}. Nevertheless, most of those studies have been conducted with monochromatic or dichromatic illumination with fixed colour ratios. Furthermore, such studies have been performed mostly at a lab scale in strictly controlled conditions, and to the authors' knowledge, no pilot-scale PBR equipped with multi-LEDs has been proposed so far.

The present work aims to propose a detailed characterization of a new semi-pilot scale prototype equipped with a multi-LEDs lighting engine. CFD simulations were carried out to characterize in detail the PBR's hydrodynamics. The study of the flow field in both the two constituent parts of the equipment, namely an alveolar flat panel and a mixing tank, was performed. CFD simulations were run in ANSYS Fluent 20.2 using a $k-\epsilon$ model for modelling turbulence, and numerical tracer experiments were run to infer the effect of the flow field on the species residence time and spatial distributions. Additionally, a description of the LED lighting engine is provided. The system allows us to unpack the entire visible spectrum with the use of 10 wave lengths, produced by different LEDs, evenly distributed along the structure. The analysis of the incident light distribution along the entire surface of the flat panels is also provided and commented on. Finally, the efficiency of the system has been tested by carrying out batch tests with two commercially relevant microalgae, phylogenetically distant and with different pigment composition and abiotic conditions requirements. For each microalga, a specific light spectrum composition has been applied based on the oxygen evolution response as a performance indicator of photosynthesis from the cells exposed to the different wavelengths. The promising biomass yields obtained with both species reflect the potential and versatility of the PBR here described. The possibility of monitoring all growth parameters, as well as the tuning of light intensity and quality, make this system an excellent platform for the study and growth at a semi-pilot scale of several targeted algae or desired products. Various considerations and suggestions, especially related to the system's fluid dynamics, are provided, and will help to further improve the proposed technology and to evaluate its possible use in an industrial scenario, in which the application of energy-efficient technologies is nowadays a priority.

3.2 Materials and methods

3.2.1 The flat panel photobioreactor

The design, hydraulic, and mass transfer characteristics of the flat-panel PBR used in this work have been described in Chapter 2¹²⁷. Compared to the PBR prototype reported in the Chapter 2 (Fig. 19A), the lighting hardware has been updated through the implementation of an own designed tuneable-spectrum LEDs lighting engine directly managed by PLC, interposed between the two panels, instead of the more energy-consuming fluorescent tubes.

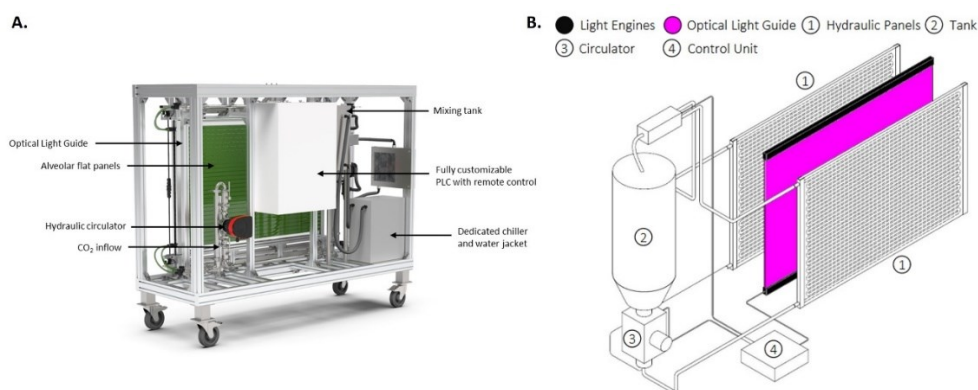


Figure 19: The alveolar flat-panel PBR. **A.** 3D isometric representation of the PBR. **B.** Schematic representation of the lighting engine. PLC: Programmable Logic Controller

3.2.2 LED lighting system

The lighting engine installed on the PBR is constituted by an innovative LED panel (patent number WO2020104895A1) engineered by MEG science (Milan, Italy), co-inventor of the system together with Arcobaleno Cooperativa Sociale (Turin, Italy) and the Polytechnic of Turin (Italy). Excluding the mechanical and control components, two elements can be identified as the system's main core: the light engines and the optical guide (Fig. 19B). The light engines are located at the upper and lower ends of the optical guide and are characterized by two water blocks that allow heat exchange between the electronic components (LEDs Printed Circuit Boards (PCBs)) and the external environment, using a forced water-cooled heat exchanger. This technical expedient serves to ensure operating temperatures below the safety junction temperature that characterizes each diode, increasing the efficiency and average lifetime of the individual LEDs. Each water block is

equipped with 3 metal core LED PCBs, each populated by 10 LED clusters containing 12 power LEDs (Luxeon CZ Colour Line, LUMILEDS, USA). The structure and configuration of this unit allow a spatially homogeneous distribution of the 10 discrete LEDs characterized by different peaks of dominant wavelength and 2 white light LEDs (not used in this work, as well as the Far-Red LEDs). The spectral range of the 10 dominant peak LEDs varies from 430 *nm* to 730 *nm*, while the two white LEDs are characterized respectively by a white with CCT (Correlated Colour Temperature) 4000 *K* and CCT 5000 *K*. It is, therefore, possible to vary the quality and intensity of the light spectrum directly through the PLC. However, as indicated in Table A.1 ([Appendix](#)), this configuration is not normalized in terms of radiometric power, leading to a difference in the furnished light intensity of the single wavelengths. This is due to the different spectral power distribution, and the related radiometric powers, of the considered LEDs, which nowadays constitutes a hardware limitation with red and blue LEDs considerably more efficient than other wavelengths. The optical guide is interposed between the two LED water blocks and ensures a homogeneous light distribution from the LEDs over the entire hydraulic panels' surfaces. The guide is made of polymethylmethacrylate (PMMA), with a length of 1500 *mm* and a height of 1120 *mm*, shaped in a 10 *mm*-thick sheet. Both the surfaces were laser-carved to obtain a pre-established pattern allowing the re-direction of light toward the hydraulic panels, assuring a certain degree of uniformity. Its geometry has been designed to allow an easy installation between the hydraulic panels in which the microalgae circulate and to reduce as much as possible the space between the emission source and the illuminated surfaces.

3.2.3 Computational Fluid Dynamics simulations setup

CFD computations were conducted by the Multiscale Modelling for Material Science and Process Engineering (DISAT – Polytechnic of Turin) research group under the guidance of Prof. Vanni. The CFD simulations were run using ANSYS FLUENT 20.2. The geometry of the reactor was created using ANSYS DesignModeler, whereas the meshes were created using the tool snappyHexMesh from OpenFOAM 5.0. Figure A.1 ([Appendix](#)) reports the geometry of the tank and some detailed views of the mesh used for the simulations. The flow is fed to the mixing tank through a cascade flow, and it flows out via the bottom outlet tube. The cascade is reproduced as a vertical cylindrical element of fluid with free slip at the lateral surface. The diameter of the inlet flow and the outlet tube are 2.5 and 2.6 *cm*, respectively. The top surface is the liquid-air interface, which stays at a constant

level during the operation with a height, measured from the bottom of the tank, equal to 30 *cm*. Figure A.2 (Appendix) illustrates the geometry of the alveolar flat panel. The fluid enters the panel from the bottom right, and it flows to the left along the horizontal direction, then passes through the hole (magnified in the inset of Figure A.2) and reaches the upper channel, where it inverts its direction and moves to the next hole. The zigzagging motion generated by the sequence of 28 horizontal channels allows the fluid to spend sufficient time in the illuminated region of the equipment, but also generates a distribution of the residence times of the different elements of the liquid. CFD simulations were restricted to the portion of the system shown in green in the Figure A.2, since the fluid dynamics of the whole panel can be reconstructed by replicating such simulation at each turn.

The meshes of the tank and the flat panel are composed of approximately $1.0 \cdot 10^6$ and $1.3 \cdot 10^6$ hexahedral cells, respectively. The side of each cell is approximately equal to 1 *mm*. The mesh quality was checked evaluating the cells' orthogonal quality, which was seen to be equal to 1 (on a scale from 0 to 1) in practically all the fluid domains. Grids of such resolution have shown to be able to accurately predict the velocity field, both in mixing tanks¹²⁸ and in ducts of rectangular cross section¹²⁹.

Since the CO₂ dissolves almost immediately in the circulating fluid, the process was modelled as single-phase flow. The fluid's properties and physical parameters were set by considering the culture medium as water. The inlet flow rates to the tank and the flat panel were set equal to 13.5 *L min⁻¹* and 6.75 *L min⁻¹*, respectively. The Reynolds number in the flat panel duct is about 8000 (based on the hydraulic diameter), well above the minimum value of 4000 required for the turbulence to occur¹³⁰. The tank inlet duct has a Reynolds number just above 10000, making also this a turbulent flow, when feeding the tank inlet cascade.

A Reynolds-averaged approach for the computation of the system hydrodynamics was resorted. Under these conditions, the equation of fluid motion reads as in Eq. 3.1 and Eq. 3.2:

$$\frac{\partial \bar{u}_i}{\partial x_i} = 0 \quad (3.1)$$

$$\rho \left(\frac{\partial \bar{u}_i}{\partial t} \right) + \frac{\partial}{\partial x_j} (\rho \bar{u}_i \bar{u}_j) = - \frac{\partial \bar{p}}{\partial x_i} + \frac{\partial}{\partial x_j} (\bar{\tau}_{ij} - \rho \overline{u'_i u'_j}) + \rho g_i \quad (3.2)$$

where $\bar{\tau}_{ij} = \mu \left(\frac{\partial \bar{u}_i}{\partial x_j} + \frac{\partial \bar{u}_j}{\partial x_i} \right)$ is the viscous stress tensor, μ the fluid viscosity, \bar{u}_i the velocity, \bar{p} the fluid pressure, and ρ the fluid density, and where the bars indicate time-averaged quantities. The fluctuating component of the fluid velocity is denoted by u'_i . The Reynolds stress term $\overline{\rho u'_i u'_j}$ was modeled as in Eq. 3.3:

$$-\overline{\rho u'_i u'_j} = \mu_t \left(\frac{\partial \bar{u}_i}{\partial x_j} + \frac{\partial \bar{u}_j}{\partial x_i} \right) \quad (3.3)$$

i.e., as proportional to the mean fluid velocity gradients and the turbulence viscosity μ_t . The two-equations $k - \varepsilon$ turbulence model was used for the closure of the set of equations. The turbulent kinetic energy k ($m^2 s^{-2}$) and the rate of energy dissipation ε ($m^2 s^{-3}$) were computed by solving the additional transport equations (Eq. 3.4 and 3.5):

$$\rho \left(\frac{\partial k}{\partial t} \right) + \frac{\partial}{\partial x_i} (\rho k \bar{u}_i) = \frac{\partial}{\partial x_j} \left(\left(\mu + \frac{\mu_t}{\sigma_k} \right) \frac{\partial k}{\partial x_j} \right) + g_k - \rho \varepsilon \quad (3.4)$$

$$\rho \left(\frac{\partial \varepsilon}{\partial t} \right) + \frac{\partial}{\partial x_i} (\rho \varepsilon \bar{u}_i) = \frac{\partial}{\partial x_j} \left(\left(\mu + \frac{\mu_t}{\sigma_\varepsilon} \right) \frac{\partial \varepsilon}{\partial x_j} \right) + c_{1,\varepsilon} \frac{\varepsilon}{k} g_k - c_{2,\varepsilon} \rho \frac{\varepsilon^2}{k} \quad (3.5)$$

where the turbulent viscosity is given by $\mu_t = \rho c_\mu \frac{k^2}{\varepsilon}$, and where the set of $c_{1,\varepsilon}$, $c_{2,\varepsilon}$, c_μ , σ_k and σ_ε are as given in the standard implementation of the $k-\varepsilon$ turbulence model of ANSYS Fluent.

No slip boundary conditions were imposed at all walls of the system, whereas a zero-stress condition was adopted for modelling the inlet cascade flow and the liquid-free surface of the tank. The pressure-velocity coupling was achieved with the SIMPLE algorithm and a second-order upwind spatial discretization scheme was used to solve all the transport equations. In this work, the $k-\varepsilon$ method used to describe turbulence is a Reynolds-Averaged Navier Stokes (RANS) technique that solves a time-averaged equation of motion, where the transient nature of turbulent fluctuations is absorbed by the Reynolds averaging. The averaged variables usually reach a stationary condition if the flow rate supplied does not vary over time, as is the case here. Hence, steady-state computations were performed. The simulations were iterated up to the point where the scales residuals of all variables between subsequent iterations stopped decreasing and reached an asymptotic value. This value was below 10^{-6} and, since additional iterations would not reduce the residuals

any further, to the authors' opinion a condition where all the variables, including the local one, have attained convergence, is reached.

Due to the extremely special geometry of the system, direct comparisons with literature results are difficult to obtain. Modelling single-phase mixing tanks is a classic problem in chemical engineering, where reliable simulations are normally obtained using models and grid densities similar to those used in this work¹³¹. With regard to the duct, the simulations of this work were checked by comparing the prediction of the friction factor far away from the curves, where the flow is developed, with the relationship reported fully by Schlichting, 1979 - chapter 20¹³², which is corroborated by the experimental data. However, the shape of the duct with U-curves of complex internal geometry makes it impossible to obtain full validation from literature.

It should be noted that a large number of experimental and modelling studies are available for motion in flat ducts of rectangular cross-section, but these are of little significance in the context of this work^{133–137}. In fact, these studies often focus on the ability to predict the secondary flows triggered by the anisotropy of turbulence in straight ducts (Prandtl's secondary flow of the second kind). These, however, do not significantly alter the averaged profiles compared to canonical wall-bounded flows¹³⁸, being of modest intensity, with transverse velocities of the order of 1% of the axial ones. The $k-\varepsilon$ method used in this work is unable to detect this particular type of secondary flow, which is triggered by the anisotropy of turbulence. It should be noted, however, that the relevant properties of the system, such as pressure drop and mixing in the panel, are dominated by the effects of the U-curves and the recirculation immediately following the curves, which is instead satisfactorily described by eddy-viscosity-based models such as the $k-\varepsilon$ ¹³⁹.

3.2.4 Microalgae-specific light spectra composition

The composition of the species-specific spectrum was based on the evaluation of the O₂ evolution response following cells' exposure to the individual wavelengths available on the PBR. More precisely, the cells of *A. obliquus* and *G. sulphuraria*, at a concentration of about 0.5 g L⁻¹, were directly exposed within the PBR at the individual wavelengths, each one adjusted to deliver about 30 $\mu\text{mol}_{ph} m^{-2} s^{-1}$, for 10 minutes after a 15-minute dark adaptation period and/or the time necessary for the O₂ concentration in the culture to be returned at equilibrium with the atmosphere. The averaged value of 30 $\mu\text{mol}_{ph} m^{-2} s^{-1}$ was chosen according to the current upper range limit of some of the single wavelengths (*i.e.*, 499.5 and 520 nm). Oxygen

evolution activity was recorded through the InPro 6000 Optical O₂ sensor located at the output of the panels. The ΔO_2 value recorded was then normalized by the light intensity for each wavelength. The final spectrum was built according to the wavelengths yielding net oxygen production, each of them set at a certain power percentage weighted for the corresponding yield of O₂.

3.2.5 Microalgae and cultivation conditions

Acutodesmus obliquus strain 276-3b, formally *Scenedesmus obliquus* (Turpin) Kützing, was obtained from the SAG Culture Collection of Algae (Göttingen, Germany), whereas *Galdieria sulphuraria* strain 074W was kindly donated by Prof. Antonino Pollio (University of Naples, Italy). The PBR was inoculated with BG-11 medium¹⁰³ for *A. obliquus* or Allen medium¹⁴⁰ for *G. sulphuraria*, and microalgae cells for a total volume (V_{PBR}) of 60 L, corresponding to a surface area-to-volume ratio (S_f/V) of 50 m⁻¹, and an initial cell concentration of ≈ 0.25 g L⁻¹ of dry weight. Each experiment was conducted in batch mode until the stationary phase was reached. The injection of CO₂ was carried out with a flow rate of 0.06 NL min⁻¹, keeping constant the CO₂ concentration threshold in the PBR at 25 mg L⁻¹ for *A. obliquus* and 15 mg L⁻¹ for *G. sulphuraria*, using the combination of solenoid valve and mass flow meter. The choice of key parameters for *A. obliquus*, such as temperature (23°C \pm 2) and pH (7.0-7.5), was done according to previous experiments performed within the same PBR structure equipped with fluorescent tubes, chosen among the most performing setups, as well as the spectrum-specific averaged photon flux density (PFD) on the panels' surface was set to 150 μmol_{ph} m⁻² s⁻¹ (12.96 mol_{ph} m⁻² d⁻¹), to have a fair comparison with the previously published results¹²⁷. On the other hand, the red microalga *G. sulphuraria* is a polyextremophile organism that has been extensively studied due to its ability to survive at low pH (as low as 0.2 for some strains)¹⁴¹, high temperatures (up to 57°C) and high osmotic pressure¹⁴². Therefore, the pH and temperature were adjusted to be 1.5-2.0 and 37.5°C \pm 2, respectively, according to several literature studies¹⁴³⁻¹⁴⁶. The spectrum-specific averaged PFD was set to 125 μmol_{ph} m⁻² s⁻¹ since, according to its benthonic nature, *G. sulphuraria* is considered extremely photosensitive, usually growing at low light intensities^{142,147}, with light inhibition already occurring above 200 μmol_{ph} m⁻² s⁻¹^{141,145}. The culture medium temperature was controlled for both the microalgae using a thermostat (Lauda IN 250 XTW, Germany).

3.2.6 Biomass concentration measurements

Microalgae growth was gravimetrically quantified as dry biomass concentration as reported in [section 2.2.3](#)¹²⁷. The biomass volumetric productivity P_x ($g L^{-1} d^{-1}$) was then calculated as Eq. 2.1. The volumetric productivity was then used to calculate the biomass yield on light $Y_{x/ph}$ [$g mol_{ph}^{-1}$] according to¹⁴¹ (Eq. 3.6):

$$Y_{x/ph} = \frac{P_x \cdot V_{PBR}}{A_{PBR} \cdot PFD} \quad (3.6)$$

where A_{PBR} (m^2) represents the total illuminated area (*i.e.*, $3 m^2$ considering both the panels).

3.2.7 Radiance matrix

The uniformity of incident light on both panels' exposed surfaces was determined as reported in [section 2.2.9](#)¹²⁷, with the light uniformity coefficient (U_I %) calculated as in Eq. 2.7.

3.3 Results and discussion

3.3.1 CFD

Figure 20 reports a characterization of the flow field in both a 3D and a 2D view for three different cross sections. For each of those, a velocity magnitude contour plot, and a representation of the velocity field, as obtained by streamlines, were reported. Cross section 1 passes through the inlet of the tank, but not through the outlet which is instead included in cross section 2. Cross section 3 is instead parallel to the liquid-air-free surface of the tank. From the pictures, it is apparent that the inlet flow is slowed down upon impact on the free surface, and it is deviated towards the bulk of the tank by the inclined bottom walls. This is visible both in the velocity magnitude contour plot of cross section 1 and in the fluid path lines reported in the 3D view. It is also apparent that in the bulk of the mixing tank, the fluid undergoes a large recirculation motion with a vortical region that takes up almost completely the tank space, both in the vertical and horizontal directions. A lateral bypass current traveling directly from the inlet to the outlet of the tank can also be observed. As it will be later discussed, these features of the flow field have a relevant effect on the fluid residence time distributions in the tank. In cross section 2 the outlet flow is shown; here it is observed that the fluid flows out of the tank with a velocity

that is close in magnitude to the inlet velocity, though with a velocity gradient that is unsymmetrical with respect to the tube centreline. This must be considered as a consequence of the lateral offset between the inlet and outlet flow.

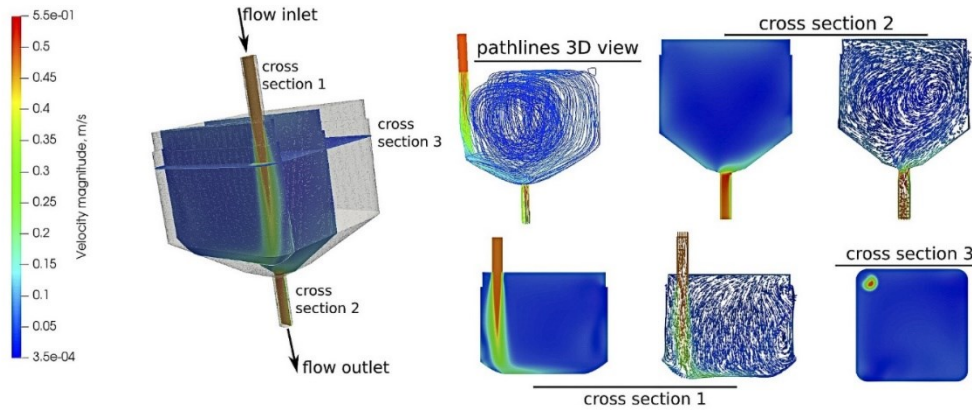


Figure 20: Visualization of the flow field in the mixing tank, by a contour plot representation of the velocity magnitude field and by fluid path lines. Three cross sections are reported together with a 3D representation.

Concerning the panel, our simulations were limited to the green-shaded region of Figure A.2. As the horizontal channel connecting two subsequent turns is long enough for the flow to be fully developed, an identical replication of the flow configuration at every turn of the panel may be expected. This point was confirmed by checking the identity of the simulated velocity distribution at the midplanes of the two subsequent horizontal channels.

In Figure 21 only the portion of the flow field close to the passage hole was reported, as this is the region where the flow presents features of more worth. Figure 21A. illustrates the velocity field by a contour plot representation. It is seen here that the flow travels almost undisturbed until it reaches the passage hole, where it is accelerated reaching large velocities, particularly in the converging region of the hole close to the wall separating two subsequent channels. The flow field representations of Figure 21B. and 21C. (streamlines and vectors of time-averaged velocity) make it also apparent that two vortical regions establish upstream and downstream of the passage hole. The first, visible in the bottom left corner, is a small, low-speed vortex, whereas the second, occurring downstream the passage hole, takes up a large vertical portion of the channel. However, this flow disturbance is seen to vanish completely at moderate distances from the passage hole. The vortex regions lead to an increase of the hydraulic retention time for the captured

particles (algae), thereby shifting their arrival time at the end of the panel. However, as it will be shown later (Fig. 23), this delay in particle arrival is on the order of minutes and can therefore be considered negligible. Conversely, the area of near-zero velocity corresponds to regions where slight biofilm formation has been observed on the reactor wall, although this phenomenon was found to be species-dependent.

From the inspection of the flow field just reported, it is apparent that a complex flow dynamics condition establishes in the two pieces of the equipment. To address this in some more detail, numerical tracer tests using non-reactive, dissolved species were performed. For the case of the tank, a step experiment was selected. Two non-interacting passive scalars were defined, one fed through the inlet flow at a constant concentration $c_{inlet} = c_0$, the second fed through the top liquid-free surface via a constant flux, such as a dissolved gas from the atmosphere. Within the tank, the tracer is transported by the convective motion of the fluid, only, with the diffusive transport disregarded. This is done to assess the effect of the flow features on species' transport and to rule out the effect of species' molecular diffusion. Thus, the transport equation reads as Eq. 3.7:

$$\frac{\partial c}{\partial t} + u_i \frac{\partial c}{\partial x_i} = 0 \quad (3.7)$$

where c is the passive scalar concentration and where u_i is the fluid velocity as calculated by solving the fluid momentum transport equation. For both scalars, the outlet concentration $c(t)$ as a function of time was measured.

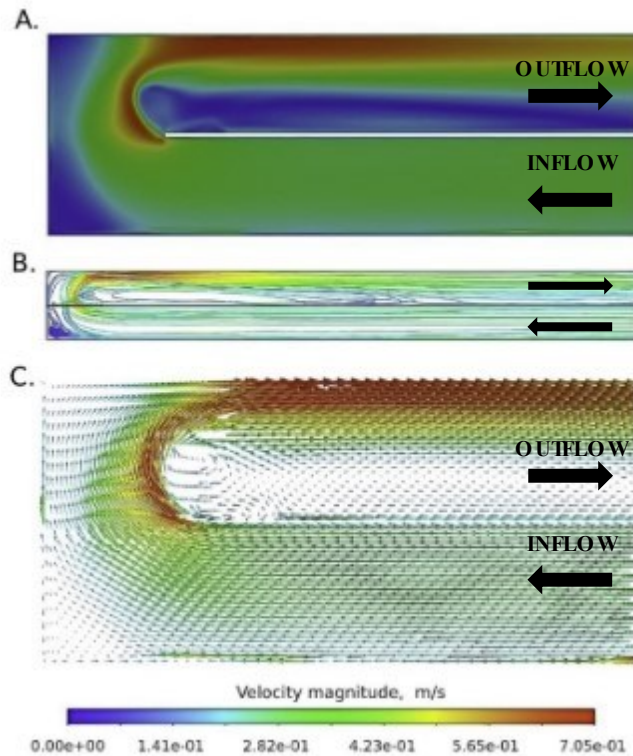


Figure 21: Visualization of the flow field in the flat panel. A. Velocity magnitude contour plot. B. Fluid path lines. C. Streamlines of the flow field. Each arrow is aligned with the local fluid velocity. The length and colour of the arrows are set according to the velocity magnitude.

The case of the release from the inlet is reported by the orange curve in Figure 22 together with a few snapshots of the spatial distribution of the tracer concentration. It is apparent that at the outlet the tracer concentration reaches, in a quite short time, a rather large value ($c \approx 0.32c_0$) which stays almost constant for approximately 25 s, and it then progressively approaches the asymptotic value ($c = c_0$). This response is the consequence of the inlet current that drags a large part of the tracer feed directly towards the bottom of the tank, from which it flows out practically by-passing the bulk of the fluid, as also visible in the concentration field snapshots at 10 and 100 s. The other part of the tracer feed flow is instead recirculated by the central vortex and spends a longer residence time in the tank. For comparison, the response of an ideal continuous stirred tank reactor is reported as a dotted line in the plot. The discrepancy between the two curves makes particularly apparent the by-pass phenomena just described.

The case of a uniform release from the tank-free surface is also reported in Figure 22. In this case, the concentration at large times reaches a lower value due to the dilution effect induced by the inlet flow. For this mode of release, no bypass phenomena occur, and the system's dynamical behaviour is very similar to the one that would be observed under perfectly mixed conditions. The uniform release from the liquid-free surface, together with the large vortical motion of the liquid bulk, distributes the tracer uniformly in the tank, making the outlet concentration increase more steadily until asymptotic conditions are reached, though with a delay compared to the perfectly mixed case. The signals of the outlet concentration make it possible to calculate the mean residence time τ of the tracers for the two different modes of release as in Eq. 3.8:

$$\tau = \frac{1}{c_0} \int_0^{c_0} t dc \quad (3.8)$$

This returned an average residence time equal to 86 s for the case of the release through the inlet flow, and 129 s for the case of the free surface release, with a difference compared to the average residence time under perfectly mixed conditions equal approximately to -8% and +37%, respectively.

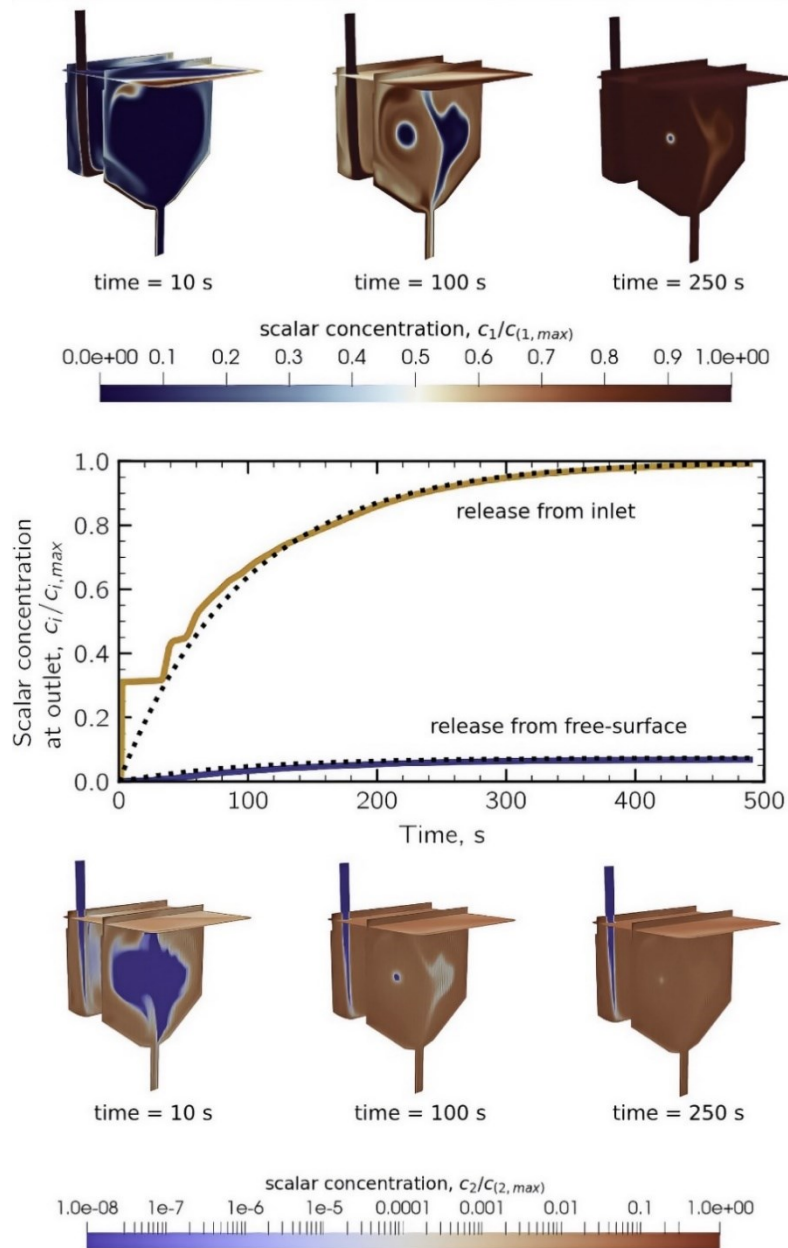


Figure 22: Results of the tracer experiments. Top) Concentration contour plot at three subsequent times for the case of a step release from the inlet. Centre) Concentration at the outlet as a function of time for the two modes of release. Bottom) Concentration contour plot at three subsequent times for the case of a step release from the liquid-free surface. The dotted lines report the outlet concentration that would be observed in perfectly mixed conditions.

Finally, in Figure 23 the distribution of the residence times in the flat panel, measured at the halfway of each channel, is reported. The measurement was done by an impulse experiment and by tracking tracer particles on the simulated domain. The results were extended to the whole flat panel by taking advantage of the system periodicity. It is seen that the residence time distribution of the particles is initially narrow, and it becomes wider after each channel. Finally, at the exit of the flat panel, three main peaks of decreasing height can be observed, approximately at 130 s, 140 s, and 165 s. This behaviour is in line with what could be inferred from the analysis of the velocity field reported in Figure 21, where it could be observed that the channel arrangement induces the formation of two recirculation regions (one downstream and one upstream of each passage hole) and the occurrence of a large velocity region near the converging region of the hole. These flow field features make the particles to be redistributed longitudinally at each elbow and to display a rather wide residence time distribution at the flat panel exit.

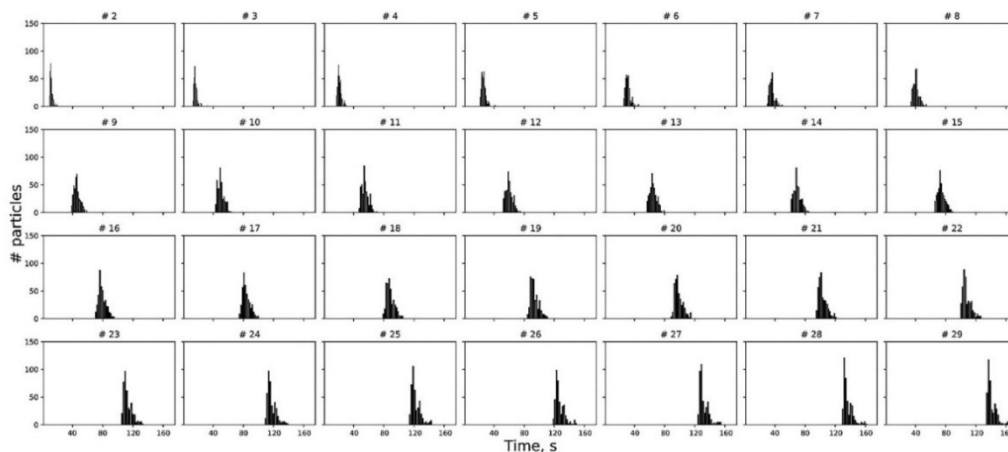


Figure 23: Residence time distributions measured at the halfway of the length of each channel of the alveolar flat panel as obtained by an impulse tracer experiment.

3.3.2 Light spectra composition

Although light absorption is wavelength-dependent, every PAR photon absorbed by the antennae can be used in the reaction centres to induce charge separation with the same efficiency, and results in an equal photosynthetic output. Nevertheless, the absorption bands of each pigment are different and, consequently, only certain wavelengths in the PAR region are effective for productive algal photosynthesis¹⁴⁸. Red light, with a narrow spectrum of 600–700 nm, is usually reported as the optimal

wavelength for the photosynthetic growth of most algal species^{14,122,149,150}. This is primarily because the most abundant pigments in most species are chlorophylls which can more efficiently absorb red light compared to other light wavelengths¹⁵¹. However, due to its longer wavelength, the low-energy red light poorly penetrates high-density or deep cultures. Therefore, the cultures should be well mixed or kept at low concentrations under these light conditions¹⁵². On the other hand, blue light, with its shorter wavelength, has a higher probability to trigger photo-inhibition by striking the light-harvesting complexes due to its high energy content^{150,153}. Overall, as reported in several works, the different wavelengths affect the cells' metabolism, by either enhancing the growth or the accumulation of specific compounds, acting differently according to the microalgae species^{122,126,154–158}. The experiments described in this section aimed to assess, for each microalga used, the optimal conditions in terms of light quality. This ideal light composition was investigated by measuring the oxygen evolution response as a performance indicator of photosynthesis from the cells exposed to the different wavelengths directly within the PBR, and thus when cultivated on a large scale. In this way, the resulting spectra represent the combination of wavelengths, rather than using only monochromatic lights, weighted based on the algae's ability to trigger redox reactions within the chloroplast. Additionally, the possibility of qualitatively and quantitatively regulating the provided individual wavelengths may be a useful strategy to investigate and minimize the energy consumption associated with the use of artificial light. The microalgae growth rates were then evaluated directly with the final ideal spectra, rather than testing the growth at each wavelength available in the PBR.

Figure 24 shows the ΔO_2 values obtained using the methodology described in the [section 3.2.4](#). Not surprisingly, the blue and red spectral regions have the largest impact on photosynthesis in green algae (Fig. 24A.), due to the large number of molecules of chlorophyll *a* (*Chl a*) and chlorophyll *b* (*Chl b*) in the light-harvesting complexes (*LHCs*). From Fig 24A. it can be noted as the green (520 nm) and orange (602 nm) lights do not lead to positive oxygen production. For the green light, the ΔO_2 is slightly negative, suggesting that the light at 520 nm induces electron transfer, but most probably the moles of photons given are not enough to reach the compensation point of photosynthesis. For instance, the light at 602 nm shows very negative ΔO_2 values, as there is a hardware limit linked to the fact that the photon flux at this wavelength is very small due to hardware limitations (around $6 \mu\text{mol}_{ph} \text{m}^{-2} \text{s}^{-1}$ at the highest power). So, this suggests no photosynthetic electron transfer and thus only respiration occurring when applying only this light wavelength. For this reason, the ΔO_2 values that occurred at 602 nm can be used as a reference for

the cell's respiration. Fig. 24B. shows the correspondent spectrum used for *A. obliquus*.

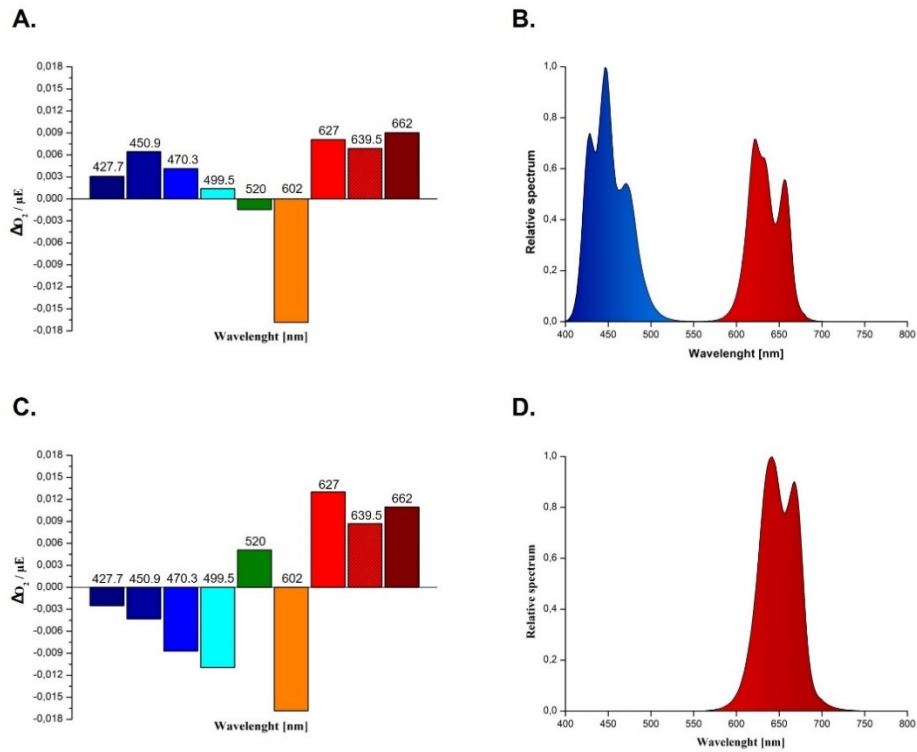


Figure 24: Light spectra customization. A. Wavelength-specific normalized oxygen evolution response (ΔO_2 [$mg L^{-1}$] / μE [$\mu mol_{ph} m^{-2} s^{-1}$]) of *A. obliquus*. B. Resultant final spectrum employed for *A. obliquus*. C. Wavelength-specific normalized oxygen evolution response of *G. sulphuraria*. D. Resultant final spectrum employed for *G. sulphuraria*. (kindly refer to [section 3.2.4](#)). Graphs were produced with the software OriginPro8.5®.

In contrast to green algae, red algae, as well as cyanobacteria, possess water-soluble Phycobilisomes (PBS) as major photosynthetic light-harvesting complexes. In *G. sulphuraria*, the PBSs are composed exclusively of allophycocyanin and (mainly) (C-) phycocyanin (C-PC) phycobiliproteins, with the C-PC having a single absorption maximum at $\approx 620 nm$ ¹⁵⁹. Furthermore, as widely reported in the literature, cyanobacteria and red algae possess low photosystem II / photosystem I (PSII/PSI) ratios, with the core complexes of PSII usually incorporating less *Chl a* than PSI cores^{160,161}. Moreover, unlike green algae, *G. sulphuraria* also lacks *Chl b* and instead has zeaxanthin as its major xanthophyll¹⁶². In accordance with its photosynthetic apparatus, *G. sulphuraria* showed no positive oxygen production

when illuminated with all the blue wavelengths (Fig. 24C.). The wavelengths resulting in the highest positive ΔO_2 were 627 nm and 662 nm, and in less extent 639.5, being the first two closer to the maximal absorption peak of *C-PC* and *Chl a*, respectively. Although *Chl a* is not present around *PSII*, it provides the energy along the *C-PC* to *PSI*, therefore enhancing electron transfer between the two photosystems. Unlike *A. obliquus*, also green light (520 nm) lead to positive oxygen evolution. Despite this, it has been decided to not include it in the correspondent spectrum since (Fig. 24D.), as previously reported, the cultivation process appears to not require a green or blue fraction to achieve optimal biomass productivity¹²². This would also reduce the energy consumption related to the artificial lighting system since in this prototype each LED is associated with a dedicated electric transformer. As for the light at 602 nm, the same considerations for *A. obliquus* can be done, reflecting the need for adequate hardware modifications if the effects on photosynthesis of this wavelength need to be further investigated.

3.3.3 Light homogeneity

Light availability in photoautotrophic microalgae cultivation is of primary importance for the overall process performance. Especially when employing artificial light, it is important to evaluate the light distribution along the photo-exposed surfaces to better characterize the amounts of photons and times at which microalgae cells are exposed. As previously investigated for a fluorescent tube light source, also in this work the light measurements on the exposed surfaces have been used to build up a radiant matrix for the two composed spectra used. The data were then computed as described in [section 3.2.7](#), obtaining an averaged *PFD* of 150 $\mu\text{mol}_{ph} m^{-2} s^{-1}$ and 125 $\mu\text{mol}_{ph} m^{-2} s^{-1}$ for *A. obliquus* and *G. sulphuraria*, respectively, as well as a light uniformity coefficient U_I of 70 % (Fig. 25A.) and 48 % (Fig. 25B.). The considerable uniformity difference between the two spectra may be ascribed, as already addressed in the [section 3.2.2](#), to the fact that the individual LEDs are distributed uniformly in clusters along the whole PCBs, but their distribution implies an unevenness from the emissive point of view. This is most evident from Fig. 25B., where the composed spectrum for *G. sulphuraria* is characterized by only 3 wavelengths, and therefore by a lower resolution along the entire optical guide. This non-uniformity, with an important gradient of light intensity ranging from 250 to 50 $\mu\text{mol}_{ph} m^{-2} s^{-1}$ along the surface of the hydraulic panels, may be overcome by changing the PCBs components, replacing the unintended wavelengths with a greater population of LEDs more uniform for each cluster. For the sake of simplicity, in this work, the averaged *PFDs* have been

considered for the calculations of the biomass yields on light. Nevertheless, as pinpointed by Blanken *et al.*, 2016⁵² the light distribution over the reactor surface has a significant influence on the growth rate, as high light will result in increased photosaturation. Further investigations on the growth kinetics with respect to the light distribution described in this section are currently ongoing.

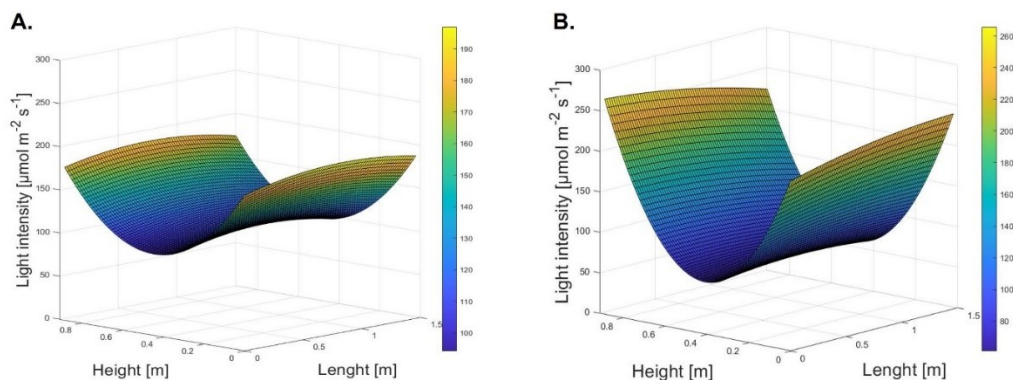


Figure 25: Graphical representation of the light intensity in a 3D space of the LEDs lighting source. *PFDs* measurements were interpolated by the Linear model Poly22 of the Curve Fitting Tool ($f(x,y) = p00 + p10*x + p01*y + p20*x^2 + p11*x*y + p02*y^2$ where x and y are the optical guide's length and height for the *PFD* sampling points, and $p(n)$ the fitted coefficients) of the software Matlab®. A. Light intensity distribution for the light spectrum employed for *A. obliquus*. The goodness of fit: SSE = 320.3, $R^2 = 0.972$. B. Light intensity distribution for the light spectrum employed for *G. sulphuraria*. The goodness of fit: SSE = 70.2, $R^2 = 0.995$.

3.3.4 Microalgae growth

In this chapter, the behaviour of PBR's fluid dynamics as well as the influence of the composed spectra on the biomass productivity of the two different microalgae (*A. obliquus*, *G. sulphuraria*, Figure A.3 – [Appendix](#)) was investigated²⁶. After 7 days of cultivation, the *A. obliquus* cells reached a final concentration of 2.305 g L^{-1} (Fig. 26A.). The analysis of the growth curves showed a mean daily volumetric productivity (P_x) of $0.295 \text{ g L}^{-1} \text{ d}^{-1} \pm 0.03$ ($n = 3$). The biomass yield on light energy was found to be on average $0.58 \text{ g mol}_{ph}^{-1}$ during the exponential phase, a value between the highest found in the literature for several green microalgae^{48,110}, although continuous experiments should be performed to address consistent estimations of this value. Nevertheless, to the authors' opinion, there is ample room for improvement, especially considering that in this work the batch experiments were conducted with a relatively low averaged light intensity ($150 \text{ } \mu\text{mol}_{ph} \text{ m}^{-2} \text{ s}^{-1}$).

Overall, the results obtained in this experimental campaign are slightly higher than what was reported in the chapter conducted with fluorescent lights, where the average light intensity on the panels' surface was found to be $120 \mu\text{mol}_{ph} m^{-2} s^{-1}$. This confirms the suitability of using the composed optimized spectrum for *A. obliquus*.

The red microalga *Galdieria sulphuraria* is nowadays considered one of the most promising biotechnological platforms for food and feed applications, due to its peculiar polyextremophile characteristics, favouring a selective environment that prevents contaminations, as well as its high content of proteins, insoluble dietary fibers, and antioxidants^{143,163}. Moreover, its amino acid profile is particularly noteworthy, as it contains a higher proportion of essential sulphur amino acids compared to *Chlorella*, *Spirulina*, and soybean protein¹⁶⁴.

In this work, it has been decided to assess the photoautotrophic growth of *G. sulphuraria* strain 074W, one of the most performant autotrophic strains¹⁴³, to show the versatility of the presented PBR to investigate and achieve high biomass growth even with extremophiles, far from common green microalgae. After 16 days of cultivation, the cells reached a final concentration of $3.28 g L^{-1}$ (Fig. 26B.). The analysis of the growth curves showed a mean daily volumetric productivity P_x of $0.22 g L^{-1} d^{-1} \pm 0.03$ ($n = 3$). Although the observed P_x may seem quite low compared to other reported autotrophic batches^{141,165}, it is noteworthy pinpoint that the light intensity used is relatively low as well as, to the author's knowledge, this work is one of the few studies where *G. sulphuraria* growth was conducted at real scale. Indeed, the biomass yield on light energy was found to be on average $0.45 g mol_{ph}^{-1}$ during the exponential phase, a value in accordance with what has been found by Canelli and co-authors¹⁶⁶ in a 17 L annular column PBR (*G. sulphuraria* strains ACUF 064 and SAG 108.79), and close to the highest ($0.5 - 0.65 g mol_{ph}^{-1}$) reported for *G. sulphuraria* (ACUF 064 and 074G) grown in autotrophic conditions at lab-scale^{141,164,165}. Taken together, the results obtained show the potential of the presented PBR prototype to achieve relatively high biomass concentrations, at a real scale, with more microalgae belonging to different phyla. Furthermore, the adopted strategy for the wavelength-specific spectra composition turned out to effectively achieve comparable yields on light obtained at the lab scale, especially considering *G. sulphuraria*. This aspect is relevant as, considering the cost of artificial lights, the possibility of choosing the optimal wavelengths according to the microorganisms' quantum requirements may strongly reduce the energy losses associated with, e.g., blue-to-yellow light conversion in white LEDs, and the overall electric input. Nevertheless, the authors are in accordance with the fact that, due to

the increase of the overall costs and the negative energy balances, the electrical energy required for microalgae cultivation employing artificial light should be generated as ‘green’ energy instead of that derived from exploiting fossil fuels ¹⁴, or alternatively be used in compensation of sunlight to ensure a 24h production.

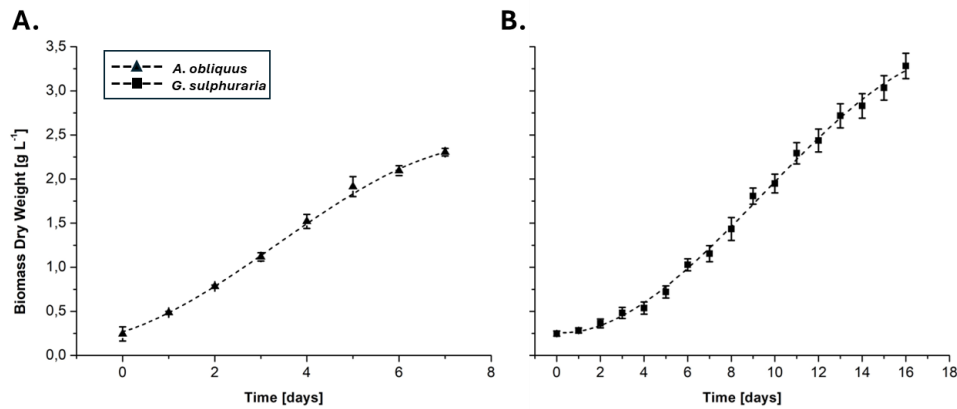


Figure 26: Photoautotrophic batches. A. Biomass concentration of *Acutodesmus obliquus* (black triangles) in the flat panel photobioreactor. B. Biomass concentration of *Galdieria sulphuraria* (black squares) in the flat panel photobioreactor. Triangles and squares represent the dry weight measurements \pm standard deviation ($n = 2$ *A. obliquus*, $n = 3$ *G. sulphuraria*). The dotted lines represent the third-degree polynomial interpolation ($R^2 = 0.999$ *A. obliquus*, $R^2 = 0.997$ *G. sulphuraria*) obtained with the software OriginPro8.5®.

3.4 Conclusion

In conclusion, the detailed characterization of a novel flat-panel PBR equipped with a LED lighting system is proposed. From the CFD analysis, it has been observed that the system hydrodynamics has several peculiar features which must be expected to determine the statistics of light and flow field sampling by the microalgae. In the mixing tank, two main regions of interest were observed: a vortex occupying almost completely the bulk of the tank, and a rather large lateral by-pass current traveling directly from the inlet to the outlet, counting for approximately 30% of the inlet flow and having a short residence time compared to what is obtained under perfectly mixed conditions. Also, the flat panel was seen to have a peculiar feature: close to the passage hole between two subsequent channels, the fluid was accelerated and two vortical regions were observed, causing the axial dispersion of the particles and a distinctive behaviour of the distribution of the residence times. Overall, the CFD analysis returned several useful indications for the technical optimization of the system and put the basis for a few further studies.

Among these, the use of internal baffles or deflectors of the fluid flow will be considered, as these can improve the mixing and mass transfer performance of the equipment.

The PBR has been equipped with a peculiar LED system capable of unpacking the entire visible spectrum. The possibility to dynamically change the light spectrum and intensity allows a high degree of customization of the cultivation process. This has been demonstrated by cultivating two completely different microalgae strains characterized by different growth parameters and spectral requirements. The biomass concentrations and yields achieved with both the strains, for which specific spectra were built, were perfectly in line with the data reported in the literature. These highlight the effectiveness of the adopted strategy for light management, which includes precise control of the light intensity and wavelength, and showcase the high efficiencies achieved by the PBR, with still ample room for improvement also considering the low light intensities applied. The peculiar light management features would also open the investigation of wavelength-specific effects on biomass composition at a pilot scale.

Chapter 4

Hybrid modelling of light-limited microalgae growth

4.1 Introduction

Microalgae, harnessing the power of photosynthesis to convert water and carbon dioxide into sugars through light energy, represent a promising avenue for sustainable biomass production. The growth of microalgae in photobioreactors hinges on accurate modelling, which traditionally involves complex frameworks requiring extensive experimental data for parameter determination. Recently, Blanken and co-authors⁵², proposed a generally applicable kinetic model to predict light limited microalgal growth. This model combines a mathematical description for photoautotrophic sugar production with a description for aerobic chemoheterotrophic biomass growth, for which the theory has been described in [Chapter 1 – section 1.7](#).

The established model, combining the Lambert-Beer Law, Jassby and Platt description of photosynthetic sugar production⁶⁸, and Pirt's balance for chemoheterotrophic growth⁶³, offers an accurate representation of microalgae metabolism while maintaining the simplicity of the model formulation and minimizing the parameters needed. The parameters required as input for the above-described model to predict the specific growth rate can be divided into two categories: i) measurable characteristics of microalgae and ii) process parameters. The measurable parameters may be obtained from literature for especially the most common green microalgae and include: molar mass of the microalgae (M_x); specific light absorption coefficient per wavelength ($a_{x,\lambda}$); sugar yield on photons ($Y_{s/ph}$); biomass yield on sugar ($Y_{x/s}$); maintenance-related specific sugar consumption rate (m_s); and maximal specific sugar production rate ($q_{s,m}$). The process parameters depend on culture conditions and include: biomass concentration (C_x), wavelength specific incident light intensity ($I_{ph,\lambda}$), and reactor depth (L).

The equations necessary to predict the microalgae specific growth rate are the following:

$$I_{ph}(z, \lambda) = I_{ph,\lambda}(0) \cdot e^{(-a_{x,\lambda} \cdot C_x \cdot z)} \cdot d\lambda \quad (4.1)$$

$$q_{ph}(z, \lambda) = \sum_{\lambda=400}^{\lambda=700} a_{x,\lambda} \cdot I_{ph}(z, \lambda) \quad (4.2)$$

$$q_s^c(z) = q_{s,m}^c \cdot \tanh\left(\frac{-q_{ph}(z) \cdot Y_{s/ph}^c}{q_{s,m}^c}\right) \quad (4.3)$$

$$q_s^c = \frac{\int_0^L q_s^c(z) \cdot dz}{L} \quad (4.4)$$

$$\mu = (q_s^c - m_s) \cdot Y_{x/s} \quad (4.5)$$

Blanken and co-authors validated the model for two different green microalgae by adopting a Monte Carlo approach based on input parameters derived from the literature. But since these parameters are measurable characteristics of the microalgae, it is possible to modify the model for other strains by performing several dedicated experiments to derive those parameters. These experiments include: 1) maximal specific growth rate (μ_m) or maximal sugar production rate ($q_{s,m}$); 2) specific absorption coefficient ($a_{x,\lambda}$) being measured with a dedicated spectrophotometer mounting an integrated sphere; 3) Molecular weight from elemental analysis; 4) Biomass yield on sugar ($Y_{x/s}$); 5) Specific sugar consumption rate for maintenance (m_s); 6) Sugar yield on photons ($Y_{s/ph}$), which for the sake of simplicity can be theoretically considered with a value of 0.09 or 0.10 $mol_s mol_{ph}^{-1}$.

In this PhD work, some of the above-described parameters have been identified for the species *Galdieria sulphuraria*, for which still few of those parameters can be retrieved from literature. Once all the parameters were identified from the experiments and/or from the literature, the described model has been implemented to predict the growth of *G. sulphuraria* in the flat-panel reactor described in Chapter 2, assuring the best cultivation conditions for this species (thus intended to have light-limited growth), employing the optimized LED spectrum as described in Chapter 3.

The overarching goal was to validate the reliability of the existing microalgae growth model for *G. sulphuraria* grown on a pilot scale reactor, while simultaneously introducing a methodology that reduces the number of experiments

for parameter acquisition. Particularly, a new methodology for the identification of the m_s , one of the most challenging parameters to identify experimentally, is provided. Indeed, in Blanken *et al.*, 2016⁵² the authors retrieved also this parameter from the literature available, fitting the model based on a Monte Carlo approach by varying the m_s , as well as all the other input parameters, within a certain range⁵². Nevertheless, the specific sugar consumption rate for maintenance is somehow dependent, given appropriate culture conditions, on the internal sugar concentration, as depicted by Blanken and co-authors¹⁶⁷. Here, the authors applied the following equation to retrieve the maintenance related sugar consumption:

$$m_s(C_s) = m_{s,m} \cdot \left(1 + e^{(d-a \cdot b \cdot f_{s/b})}\right)^{-1/b} \quad (4.6)$$

where C_s is the accumulated sugar biomass, $m_{s,m}$ is the maximal maintenance related sugar consumption rate retrieved always from the literature, $f_{s/b}$ the internal sugar fraction, and a , b and d are the fitted parameters on experimental data. It is worth mentioning that in their study, the authors adopted a distinction between functional biomass and accumulated sugar biomass, to describe the diurnal carbon-partitioning between storage and biomass growth, to fully understand monoalgal biofilm productivity where light starvation occurs deep in the biofilm, similarly to what happens to microalgae cultivated under natural sunlight conditions, and thus day-night cycles. This resulted in a series of differential equations which may increase the complexity of calculations on and industrial point of view.

By assuming that in the flat-panel reactor microalgae are always exposed to light, in this work no such partitioning may be necessary, and a similar Richards' equation for the m_s identification (Eq. 4.6) has been implemented into the model, in direct relationship with the biomass accumulation over time during batch cultivations. Additionally, being $m_{s,m}$ currently unknown for *G. sulphuraria*, and again difficult to retrieve experimentally, also this parameter is computationally fitted with the experimental data. A schematic representation of the developed model is reported in Figure A.4 ([Appendix](#)).

Additionally, the chapter also investigates the impact of the absorption cross section ($a_x/a_{x,\lambda}$) on the overall process. As discussed in [Chapter 1 - section 1.7.1](#), $a_x/a_{x,\lambda}$ represents the microalgae light-absorbing surface, and is fundamental to the estimation of the light penetration within the PBR, as well as the calculation of the specific photon absorption rate (q_{ph}). The $a_x/a_{x,\lambda}$ also reflects the photoacclimation process, wherein microalgae adjust their pigmentation in response to light conditions. Therefore, it varies according to the biomass concentration and light

exposure. It follows that, it should be kept constant if chemostat cultivations are performed, whereas it varies in batch conditions. The analysis of this parameter necessitates the use of scan spectrophotometer equipped with a dedicated integrated sphere, a specific equipment which may not be always available in research laboratory and industry. Therefore, the following question arises: is it always necessary to experimentally determine the $a_x/a_{x,\lambda}$?

Lastly, the model has been applied by considering both the wavelength-resolved characteristics of the supplied light ($I_{ph,\lambda}$), in conjunction with the absorption cross section $a_{x,\lambda}$, and the PAR-averaged parameters I_{ph} and a_x . For the latter, Eq. 4.1 and 4.2 have been modified as follows:

$$I_{ph}(z) = I_{ph}(0) \cdot e^{(-a_x \cdot c_x \cdot z)} \quad (4.7)$$

$$q_{ph}(z, \lambda) = a_x \cdot I_{ph}(z) \quad (4.8)$$

This comprehensive approach allows for the evaluation of whether the adoption of wavelength resolution, although accounting for variations in light penetration across the different wavelengths and thus theoretically more precise, is justifiable compared to the use of averaged parameters. The consideration extends to assessing the computational intricacy and power requirements, at least referring to the PBR system used in this study and under the specific growth conditions adopted for *Galdieria sulphuraria*. The core Python scripts are available as annexes to this PhD thesis.

4.2 Materials and Methods

4.2.1 Batch cultivations

Several batch cultivations were conducted by adopting the same culture conditions and light spectrum described in [Chapter 3 - section 3.2.5](#). Two main light supply strategies have been adopted: i) constant illumination at averaged $125 \mu\text{mol}_{ph} \text{m}^{-2} \text{s}^{-1}$; ii) increasing light intensity over time to assure an optimal light supply rate always in the range $3 - 7 \mu\text{mol}_{ph} \text{g}^{-1} \text{s}^{-1}$ as stated by Abiusi and co-authors¹⁴¹. All the batch experiments lasted between 10 and 16 days.

4.2.2 Sample measurements (C_x , $a_x/a_{x,\lambda}$)

Microalgae growth was gravimetrically quantified as dry biomass concentration (C_x) as reported in [Chapter 2 - section 2.2.3](#). The wavelength-dependent absorption cross section ($a_{x,\lambda}$) was derived from absorbance measurements taken using a UV-VIS spectrophotometer (Shimadzu UV-2600i, Japan) equipped with an integrating sphere (ISR-2600plus) according to de Mooij *et al.*, 2015¹⁶⁸. The averaged absorption cross section a_x was then calculated as in Eq. 1.23 ([Chapter 1 - section 1.7.2](#)).

4.2.3 Elemental composition

For the evaluation of *G. sulphuraria* elemental composition, fresh biomass from three different batch experiments was collected by centrifugation, freeze-dried at -85°C , and then freeze-dried. The samples were weighted in 2 mg foil capsules and then introduced into a CHNS analyzer (Flash 2000 CHNS/O Analyzer, Thermo Fisher Scientific), to evaluate the C, H, N and S content after rapid and complete combustion at 950°C in oxygen excess followed by separation of gaseous compounds into gas chromatographic column. The results, expressed as element %, were then translated into 1 mol_x of microalgae biomass usually represented by the formula $\text{CH}_x\text{O}_x\text{N}_x\text{P}_x$.

4.2.4 Computational methods

4.2.4.1 Data-driven model and training

This model employs five equations to calculate the average specific growth rate within a microalgae culture inside a photobioreactor, and the equations already introduced are written such that they depend on culture depth. The local light intensity ($I_{ph}(z)$) is used to calculate the local specific photon absorption rate ($q_{ph}(z)$) which is subsequently coupled to the sugar production and integrated over the reactor to acquire the average specific sugar production rate (Eq. 4.4). This integration assumes therefore that all the microalgal cells behave at the same way along the culture depths. The partitioning of the produced sugar between functional biomass (anabolism), growth-related respiration (catabolism), and maintenance-related respiration is described by Eq. 4.5.

It is worth to mention that some assumptions have been made: i) microalgae within the PBR used are subject to 24h illumination (although as from Chapter 2 and 3 the PBR configuration present a mixing tank and a certain degree of light/dark cycles);

ii) The incident light angle is exactly perpendicular to the whole panels' surface;
 iii) the spatial distribution of the incident light is perfectly homogeneous, since the averaged light intensity over the panels' surface has been considered (please refer to [Chapter 3 - section 3.3.3](#)), and therefore photosynthesis dynamics do not change over the entire light exposed surface.

All batch experiments were partitioned into train and test sets. The train set comprised four batches conducted under constant illumination, except for one variation, while the test set consisted of eleven batches, primarily characterized by increasing light intensity.

$Y_{x/s}$ was set equal to $0.58 \text{ mol}_x \text{ mol}_s^{-1}$ by averaging the available data from the literature ^{141,169}, whereas $Y_{s/ph,m}^c$ was set to $0.10 \text{ mol}_s \text{ mol}_{ph}^{-1}$ according to theory stoichiometry ([Chapter 1 - section 1.7](#)). On the other hand, $q_{s,m}^c$ was experimentally derived from P-I curves (data not shown).

To estimate the m_s parameter as function of biomass concentration the following formula has been used:

$$m_s(C_x) = A \cdot (1 + e^{(D+C \cdot B \cdot C_x)})^{-1/B} \quad (4.9)$$

where C_x is the biomass concentration expressed in $\text{mol}_x \text{ m}^{-3}$, and A , B , C are the parameters fitted on experimental data, which will be named hereafter $\vec{\omega}$ for the sake of simplicity. The m_s parameters may be influenced by cultivation conditions such as T and pH, but in this work optimal conditions were carefully kept constant for *G. sulphuraria*, and therefore the m_s has been described as only function of biomass concentration. It follows: $m_s(T, pH, C_x, \vec{\omega}) = m_s(C_x, \vec{\omega})$

Moreover, to reduce the number of fitting parameters and therefore increase the fitting confidence, the position of the m_s function profile described by Eq. 4.9 was fixed by using the constrain:

$$\lim_{C_x \rightarrow 0} m_s(C_x, \vec{\omega}) = 0 \quad (4.10)$$

However, given the properties of sigmoid functions for numerical treatability, the limit Eq. 4.10 is set to 10^{-9} .

By solving this constrain, it results in:

$$D = \ln \left(\left(\frac{A}{10^{-9}} \right)^B - 1 \right) \quad (4.11)$$

Therefore, the number of fitting parameters moved from 4 to 3.

The working environment was administered and controlled using the Anaconda distribution of Python (version 3.9.7), and all data management tasks, including the manipulation of data structures, were performed using the Pandas library (version 2.0.3).

All the above equations were discretised by subdividing the photobioreactors into 10^4 layers along the light path (z). Being the fitting performed on batch cultivations, to predict the biomass accumulation over time it has been used:

$$\frac{dC_x}{dt} = \mu \cdot C_x \quad (4.12)$$

This differential equation was solved with the *Explicit Runge-Kutta method of order 5(4) (RK45)* solver implemented in the *solve_ivp* function from the SciPy library (version 1.11.1), using default parameters. Output parameters were evaluated at the same sampling points of the batch experiments. The $\vec{\omega}$ parameters were fitted using the *minimize* function implemented in the SciPy library, using default settings. Boundaries were imposed to the $\vec{\omega}$ parameters during the fitting, namely A ($10^{-8}, 10^{-4}$), B ($10^{-7}, 5$), C ($-10, 10$), to provide a physical meaning, given the commonly reported ranges for the m_s parameter, and to enhance the efficiency of the training process.

The minimized loss function was defined as the absolute value of the sum of residual errors between the experimental and predicted values for all trials in the training set across all time points.

$$Loss\ Function = \sum_{i=1}^N |y_{pred,i} - y_{exp,i}| \quad (4.13)$$

The m_s parameter has been fitted by using both the experimental absorption cross section ($a_{x,\lambda}$) and the derived averaged-absorption cross section (a_x), taken approximatively every 24h. The $a_x/a_{x,\lambda}$ values between the sampling times have been therefore retrieved using the linear interpolation implemented in the scipy library.

4.2.4.2 Model evaluation

The model accuracy has been evaluated using the following metrics: Mean Absolute Percentage Error (MAPE), Mean Absolute Error (MAE), and R^2 .

$$MAPE = \frac{100\%}{N} \cdot \sum_{i=1}^N \frac{|y_{pred,i} - y_{exp,i}|}{y_{exp,i}} \quad (4.14)$$

$$MAE = \sum_{i=1}^N \frac{|y_{pred,i} - y_{exp,i}|}{N} \quad (4.15)$$

$$R^2 = 1 - \frac{\sum_{i=1}^N (y_{exp,i} - y_{pred,i})^2}{\sum_{i=1}^N (y_{exp,i} - \bar{y}_{exp,i})^2} \quad (4.16)$$

where N is the number of experimental points within a batch experiment, y_{pred} is the model C_x predictions, and y_{exp} is the C_x experimental data. Additionally, the Mean Error and Skewness metrics were also retrieved using the respective functions implemented in the NumPy and SciPy libraries.

For both training and test datasets, the metrics have been used for the biomass concentration C_x at the given time t of the experiments. The results shown hereafter are evaluated on the test dataset.

4.2.5 a_x effect on model performances

Once the $m_s(C_x)$ function has been identified using experimental a_x values, an investigation over the a_x effect on the specific microalgal growth rate was executed at different constant averaged light intensities (62.5, 125, 250, 500 $\mu\text{mol}_{ph} \text{m}^{-2} \text{s}^{-1}$). Namely, the a_x value was changed in the range between 1.4 and 2.2 $\text{m}^2 \text{mol}_x^{-1}$, since the expected steady value was experimentally observed to be in this range. The a_x value was therefore homogeneously changed within this range with a linearly spaced discretization with 100 values.

4.3 Results and Discussion

4.3.1 *G. sulphuraria* elemental composition

From the CHNS analysis, the elemental composition of *G. sulphuraria* grown photoautotrophically under the conditions described in this work is as follows: C = 47.81%, N = 10.41%, H = 6.91%, S = 1.67%, O = 31.2%, and P = 2%. These data have been translated into 1 mol_x compound represented by the formula $CH_{1.7}O_{0.019}N_{0.007}P_{0.0006}$. By calculating the corresponding grams of each element, it has been determined that the molecular weight of *G. sulphuraria* is 25 g mol^{-1} . It is worth mentioning all model calculations were performed using as units $C_x = mol_x m^{-3}$ and $I_{ph} = mol_{ph} m^{-2} s^{-1}$, but for the sake of readiness all graphs in this chapter are presented with the more intuitive units of $C_x = g_x L^{-1}$ and $I_{ph} = \mu mol_{ph} m^{-2} s^{-1}$ according to the here-described molecular weight of *G. sulphuraria*.

4.3.2 Model training

Figure 27 shows the predictions on three representative batches of the test set, namely the best (A), the worst (B), and the on-average (C) obtained predictions, following the training with which the fitting parameters have been identified and based both on experimental a_x and $a_{x,\lambda}$ values.

In evaluating the model's performance across the reported predictions, Table 4 reports a range of error metrics that provide insight into its accuracy and bias. The best prediction scenario (A) obtained by using the experimental averaged absorption cross section (a_x), with a mean error of 1.364 and skewness of 0.286, indicates a nearly Gaussian error distribution centred around zero, demonstrating minimal bias and high accuracy. In contrast, the worst obtained prediction (B), with a mean error of 4.009 and skewness of -0.457, suggests a slight overestimation tendency, but still within an acceptable error margin given the dataset's range.

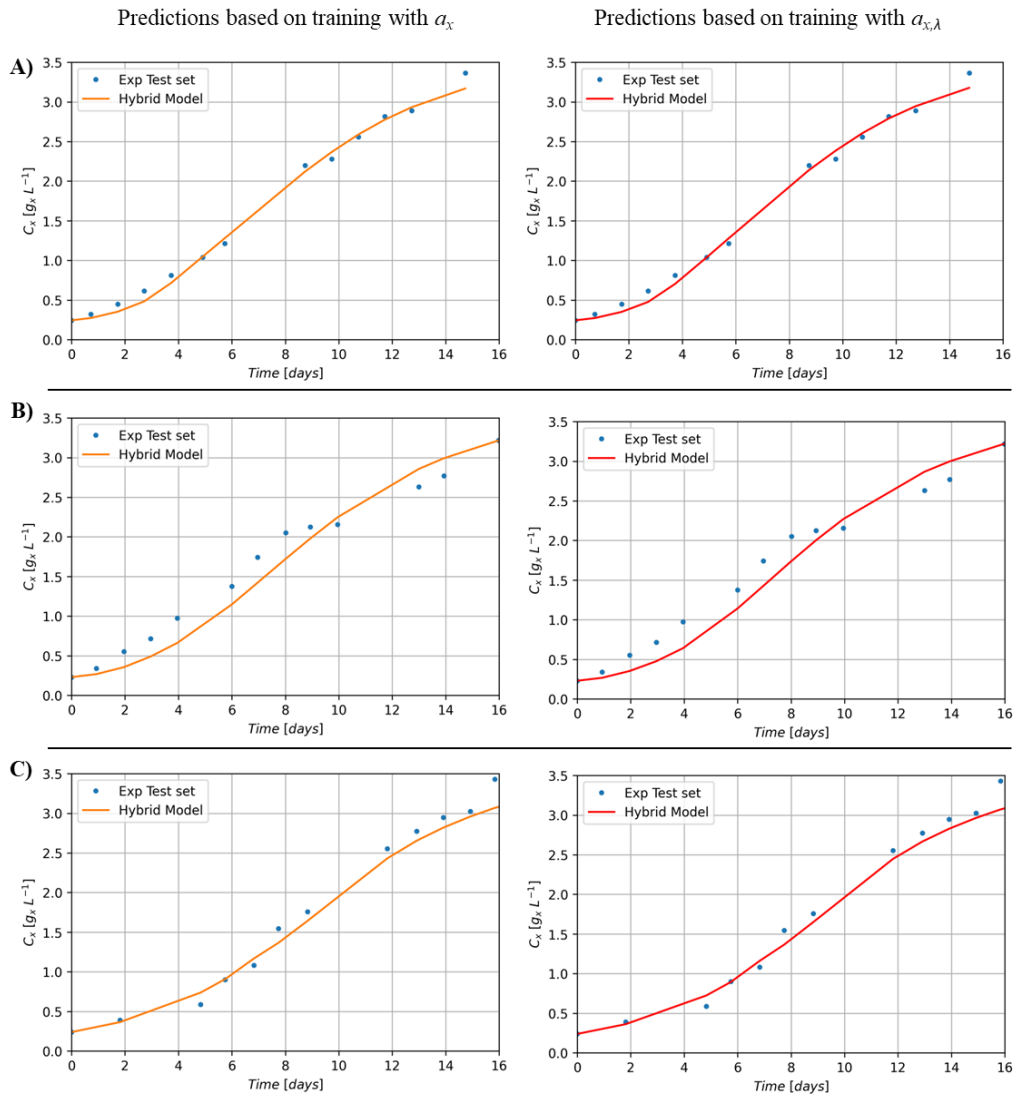


Figure 27: Hybrid model performances of three representative batches of the test set. A. The best obtained prediction. B. The worst obtained prediction. C. The on-average obtained prediction. Graphs on the left side (orange lines) represent the predictions using the average absorption cross section a_x data, whereas the graphs on the right side (red lines) the predictions using the wavelength specific absorption cross section $a_{x,\lambda}$ data.

Table 4: Predictions and errors' metrics of the reported representative batches of the test set.

	MAPE (%)	MAE	R²	Mean Error	Skewness
A - a_x	7.121	2.823	0.993	1.364	0.286
A - $a_{x,\lambda}$	7.313	2.869	0.993	1.199	0.196
B - a_x	15.377	7.317	0.950	4.009	-0.457
B - $a_{x,\lambda}$	15.712	7.417	0.948	3.858	-0.448
C - a_x	7.694	6.115	0.962	2.973	1.630
C - $a_{x,\lambda}$	7.433	6.061	0.962	3.030	1.603

On the other hand, the on-average prediction scenario (C) displays a mean error of 3.030 and skewness of 1.603. These metrics indicates a slightly higher level of inaccuracy and a positive skew, suggesting a tendency for the model to underestimate actual values. The error distribution in this scenario deviates somewhat from the ideal Gaussian shape, presenting a positive skewness that would need for a higher model refinement to address the prevalent underestimations. Nevertheless, the model may still provide valuable insights and predictions, especially if the errors are consistent and can be accounted for or corrected in subsequent analyses and/or hyperparameter tuning.

By using the wavelength-specific absorption cross section ($a_{x,\lambda}$) instead of a_x , all the metrics show no notable improvements for all the cases.

For both the best (A) and on-average (C) predictions, the models consistently return MAPE values below 10%, indicating that the model error is around 10%, extending to a maximum of 20 % for the worst prediction (B), which anyway stands as an isolated result within the dataset. Whereas, looking to the MAE, it ranges from approximately 2.14 % in the case A to 5.54% and 4.63% in the B and C, respectively, calculated as percentages of the maximum value of the curve, which is $132 \text{ mol}_x \text{ m}^{-3}$ (3.3 g L^{-1}). Being the MAPE higher than the MAE indicates that most relevant errors occur predominantly at the beginning of cultivation, possibly during the lag phase, which can be influenced by technical aspects such as inoculum density, inoculum pigmentation, and light conditions at inoculation time.

Lastly, the R² values are close to 1 in all cases, indicating that the models perform better than the average points, accurately following the growth trend regardless of the absorption cross section data used.

Comparing the graphs with and without wavelength resolution (Fig. 27), for all the cases A, B and C, reveals that the results are substantially similar with no real significant differences observed. Moreover, by examining the distribution of metrics across the overall train and test sets (Fig. 28), it becomes evident that, although it is theoretically appropriate to use wavelength-specific resolution, the use of such data under our conditions does not lead to any significant improvement. Therefore, the use of the averaged a_x data is suggested, since it results in a more streamlined code and shorter computation time compared to the wavelength resolution, at least under the cultivation, and most importantly light spectrum, conditions utilized in this PhD work for *G. sulphuraria*. If the goal is merely parameter identification (*i.e.*, obtaining the numerical values), then the use of $a_{x,\lambda}$ values might be acceptable for the train dataset. For the reasons detailed in this paragraph, all subsequent analyses in this work have been conducted using the experimental a_x values.

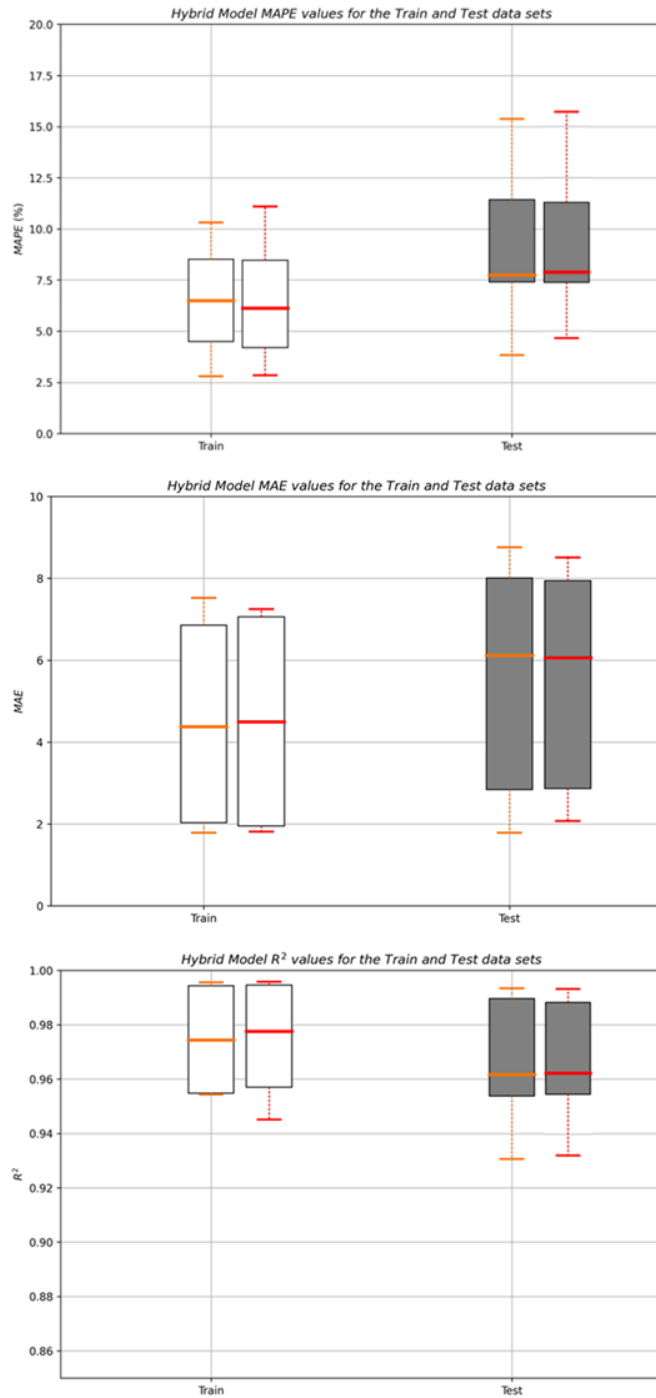


Figure 28: MAPE, MAE and R² box plots of the hybrid model performances for the train (white) and test (grey) data sets. The rectangles with orange whiskers and medians represents the metrics' distribution of the predictions using the average absorption cross section a_x data, whereas the rectangles with red whiskers and medians the predictions using the wavelength specific absorption cross section $a_{x,\lambda}$ data.

4.3.3 Model analysis

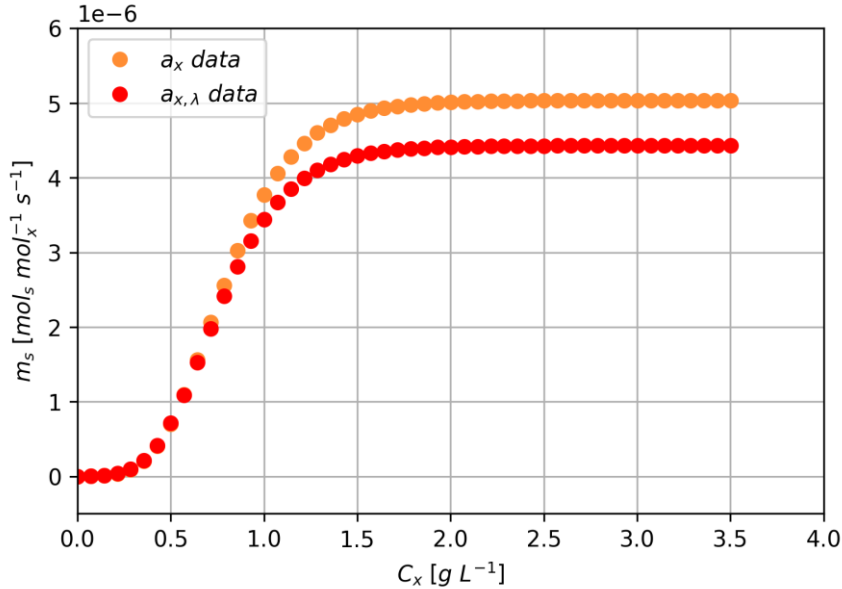


Figure 29: The trend of the specific sugar consumption rate for maintenance (m_s) as function of the biomass concentration C_x as described by Eq. 4.9, with the $\vec{\omega}$ parameters fitted on the experimental data of the train data set using the a_x (orange dots) and $a_{x,\lambda}$ (red dots) data.

From Figure 29 it can be noted as the $m_s(C_x)$ function has the typical S shape, ranging between a minimum and a maximum value, which represents the physics of the system (m_s must be a bounded function) since a primary metabolic rate must necessarily be a non-zero finite number. Moreover, the predicted m_s values, obtained with both the the experimental a_x and $a_{x,\lambda}$ data, fall within the range reported in the literature for several microorganisms ($1 \cdot 10^{-6}$ - $6 \cdot 10^{-6} mol_s mol_x^{-1} s^{-1}$). The predicted $m_{s,m}$ values for *G. sulphuraria*, grown in the conditions detailed in this work, varies from $5.04 \cdot 10^{-6}$ to $4.43 \cdot 10^{-6} mol_s mol_x^{-1} s^{-1}$, by using the experimental a_x and $a_{x,\lambda}$ data, respectively.

One of the main advantages of having a hybrid model adapting the m_s values as function of process conditions, is the more accurate prediction of the microalgae growth behaviour. Indeed, Figure 30 shows the cases where m_s is set to both the minimum and maximum constant values proposed in the literature^{52,170}, and it is possible to assess how the existence range of the model is very wide, with the width increasing with time due to propagation of the ODE (Ordinal Differential Equations). The hybrid model described in this work is represented by the orange

curve, which perfectly fall within the range of the possible growth curves. Moreover, it can be noted that the hybrid model, executed by taking as input the same initial biomass concentration ($C_x(t=0)$, hereafter named $C_x(0)$), averaged incident light intensity ($I_{ph}(z=0)$, hereafter named $I_{ph}(0)$) and an average a_x value of an experimental test, describes more accurately the experimental points compared to the same predictions executed with the constant boundary m_s values.

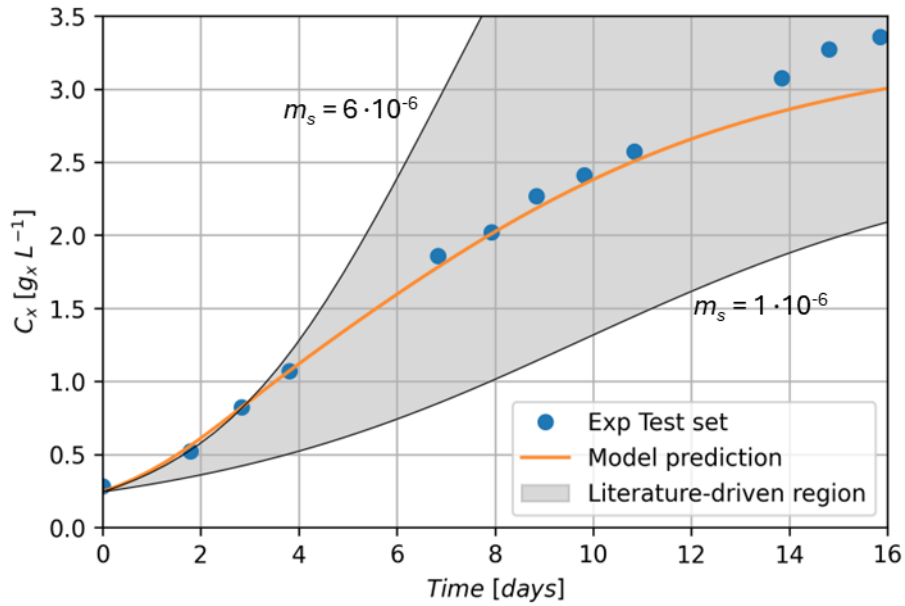


Figure 30: Comparison of the model prediction implementing the adaptive m_s (orange line) and the predictions assuming a constant m_s value within the literature-reported range (grey region). The blue dots show an experimental batch cultivation of the test data set. All the predictions were made using the following parameters values: $I_{ph}(0) = 125 \mu\text{mol}_{ph} \text{m}^{-2} \text{s}^{-1}$, $C_x(0) = 9.46 \text{mol}_x \text{m}^{-3}$ (matching the experimental starting biomass concentration = $0.244 \text{g}_x \text{L}^{-1}$); $a_x = 1.8 \text{m}^2 \text{mol}_x^{-1}$ (averaged value obtained with the growth conditions utilized in this study).

Figure 31 depicts a heat map reporting the hybrid model predictions of the specific growth rate μ as function of the averaged incident light intensity and biomass concentration, given an averaged a_x value of $1.8 \text{m}^2 \text{mol}_x^{-1}$. This a_x value was chosen since it represents the average value observed experimentally over the batch cultivations performed. As can be noted, the predicted μ are in line with the physics describing the photoautotrophic growth, where: i) at a given light intensity, the increasing biomass concentration translates to a decrease of μ due to light limitation along the culture path; ii) at a given biomass concentration, the μ increases along with the supplied light intensity, because of the higher photons' availability. The

isoline curves in the graph delineate the input variable combination such that the output value (μ) is constant. Therefore, they can be employed as an operative tool for a preliminary determination of the growth conditions to be compatible to the downstream process over a continuous cultivation, to maximize the overall process efficiency. Lastly, the isolines can explain the effect of a control variable over the other one to reach always the same growth rate, and therefore can be used as a powerful tool also to implement automated controllers.

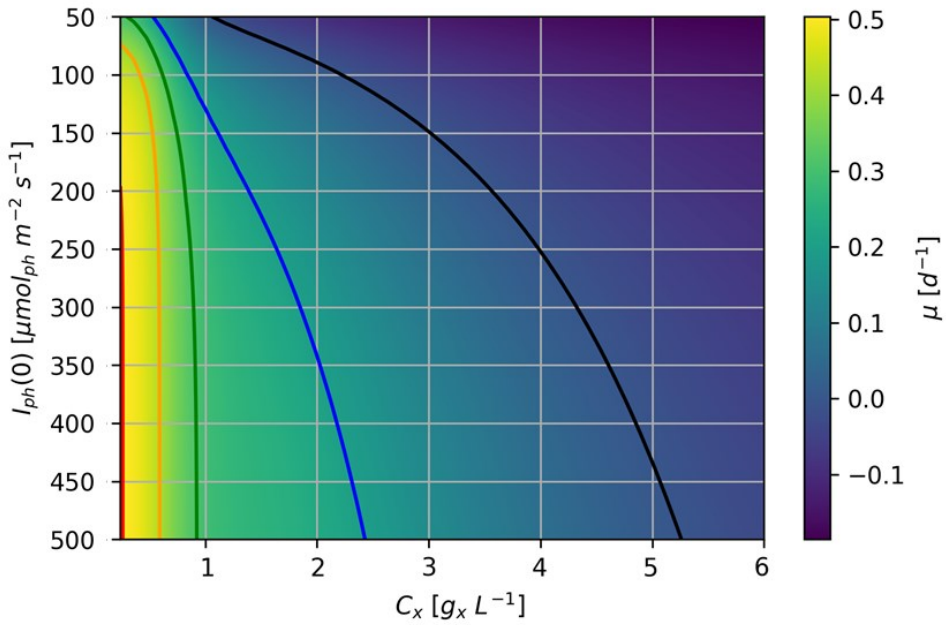


Figure 31: Contour plot of the hybrid model derived growth rate (μ) as a function of biomass concentration (C_x) and the incident light intensity ($I_{ph}(0)$). The isolines indicate the specific C_x and $I_{ph}(0)$ values for which the μ is constant: $\mu = 0 \text{ d}^{-1}$ (black); $\mu = 0.2 \text{ d}^{-1}$ (blue); $\mu = 0.3 \text{ d}^{-1}$ (green); $\mu = 0.4 \text{ d}^{-1}$ (orange); $\mu = 0.5 \text{ d}^{-1}$ (red).

Lastly, the effect of a_x on the microalgal growth has been evaluated using a probabilistic approach. Its value has been changed following a uniform distribution between the minimum and maximum a_x values identified in the experimental campaign. The effect on the μ of this stochastic change was evaluated, together with the biomass concentration C_x and averaged incident light intensity $I_{ph}(0)$ (Fig. 32). In this figure, the more shaded are the points at a given biomass concentration and light intensity conditions, the more is the a_x effect on μ . On the other hand, the more gathered are the points, the less is the effect of a_x on μ . As can be noted, at low biomass concentrations increasing the $I_{ph}(0)$ value returns a less relevant effect of a_x on μ . Indeed, at low light intensities (blue) the a_x values at low C_x are more

scattered, whereas at the highest $I_{ph}(0)$ (red), they result in a more gathered configuration. Notably, a counter configuration can be identified at high C_x . Furthermore, according to the hybrid model predictions, a C_x range can be identified, between 1.5 and 2.5 $g L^{-1}$, where the variation of a_x has a neglectable effect on μ , regardless the light intensity supplied. This plot is auxiliar to the heat map reported in Fig. 31 because the latter was obtained assuming a constant averaged a_x . However, looking at Fig. 32, is possible to detect areas where the variation of a_x is significant to the growth rate and others where it is less important, suggesting that experimental knowledge of a_x is necessary at least in the initial phase of experimentation with a new microalgae strain in order to finely tune the growth conditions and improve the overall process efficiency.

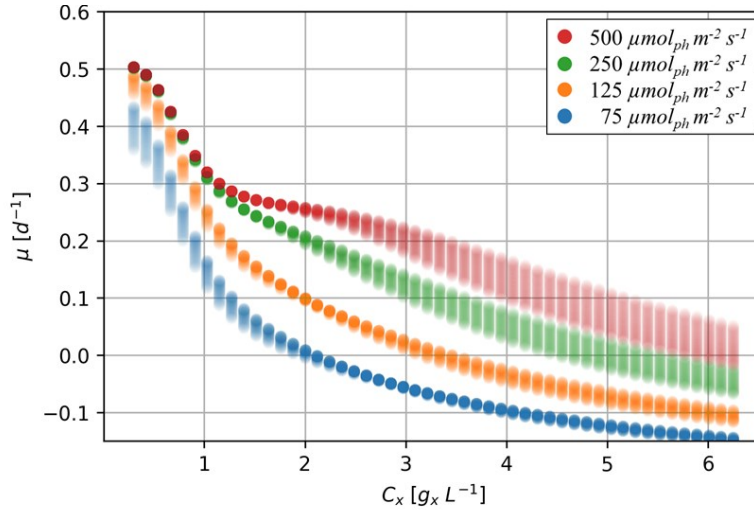


Figure 32: Hybrid model derived growth rate (μ) sensitivity with a_x and averaged incident light intensity ($I_{ph}(0)$), assuming a_x stochastic behavior with uniform probability in the range [min = 1.4, max = 2.2 $m^2 mol_x^{-1}$]. For each light intensity, it is possible to identify C_x ranges where the value of a_x significantly influences the μ and others where the growth rate is substantially independent of a_x .

4.4 Conclusion

In conclusion, the hybrid model developed in this study demonstrates a significant improvement in predicting microalgae growth by dynamically adjusting the m_s values based on varying process conditions. This adaptive approach outperforms models utilizing constant m_s values, particularly in accurately describing experimental growth data. Additionally, the utilization of probabilistic analyses provides deeper insights into the interplay between light intensity, biomass concentration, and growth rate. These tools not only facilitate the preliminary determination of optimal growth conditions but also support the implementation of automated control systems. It is worth mentioning that the model code has been written in Python, ensuring greater transferability to industrial settings, and its fast-paced pipeline allows for efficient integration into model predictive controllers. In the authors' opinion, the proposed methodology significantly streamlines the resolution of the equations, presenting a more operationally efficient and straightforward approach, particularly from an engineering perspective. This method not only simplifies the computational process but also obviates the necessity for experimental exploration of the associated parameters in the absence of relevant data within the existing literature. The robustness and practical applicability of this hybrid model mark a significant advancement in optimizing microalgal cultivation processes.

Chapter 5

Towards sustainable water management for *Galdieria sulphuraria* cultivation

5.1 Introduction

Microalgae cultivation has become increasingly popular due to its potential for commercial applications across various industries ². As a result of CO₂ fixation, microalgae are capable of accumulating significant amounts of carbohydrates, proteins, lipids, and other valuable compounds, such as pigments and vitamins, making them a promising energy feedstock with versatile applications in the production of dietary supplements, cosmetics, food, animal feed, and biofuels ^{77–80}. However, one of the main challenges associated with microalgae cultivation is, among others, the large amount of water required for biomass production, as well as the continuous replacement of freshwater in photobioreactors to support the biological functions and growth of algae. The high cost of freshwater, in terms of energy and environment impact, and its limited availability, especially in water-stressed regions, have contributed to impair the growth of the microalgae industry ^{171,172}. Optimizing the harvesting process and investigating the feasibility of reusing water would lead to the reduction of environmental and management costs associated with microalgae cultivation ¹⁷³, moving towards a circular economy approach.

The polyextremophile red microalga *Galdieria sulphuraria* has gained extensive attention for its ability to survive in harsh conditions, such as low pH (as low as 0.2 for some strains) ¹⁴¹, high temperatures (up to 57°C), and high osmotic pressure ¹⁴². *G. sulphuraria* has been found to be a rich source of proteins, insoluble dietary fibers, and antioxidants ^{143,163}. It also contains a high proportion of essential sulphur amino acids compared to other sources, *e.g.*, *Chlorella*, *Spirulina*, and soybean protein ¹⁶⁴. Its blue-green colour is attributed to the presence of blue

phycobiliproteins C-phycoyanin (*C-PC*) and allophycocyanin, as well as chlorophyll *a*. Furthermore, the C-phycoyanin extracted from *G. sulphuraria* is more stable at low pH and high temperatures than that extracted from *Arthrospira platensis*, the latter representing the nearly exclusive *C-PC* production platform today. These characteristics position *G. sulphuraria* as a promising candidate for large-scale production as a food and feed source.

Since *G. sulphuraria* cultivation medium requires low pH conditions, sulphuric acid is commonly added to the cultivation medium, leading to highly acidic wastewaters, which exceed typical wastewater discharge standards, including Italian limits for industrial wastewater discharge after biomass harvesting (Annex 5, Third Section, Legislative Decree n. 152/2006, ¹⁷⁴). Therefore, the aim of the work described in this chapter was to assess two separation techniques, namely, centrifugation and membrane microfiltration, in their ability to extract water to be reused as new cultivation medium. In particular, different fractions of reused water were investigated, as well as their effects for one or multiple cycles of *G. sulphuraria* cultivation at pilot scale. Additionally, the potential *C-PC* content achievable within the employed photobioreactor (PBR), under control conditions (distilled water plus salts) as well as when algae are grown in reused water, is discussed. Finally, a comparison between centrifugation and membrane filtration is provided in terms of achievable extraction and energy input at different scales, with the goal to provide a preliminary guide toward the choice of the most suitable water reuse technique. The present work has been conducted in collaboration with the Environmental Surface Engineering laboratory for Water (DIATI – Polytechnic of Turin) lead by Prof. Tiraferri.

5.2 Materials and Methods

5.2.1 Microalgae growth and cultivation conditions

Galdieria sulphuraria strain 074W was kindly donated by Prof. Antonino Pollio (University of Naples, Italy). All the experiments were conducted within the PBR in batch mode and axenic conditions under constant illumination with the specific light spectrum as described in Chapter 3 ¹⁷⁵. The PBR was inoculated with: (i) Allen medium (control conditions) acidified at pH 2 with sulphuric acid ¹⁴⁰, or with (ii) recovered water added with distilled water in a ratio 1:3 (with nutrients reintegration), or with (iii) reused water only (with N and P reintegration), as well as with microalgae cells, reaching a total volume of 45 L. The initial biomass dry weight was about 0.25 g L⁻¹ for all the tests. Microalgae growth was gravimetrically

quantified as dry biomass concentration as reported in [section 2.2.3](#)¹²⁷. The biomass volumetric productivity P_x ($g L^{-1} d^{-1}$) was then calculated as Eq. 2.1.

5.2.2 Microalgae harvesting methods

Cells reaching the stationary phase were collected and centrifuged using a CLARA-20 centrifuge (Alfa Laval, Sweden) model operated with a starting flow of $100 L h^{-1}$ up to $150 L h^{-1}$, and a counter pressure of about 1.8-1.9 *bar*. On the other hand, for what concern the harvesting through the microfiltration process, a standard system configuration was employed. A TiO_2 ceramic membrane (TAMI industries, France) with $0.14 \mu m$ pore-size was selected as it proved its effectiveness among other microfiltration and ultrafiltration membranes when concentrating algal biomass in the same concentration range^{176,177}. The tubular membrane length was 1170 *mm* in length and its active filtration area was $0.21 m^2$. Two different filtration protocols were performed: the first one consisted in semi-batch operations whereby, at fixed recovery rate values, the permeated water was recirculated into the feed tank until steady-state conditions were reached and then the loop was opened to separately collect the permeate water. This protocol was repeated at the following five recovery values: 0, 25%, 50%, 75%, and 90%. In the second protocol, the permeated water was collected separately and continuously, thus operating in an open loop configuration: in this case, the feed solution was continuously concentrated until the highest possible recovery rate was reached. For both testing protocols, the same operating conditions were used: the cross flow velocity was $2.5 m s^{-1}$, corresponding to a feed flow rate of $1.9 m^3 h^{-1}$, while the average trans-membrane pressure was 1.6 *bar*. To restore the initial characteristics of the membranes for each new reuse cycle, extensive membrane cleaning was performed after the filtration process in two steps: i) quick flushing with tap water to rinse the filtration unit and remove the remaining algal matter, followed by 30 *min* of continuous operation with deionized water, and ii) at least 4 *h* of operation at a nominal TMP, using a solution containing $NaClO$ ($6 mL L^{-1}$) and citric acid ($1.5 g L^{-1}$). The aim of such extensive cleaning was solely to restore the initial membrane conditions to allow a fair comparison between the consecutive filtration processes, and it is not to be intended as a blueprint for actual operation practices.

The concentrated biomass (approximately 2 *L*), either from centrifugation or microfiltration, was frozen at $-85^\circ C$ and subsequently lyophilized (ScanVac CoolSafe Touch 55-4 Freeze Dryer, LaboGene, Denmark) to facilitate further extractions. As mentioned above, the reused water was either mixed with distilled water (with nutrient reintegration) in a 1:3 ratio (25% reused water and 75%

distilled water) or used as is (~73-98%, with nutrients reintegration) to prepare the cultivation medium for subsequent algae growth.

5.2.3 C-PC extraction and quantification

The C-phycoyanin (*C-PC*) from *G. sulphuraria* was quantitatively extracted by bead beating (Mixer Mill MM 400, Retsch, Germany) approximately 1 g of lyophilized biomass. Lyophilized cells were resuspended in 100 mM Na-phosphate buffer at pH 7 and exposed to 3×5 min beating cycles at a frequency of 30 Hz with 5 min breaks on ice between each cycle. Cell debris was removed through centrifugation at 16,000 rpm for 10 min and the supernatant was collected in fresh tubes. This extract is called crude extract. The *C-PC* contents were calculated measuring the absorbance at 620 and 652 nm and converting the measured absorbance to concentration using the Kursar and Alberte equation¹⁷⁸.

5.2.4 Macro- and micro-nutrients monitoring

Macronutrients and micronutrients were quantified after water extraction and, if needed, re-integrated in the solution to achieve the same concentrations of the ideal Allen medium. Nitrogen (N) and phosphorous (P) were quantified spectrophotometrically (Onda UV-31 Scan spectrophotometer, China) using standard reagent kits for highly sensitive photometric measurements (NANOCOLOR® test kit, Macherey-Nagel, Germany). All the other metals, namely, magnesium (Mg), potassium (K), manganese (Mn), sodium (Na), iron (Fe), cobalt (Co), and molybdenum (Mo), were quantified with inductively coupled plasma metal analysis (OPTIMA 2000 ICP optical emission spectrometer, PerkinElmer, U.S.A.).

5.3 Results and Discussion

5.3.1 Microalgae cultivation in partially reused water (25%)

In recent years, *Galdieria sulphuraria* has emerged as a promising biotechnological platform for large-scale cultivation and production of a high-nutritional value biomass, for nutraceutical purposes, as well as to produce high-value molecules, such as the blue pigment phycocyanin. However, being an extremophilic species, it requires cultivation at high temperatures, and most importantly, in an appropriately acidified culture medium. The acidification of the medium is commonly achieved using sulphuric acid, which results at the end of the

process and after biomass harvesting, in a strongly acidic wastewater outside the legal limits for industrial wastewater release without a proper wastewater treatment. Moreover, since the use of a large amount of freshwater is among the main costs associated with large-scale algae cultivation, the possibility of reusing water and nutrients for multiple cultivation cycles would significantly reduce costs. In this study, a 25% water reuse factor was first performed to assess the preliminary feasibility of the process. In fact, the reused water was always characterized by a yellowish colour due to the likely presence of algae organic matter (AOM), which, without appropriate dilution, might lead to a strong attenuation of light, interfere with algae growth, and/or contribute to biofouling within the PBR¹⁷⁹. After an initial batch cultivation with standard (control) medium, 3 consecutive cycles of harvesting and re-inoculation using the reused water mixed with distilled water in a ratio of 1:3 were carried out. This experiment was conducted identically with the reused water obtained from centrifugation and from membrane filtration. Note that the harvesting processes were conducted starting from a biomass concentration of 1 g L^{-1} achieved after algae growth in each of the cycles. For these tests, only N and P concentrations were quantified in the reused water and re-integrated in each of the cycles to achieve the starting, ideal concentrations, equal to those of the standard solution. All the other salts were added to the final working volume without prior measurement, according to the medium recipe. Despite the dilution, the pH remained between 3-3.5 for all the cultivation cycles, therefore no pH adjustment was performed.

Fig. 33 reports the *G. sulphuraria* growth data in control conditions and in each consecutive cycle of growth in partially reused water derived from the centrifugation (Fig 33A.) and membrane microfiltration (Fig 33B.) processes. After 16 days of cultivation, the biomass concentration reached $3.26 \text{ g L}^{-1} \pm 0.15$ in control conditions, with an average biomass productivity (P_x) during the exponential phase of $0.21 \text{ g L}^{-1} \text{ d}^{-1} \pm 0.06$. Growth in partially reused water showed negligible differences with respect to the control condition for both the downstream processes employed, reaching the same final concentrations at the end of the cultivation period. Indeed, the average P_x during the exponential phase was 0.22 ± 0.10 , 0.20 ± 0.07 , and $0.20 \pm 0.05 \text{ g L}^{-1} \text{ d}^{-1}$, for the three cycles with centrifugation, respectively, and 0.22 ± 0.02 , 0.24 ± 0.04 , and $0.21 \pm 0.03 \text{ g L}^{-1} \text{ d}^{-1}$, respectively, for the membrane microfiltration process.

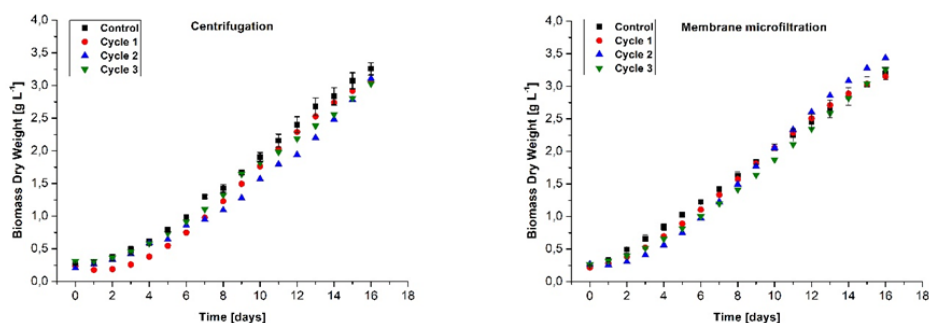


Figure 33: Biomass concentration measured over time during cultivation. A. Cycles of partially reused water from centrifugation. B. Cycles of partially reused water from membrane microfiltration. Black squares: control (n =3). Red circles: 1st cycle at 25% water reuse. Blue triangles: 2nd cycle at 25% water reuse. Green triangles: 3rd cycle at 25% water reuse.

The results reported in Figure 34 delve into the performance of the microfiltration process. The water flux across the membrane decreased from the first to the third reuse cycle, with a trend suggesting a possible fouling problem. As expected, increasing the water recovery, in turn leading to increased biomass concentration in the feed solution, translated into a decrease of water flux and increase in fouling. The release of AOM consequent to algal cell break and the possible accumulation of AOM from one cycle to the next translated into more important clogging of the membrane pores, likely due to low MW compounds. These results suggest that multiple water reuse cycles can be potentially achieved by membrane filtration, but with a reduction of membrane productivity, hence harvesting efficiency. That being said, the observed flux was always above $40 L m^{-2} h^{-1}$, even in the third reuse cycle and at 90 % recovery rate ($10\times$ algae concentration factor in the feed suspension, equivalent to a cell concentration of $10 g L^{-1}$). The flux results suggest that it should be possible to maintain a minimum flux larger than $\sim 30-40 L m^{-2} h^{-1}$ and an average flux larger than $40-50 L m^{-2} h^{-1}$ for several reuse cycles and working at algae cell concentrations between roughly 1 and $10 g L^{-1}$. In the last filtration cycle shown in Fig. 34, the dissolved organic carbon (DOC) concentration in the permeate water was measured at each recovery step: 0, 25%, 50%, 75%, and 90% recovery values corresponded to concentration of DOC of respectively 52.6 ppm, 54.7 ppm, 55.3 ppm, 58.8 ppm, and 60.3 ppm. These results highlighted a trend: DOC concentration increased in the permeate as feed concentration increased, consistent with theoretical expectations assuming a constant membrane rejection, which results in increased permeation with increased concentration in the feed suspension.

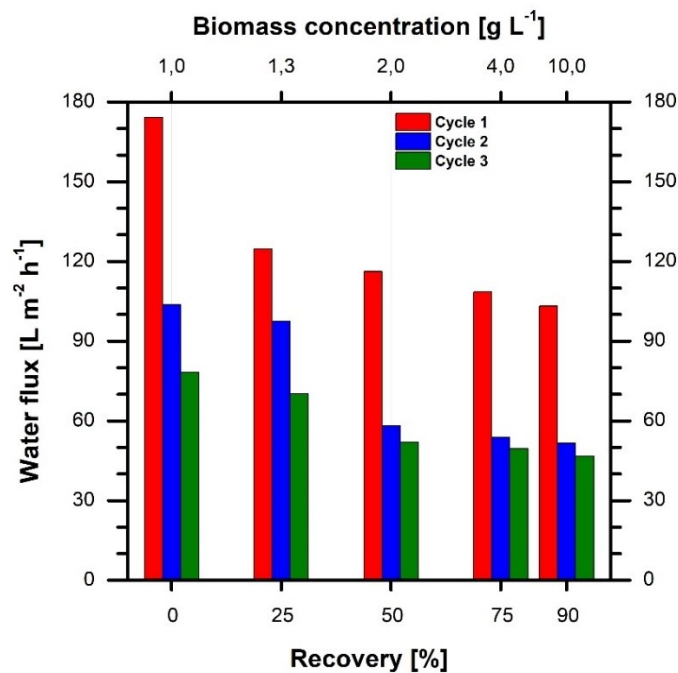


Figure 34: Water flux across the microfiltration membrane as a function of water recovery values. The reported water flux values were measured upon reaching flux stabilization for each recovery value. These results refer to a starting biomass concentration of 1 g L^{-1} and an applied pressure of 1.6 bar .

5.3.2 Microalgae cultivation with highest recovered water volume

Appraised the potential of partial water reuse, both in terms of algae cultivation in reused media and harvesting process, full water reuse was assessed while simultaneously stressing the harvesting system by using suspensions with initial biomass concentration equal to 4 g L^{-1} . In particular, the centrifugation allowed retrieving 99 % of the total water volume (44.55 L out of 45 L of water were recovered), of which 44 L were used as new culture medium ($\sim 98 \%$) upon mixing with 1 L ($\sim 2 \%$) of fresh microalgae inoculum. Therefore, a concentration factor of ~ 100 was achieved by centrifugation, reaching algae concentrations of roughly 400 g L^{-1} in the final concentrated slurry. Whereas, by concentrating the microalgae substrate with membranes, the achieved water recovery was approximately 80.5% (32.2 L out of 40 L of water were recovered), corresponding to a 5.1 concentration factor and a final algae concentration of approximately 20.5 g L^{-1} in the concentrate stream. Fresh microalgae inoculum and additional distilled water were then added

to reach the final working volume of 45 L, corresponding thus to an overall 71.5 % of reused water. For these tests, only one cycle of water reuse was assessed on independent trials for the two downstream processes. All the nutrients were quantified in the reused water (Table 5). Since the concentration of all the monitored elements did not decrease significantly, indicating an excess of nutrients in the ideal medium, only N and P were re-integrated into the reused water. As expected, the pH values of reused water in the final working volume were found to be 2 and 2.6, for the centrifugation and membrane microfiltration experiments respectively, and therefore no pH adjustment was required.

Table 5: Concentration of metals and ions in the culture medium in different solutions, before and after cultivation, before and after water recovery with centrifugation or microfiltration.

<i>Metal/ion</i>	<i>Concentration in the Allen medium (control) [mg L⁻¹]</i>	<i>Concentration after biomass cultivation prior to centrifugation [mg L⁻¹]</i>	<i>Concentration in the recovered water from centrifugation [mg L⁻¹]</i>	<i>Concentration of the feed solution prior to membrane microfiltration [mg L⁻¹]</i>	<i>Concentration in the permeated water from membrane microfiltration [mg L⁻¹]</i>
Mo	2.38 ± 0.02	1.13 ± 0.03	1.126 ± 0.026	2.20 ± 0.07	1.60 ± 0.05
Co	0.028 ± 0.00	0.03 ± 0.00	0.029 ± 0.00	0.06 ± 0.02	0.05 ± 0.03
Fe	2.223 ± 0.021	1.90 ± 0.03	1.904 ± 0.027	1.46 ± 0.04	1.36 ± 0.05
Mn	2.285 ± 0.011	2.02 ± 0.05	2.019 ± 0.047	2.11 ± 0.03	2.01 ± 0.02
Mg	39.35 ± 0.042	33.02 ± 0.69	33.02 ± 0.684	26.96 ± 0.74	12.91 ± 0.66
Na	10.73 ± 0.24	11.09 ± 0.28	11.088 ± 0.282	11.30 ± 0.34	11.44 ± 0.22
K	101.2 ± 0.707	67.79 ± 1.39	67.793 ± 1.392	58.87 ± 2.11	56.15 ± 2.98
NH₄⁺	470.7 ± 2.22	47.55 ± 0.84	47.55 ± 0.84	n.d.	n.d.
PO₄³⁻	250.10 ± 1.46	147.18 ± 4.25	147.18 ± 4.25	143.55 ± 5.41	142.88 ± 4.44

The results displayed in Figure 35 indicate that *G. sulphuraria* growth was not affected by the use of the maximum recoverable water from both the downstream processes. The averaged P_x during exponential growth was 0.25 ± 0.08 , 0.24 ± 0.06 , and $0.24 \pm 0.10 \text{ g L}^{-1} \text{ d}^{-1}$ for the control batches and the growth on reused water

from the centrifugation and membrane microfiltration processes, respectively. Despite the strong yellowish colour of the reused water, indicating the likely presence of a substantial amount of *AOM*, no differences in growth rate or in terms of biofouling were observed in one cycle of water reuse. Further experiments are necessary to address the feasibility of reusing water for more consecutive cycles and a proper integration of nutrients according to the microalgae needs and according to economic criteria. Note that no substantial loss of micronutrients was observed upon centrifugation or microfiltration, with measured metal and ion concentrations close to the values determined in the cultivation suspension upon biomass growth in the ideal Allen medium (Table 5). Only a certain loss of magnesium was observed in the microfiltration test, which may be simply related to experimental error and would require further investigation.

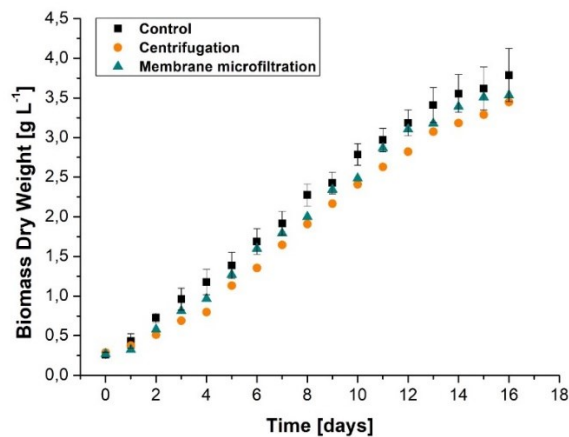


Figure 35: Biomass concentration over time during cultivation in reused water. Black squares: control (n =3). Orange circles: growth in 98 % reused water from centrifugation (n = 2). Green triangles: growth in 71.5 % reused water from microfiltration.

Results in Figure 36 delve into the microfiltration behaviour when separating water from a feed stream containing an initial biomass concentration of 4 g L^{-1} in open-loop configuration, *i.e.*, permeate stream continuously recovered externally to the feed loop until the maximum recovery achievable in the employed system was reached (80.5%). The water fluxes were consistent with those reported in Fig. 34. In particular, the system started with a flux roughly equal to $72 \text{ L m}^{-2} \text{ h}^{-1}$, which is within the range of flux values observed at the recovery rate of 75 % in the experiments starting with a biomass concentration equal to 1 g L^{-1} . The flux decreased to a value of $55 \text{ L m}^{-2} \text{ h}^{-1}$ at the end of the filtration, once again

suggesting the feasibility of the microfiltration system to concentrate biomass and extract freshwater, at least in terms of system productivity. Dissolved Organic Carbon (DOC) and Total Nitrogen (TN) were measured in the initial feed stream, in the concentrate stream, in a permeating water sample collected in the beginning of the experiment, and in the total permeated volume. DOC results were 216 ppm, 411 ppm, 140 ppm, and 169 ppm respectively, while TN concentrations were respectively equal to 24.4 ppm, 44.0 ppm, 18.0 ppm, and 22.6 ppm. The DOC and TN rejections provided by the membrane were thus roughly 35 % and 20 %, respectively. However, the system rejections, calculated from the concentrations in the total permeated volume with respect to the initial feed, were approximately 20 % and 5 %, respectively. Note that the membrane pores are much larger than any dissolved substance and that filtration operated by the algae cake is likely responsible for most of the observed rejection of DOC and TN. Differences in the absolute DOC concentration values between the partial and full water reuse scenarios were due to the different initial algal concentration (1 g L^{-1} and 4 g L^{-1} , respectively).

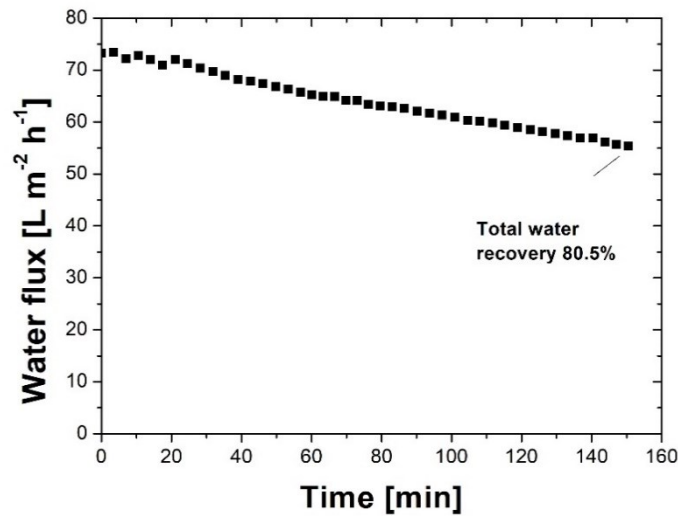


Figure 36: Measured water flux (y-axis) during microfiltration reported against time(x-axis). These results refer to a starting biomass concentration of 4 g L^{-1} and an applied pressure of 1.6 bar.

5.3.3 Analysis of water reuse energy consumption

In this study, two different downstream processes for biomass separation were employed, namely, microfiltration and centrifugation. Among the wide spectrum of possible concentrating techniques, these processes represent the most adopted solutions for biomass separation from the liquid phase as of today. A direct energy comparison between the two techniques is far from straightforward, due to the fundamental difference in their separation mechanism, the variety of conditions, and the multiple parameters affecting energy expenses. However, two variables that are hypothesized to influence the energy performance of concentration systems and, therefore, the choice of the most suitable harvesting option, are the following. (i) Cultivation volumes or flow rates: energy expenses are related to the size of the system, often in a non-linear and complex way. (ii) Starting and final biomass concentrations and the relative concentration factor. This discussion aims at reviewing energy expense figures related to the two separation techniques in the light of the two variables just highlighted, placing energy figures into context, and drawing conclusions that may guide a rational choice of the most suitable process aimed at biomass harvesting and freshwater extraction.

(i) To understand the effect of system size, the discussion starts with reviewing the energy expenses measured with the lab-scale units utilized in this work, then those that are estimated for efficient large-scale systems, and will finally provide ranges associated pilot-scale units and reported in the literature. The membrane separation system and the centrifuge deployed in this research were laboratory-scale units, far from being optimized in terms of energy consumption. The measured, specific electrical energy consumption (SEEC) of the membrane separation was approximately 25 kW m^{-3} (energy needed for each m^3 of extracted freshwater), calculated by simply considering that the power absorbed by the pump was $\sim 0.3 \text{ kW}$ and that the system recovered 32.2 L of water out of 40 L of diluted biomass in 150 min of operation. On the other hand, the separation operated with the centrifuge was associated with a SEEC of approximately 14 kW m^{-3} , calculated considering that the power absorption of the system was $\sim 2.2 \text{ kW}$ and that it separated 39.2 L of water out of 40 L of diluted biomass in 15 min . It is worth highlighting again that these figures do not represent those that would be necessary in a real scale plant, but they serve the goal of highlighting the importance of system scale and modularity features.

On the other end of the spectrum compared to lab-scale systems, large-scale plants aim at reducing irreversibility issues, thus using energy in an efficient way and

approximating as much as possible the energy of separation that can be estimated from first principles. For example, the SEEC expected for an efficient membrane-based separation driven by applied pressure can be calculated directly starting from the Bernoulli's principle as follows:

$$SEEC_m = \frac{Q_{feed} \cdot (\Delta P + \Delta P_{loss})}{Q_{perm} \cdot \eta \cdot 36} \quad (5.1)$$

where Q_f is the feed flow rate ($L h^{-1}$), Q_{perm} is the permeate flow rate ($L h^{-1}$), η is the efficiency of the pump (-), assumed equal to 0.5 to give a conservative estimation, ΔP is the applied pressure (*bar*), and ΔP_{loss} represents the pressure losses (*bar*) that can be conservatively assumed equal to 0.1 *bar* for each meter of membrane module. The ratio between Q_{perm} and Q_f represents the single pass recovery rate of the system that proved to be easily above 80 % for the application of this study. The resulting theoretical SEEC value for the extraction of freshwater, assuming the same conditions of the laboratory unit utilized in this study ($\Delta P = 1.6$ *bar*, $\Delta P_{loss} = 0.12$ *bar* relative to a 1178 *mm* long module), is $0.12 kW m^{-3}$. This number is roughly 200 times smaller than the energy value needed with the lab-scale unit utilized in this study and is not far from what would be expected in a large-scale microfiltration system. Indeed, optimized large-scale microfiltration plants for surface water treatment consistently show energy consumptions around $0.3 kW m^{-3}$ at very high recovery rates (> 95 %).

SEEC values reported in the literature for pilot-scale membrane units operated for biomass harvesting range from $0.97 kW m^{-3}$ to $2.5 kW m^{-3}$, one order of magnitude higher than the value estimated from Bernoulli's principle. The former value refers to the optimized conditions of a system managing 2000 *L* microalgae suspension and a volume concentration factor equal to 200¹⁸⁰, while the latter value refers to an experimental measurement of the harvesting of 200 *L* microalgal suspension reaching a volume concentration factor of 39.2¹⁸¹. Considering instead available data of commercial centrifuge systems, the Clara 750 and Clara 20 from Alfa Laval may be taken as representative examples. They are associated to SEEC values for centrifugation of $0.9 kW m^{-3}$ and $4.4 kW m^{-3}$, respectively. Note that these two centrifuge units represent the limits of systems commercialized by Alfa Laval: Clara 750 operates at a maximum flow rate of $50 m^3 h^{-1}$, while Clara 20 at $0.5 m^3 h^{-1}$. These SEEC values are in the same order of magnitude as those that can be estimated from equations based on centrifugal forces, applied by some authors to estimate the energy expense of centrifugation starting from first principles^{182,183}.

The numbers reported above highlight an important trend. The energy needs of membrane-based microfiltration may span as much as four orders of magnitude (0.1 to 100 $kW m^{-3}$) as a function of system size. This ample range is due to the intrinsic modularity of membrane systems: the number of modules in parallel and in series, the overall membrane active area, bypass and recirculating streams, and the possible presence of pressure recovery devices, strongly impact the energy consumption. In this respect, systems with larger membrane active area are characteristically more energetically efficient than smaller ones. Energy values for centrifugation systems fall instead within two orders of magnitude only (1 to 10 $kW m^{-3}$), implying that system size plays some role, but substantially less so compared to membrane units. As hypothesized above, the scale of the system is in fact an important guiding principle to select the best downstream harvesting technique.

(ii) When considering the other variable hypothesized above, *i.e.*, achievable biomass concentrations and concentration factor, note that microfiltration has limitations when it comes to the concentration of microalgae that can be attained in the retentate stream, due to issues associated with fouling and/or cake build-up when highly concentrated suspensions are filtered. It is unlikely that a well-operated microfiltration system could reach concentrations substantially larger than $\sim 50 g L^{-1}$ for the harvested biomass, possibly reaching values in the order of $100 g L^{-1}$ in the best-case scenario. On the other hand, well-operated centrifugation systems have been shown to achieve considerably larger biomass concentration in the harvested product, at least $150 g L^{-1}$ (as also observed in this study), but possibly up to an order of magnitude of $1000 g L^{-1}$. Biomass contents above $100 g L^{-1}$ are required by most of the applications seeking to utilize the harvested biomass for beneficial purposes. Therefore, the majority of biomass harvesting plants would likely require a single or a final concentration step that would guarantee such target biomass concentration values.

Given the assessments discussed above, some rational guiding principles may be formulated. For biomass plants producing $< \sim 10 m^3$ of algae suspension daily, a harvesting system comprising a single centrifugation step would possibly be the best option, since it would allow achieving a target concentration factor while requiring reasonable energy inputs. As a reference scenario for understanding the actual size of real microalgal biomass harvesting systems, the cultivation of Astaxanthin-producing microalgae is analysed. Although its cultivation represents a relatively small market, with an average estimated produced volume of $18,500 kg yr^{-1}$, five players produce around 72 % of the overall final product. Among these companies, BGG, Algatech, and Algalif currently produce, respectively, ~ 4000 ,

2500, and 2500 $kg\ yr^{-1}$ of final product using PBR cultivation technology, while Cyanotech currently produces $\sim 1500\ kg\ yr^{-1}$ with open ponds. Assuming typical microalgal concentrations in pond cultivation from 0.5 to 0.8 $g\ L^{-1}$ and concentrations from PBR in the range 1-2 $g\ L^{-1}$, the volumes of diluted microalgal biomass being treated every year range from 1250 to 4000 m^3 , corresponding to daily flow rates from 3.4 to 11 m^3 . As the biomass cultivation plant increases in size above this range, membrane systems become increasingly competitive in terms of energy consumption, to the point where it would make sense to pre-concentrate the biomass suspension using a membrane-based separation and then achieve the final harvesting target with a centrifugation process. Such a two-step process would combine the intrinsic ability of medium to large-scale membrane systems to effectively extract large volumes of freshwater with relatively low specific energy demands, and the intrinsic ability of centrifuge systems to concentrate the biomass to high values while managing a suspension of smaller volume.

As a disclaimer to the guiding principles just highlighted, the most suitable separation train should be evaluated in each case, also to ensure the continuity between the bioreactor and the harvesting process when the extracted freshwater is to be reused in part or in full. Also, note that the microalgal strain may have an impact on the efficacy of the harvested techniques: different species have shown distinct results when concentrated using the same technique, seen differences in their shape, size, and chemical composition.

5.3.4 Biomass quality and environmental benefits of water reuse

This study indicates the technical feasibility of reusing cultivation water for *Galdieria sulphuraria* growth, potentially yielding significant resource savings and environmental impact reduction. Monitoring water quality throughout the cultivation process, both upstream and downstream, is crucial for effective water reuse and it allows precise interventions, such as nutrient reintegration. In particular, nitrogen (N) and phosphorus (P) re-integration may be optimized to meet primary metabolic needs while addressing economic and environmental sustainability criteria. In this study, phosphorus was consumed at a considerably lower rate compared to nitrogen. This phenomenon suggests a likely abundance of phosphorus in the standard cultivation medium, making reintroduction unnecessary, at least in the first or the first few water reuse cycles. Also, the results indicated that micronutrient consumption may be reduced by up to 77% across three water reuse cycles. Additionally, this research addresses the environmental challenge posed by the addition of sulphuric acid to obtain low pH conditions in the

cultivation medium. By eliminating the need to adjust the pH, the overall volume of acidic wastewater requiring treatment would be reduced, as well as the need for chemicals. This achievement would have broader implications for sustainable and environmentally friendly microalgal cultivation practices.

To ensure high biomass quality in successive cultivation cycles conducted in reused water, the final *C-PC* accumulation in *G. sulphuraria* achievable within the flat panel PBR was finally evaluated. At the end of the cultivation period, the *C-PC* accumulated was found to be the 10.80 ± 0.36 % *w/w* in the control conditions (Table 6). This value is between the highest ever reported for several *G. sulphuraria* strains grown with different trophic modes ^{164,165,184}. Nevertheless, it is worth mentioning that the *C-PC* accumulation at the end of a batch cultivation process is maximized, as cultures are dense, and light becomes the limiting factor. Continuous cultivation experiments should be performed to evaluate and maximize the *C-PC* volumetric and areal productivities, appropriately selecting the most appropriate conditions, namely, biomass concentration, dilution factor, and light intensity. As reported in Table 6, the final *C-PC* accumulation did not vary when reused water was used as partial cultivation medium for consecutive cycles, or at the maximum recoverable volume, regardless of the harvesting process used. This result implies no major stress factor associated to the strong yellowish colour of recovered water, nor the possible presence of *AOM*, over *C-PC* accumulation.

Table 6: *G. sulphuraria* *C-PC* accumulation as % weight/weight at the end of each cultivation cycle (n = 2).

Conditions	C-Phycocyanin [<i>w/w</i> %]
Control	10.80 ± 0.36
<i>Centrifugation steps</i>	
Cycle 1 25% water reuse	10.46 ± 0.28
Cycle 2 25% water reuse	10.12 ± 0.63
Cycle 3 25% water reuse	10.16 ± 0.84
Max water reuse (98%)	10.79 ± 0.46
<i>Membrane microfiltration steps</i>	
Cycle 1 25% water reuse	9.46 ± 0.48
Cycle 2 25% water reuse	10.71 ± 0.93
Cycle 3 25% water reuse	9.88 ± 0.66
Max water reuse (71.5%)	11.09 ± 0.76

5.4 Conclusion

The successful reuse of acidic wastewater in *Galdieria sulphuraria* cultivation was discussed in this chapter. Two harvesting techniques were evaluated and compared to concentrate biomass and extract water for reuse, namely, membrane microfiltration and centrifugation. Results showed that directly reusing 25% of water did not significantly affect the growth or the quality of *G. sulphuraria* in subsequent cultivation cycles. Moreover, reusing the maximum recoverable freshwater derived from both harvesting processes did not affect the *G. sulphuraria* growth nor the final *C-PC* accumulation, at least for one cycle of reuse. The assessment of more consecutive water reuse cycles operations is currently under investigation. Appropriate nutrient re-integration was necessary to achieve such goals. Directly reusing highly acidic (pH 2-3) wastewater and micronutrients in *G. sulphuraria* schemes may represent an important step forward in making microalgae cultivation more sustainable by reducing the amount of required freshwater and minimizing the release of acidic wastewater. The performed size and energy analyses suggests that centrifugation may be more appropriate for small to medium-size biomass cultivation applications, where are involved either small volumes of biomass or high algal cell concentrations in the final biomass product. A preliminary analysis suggests that centrifugation may be more suitable for small or medium-size biomass cultivation plants and/or to achieve high algal cell concentrations in the final biomass product. On the other hand, the adoption of microfiltration units, possibly as pre-treatment for a final concentration step, would allow reducing the overall energy consumption when large volumes of flow rate of biomass suspensions need to be harvested. The potential of this approach for further optimization and scale-up should be investigated in future studies, with the aim of achieving higher levels of water and metal/ions reuse, and ultimately, a more efficient and environmentally friendly process for large-scale microalgae cultivation.

Chapter 6

General conclusion and future perspectives

Overall, this PhD thesis makes substantial contributions to the field of microalgae cultivation by presenting an advanced PBR design with a detailed description of its fluid dynamics and enhanced artificial light management, along with the development of tools for process optimization and the investigation of sustainable water reuse and resource recovery. Three main topics have been sequentially developed and investigated in this thesis: i) Innovative photobioreactor design and optimized light supply management; ii) hybrid modelling for process optimization; and iii) sustainable practices: water and nutrient recycling. Each topic represents a significant contribution to advancing microalgae cultivation technologies, collectively contributing to the efficiency, sustainability, and scalability of microalgae production systems.

i) Central to this thesis is the introduction of a novel flat panel PBR prototype equipped with a centrifugal pump-assisted hydraulic circuit and a customizable LED lighting system. This design enhances mixing efficiency, improves CO₂ mass transfer, and enables precise control over light spectra and intensity, crucial for optimizing conditions for microalgae growth. The prototype's demonstrated performance with various microalgae species highlights its potential for achieving high biomass productivity and efficient CO₂ bio-fixation, signalling a significant step toward sustainable industrial-scale production. Additionally, a detailed CFD analysis has provided crucial insights into the hydrodynamics of the PBR system, guiding technical optimizations to enhance mixing patterns and optimize light distribution within the reactor. Future research could explore enhancements such as internal baffles or deflectors to further improve mass transfer efficiency and overall system performance. Conducting continuous growth experiments will further provide valuable data on the long-term stability and efficiency of the PBR system under industrial conditions, as well as testing more powerful tailored light supply systems could further enhance photosynthetic efficiency and biomass productivity.

ii) A key contribution of this thesis is the development of a hybrid modelling approach for predicting microalgae growth under light limiting conditions. This approach dynamically adjusts model parameters, enhancing accuracy in predicting growth rates and biomass yields compared to traditional static models. By incorporating probabilistic analyses, the model provides deeper insights into the complex interactions between light intensity, biomass concentration, and growth rates. These capabilities might not only optimize cultivation conditions but also support the implementation of automated control systems for real-time adjustments. The model's robustness and adaptability make it a valuable tool for optimizing operational parameters and scaling up microalgae production systems. Future applications will include its use with green microalgae and/or cyanobacteria to assess the model's versatility and effectiveness across different microalgae species, potentially broadening its applicability. Additionally, the development of a graphical interface would facilitate its ease of use and integration into IoT processes, enabling real-time monitoring and optimization, and leading to more efficient and responsive cultivation processes.

iii) Efforts to recycle acidic wastewater and recover nutrients in the cultivation of *Galdieria sulphuraria* underscore the thesis's commitment to sustainability. Evaluation of membrane microfiltration and centrifugation techniques for biomass harvesting and water recovery shows promise in reducing freshwater consumption and minimizing environmental impact in large-scale microalgae cultivation. Further optimization and scale-up of these recycling processes hold potential for achieving higher efficiency and sustainability goals. Additionally, continuous cultivations where the volume of water to be replenished can be effectively sourced from biomass centrifugation and/or microfiltration will be pursued. Conducting continuous tests will provide insight into the feasibility of maintaining a closed-loop water recycling system over extended periods, further reducing freshwater usage. The ability to replenish water from the biomass harvesting process can ensure a steady supply of recycled water, enhancing the sustainability of the cultivation process. This approach aligns with circular economy principles and could set new standards for water management in industrial microalgae production.

Looking forward, this PhD work lays the groundwork for future improvements in large-scale microalgae cultivation, where key trends to investigate might be summarized in the following macro topics:

- **Advancements in PBR Technology:** Continued innovation in PBR design, focusing on improving energy efficiency, scalability, and integration of smart technologies for real-time monitoring and control.
- **Integration of Artificial Intelligence (AI):** Use of AI algorithms to optimize PBR operations, enhance predictive modelling capabilities, and enable autonomous decision-making to maximize productivity and resource efficiency.
- **Circular Economy Practices:** Expansion of closed-loop systems for water, nutrient, and metal recycling to minimize waste and environmental impact, supporting sustainable microalgae cultivation on a larger scale.
- **Commercialization and Scaling:** Validation of research findings in pilot and demonstration projects to assess economic feasibility and facilitate commercial adoption of advanced microalgae cultivation technologies.

In conclusion, this thesis makes significant contributions to advancing microalgae cultivation technologies. By addressing key challenges and exploring innovative solutions, the research sets the stage for continued progress toward sustainable and efficient production of microalgal biomass for various industrial and environmental applications. Future research efforts should leverage these advancements to achieve greater sustainability, scalability, and economic viability in microalgae cultivation.

References

- (1) Chisti, Y. Biodiesel from Microalgae. *Biotechnol Adv* **2007**, *25* (3), 294–306. <https://doi.org/10.1016/j.biotechadv.2007.02.001>.
- (2) Spolaore, P.; Joannis-Cassan, C.; Duran, E.; Isambert, A. Commercial Applications of Microalgae. *J Biosci Bioeng* **2006**, *101* (2), 87–96. <https://doi.org/10.1263/jbb.101.87>.
- (3) Chen, C. Y.; Yeh, K. L.; Aisyah, R.; Lee, D. J.; Chang, J. S. Cultivation, Photobioreactor Design and Harvesting of Microalgae for Biodiesel Production: A Critical Review. *Bioresour Technol* **2011**, *102* (1), 71–81. <https://doi.org/10.1016/j.biortech.2010.06.159>.
- (4) Becker, E. W. Chemical Composition. In *Microalgae: Biotechnology and Microbiology*; Cambridge University Press, 1993; pp 177–195.
- (5) Guiry, M. D. How Many Species of Algae Are There? *Journal of Phycology*. October 2012, pp 1057–1063. <https://doi.org/10.1111/j.1529-8817.2012.01222.x>.
- (6) Ambati, R. R.; Gogisetty, D.; Aswathanarayana, R. G.; Ravi, S.; Bikkina, P. N.; Bo, L.; Yuepeng, S. Industrial Potential of Carotenoid Pigments from Microalgae: Current Trends and Future Prospects. *Critical Reviews in Food Science and Nutrition*. Taylor and Francis Inc. July 4, 2019, pp 1880–1902. <https://doi.org/10.1080/10408398.2018.1432561>.
- (7) Acién, F. G.; Molina, E.; Reis, A.; Torzillo, G.; Zittelli, G. C.; Sepúlveda, C.; Masojídek, J. *Photobioreactors for the Production of Microalgae*; 2017. <https://doi.org/10.1016/B978-0-08-101023-5.00001-7>.
- (8) Posten, C. Design Principles of Photo-Bioreactors for Cultivation of Microalgae. *Eng Life Sci* **2009**, *9* (3), 165–177. <https://doi.org/10.1002/elsc.200900003>.
- (9) Acién, F. G.; Fernández, J. M.; Magán, J. J.; Molina, E. Production Cost of a Real Microalgae Production Plant and Strategies to Reduce It. *Biotechnol Adv* **2012**, *30* (6), 1344–1353. <https://doi.org/10.1016/j.biotechadv.2012.02.005>.

- (10) Norsker, N. H.; Barbosa, M. J.; Vermuë, M. H.; Wijffels, R. H. Microalgal Production - A Close Look at the Economics. *Biotechnol Adv* **2011**, *29* (1), 24–27. <https://doi.org/10.1016/j.biotechadv.2010.08.005>.
- (11) Tredici, M. R.; Zittelli, G. C. *Efficiency of Sunlight Utilization: Tubular Versus Flat Photobioreactors*; 1998; Vol. 57.
- (12) Schulze, P. S. C.; Barreira, L. A.; Pereira, H. G. C.; Perales, J. A.; Varela, J. C. S. Light Emitting Diodes (LEDs) Applied to Microalgal Production. *Trends in Biotechnology*. Elsevier Ltd 2014, pp 422–430. <https://doi.org/10.1016/j.tibtech.2014.06.001>.
- (13) Radzun, K. A.; Wolf, J.; Jakob, G.; Zhang, E.; Stephens, E.; Ross, I.; Hankamer, B. Automated Nutrient Screening System Enables High-Throughput Optimisation of Microalgae Production Conditions. *Biotechnol Biofuels* **2015**, *8* (1). <https://doi.org/10.1186/s13068-015-0238-7>.
- (14) Blanken, W.; Cuaresma, M.; Wijffels, R. H.; Janssen, M. Cultivation of Microalgae on Artificial Light Comes at a Cost. *Algal Res* **2013**, *2* (4), 333–340. <https://doi.org/10.1016/j.algal.2013.09.004>.
- (15) Cuaresma, M.; Janssen, M.; Vilchez, C.; Wijffels, R. H. Productivity of *Chlorella Sorokiniana* in a Short Light-Path (SLP) Panel Photobioreactor under High Irradiance. *Biotechnol Bioeng* **2009**, *104* (2), 352–359. <https://doi.org/10.1002/bit.22394>.
- (16) Oldenhof, H.; Zachleder, V.; Van Den Ende, H. Blue- and Red-Light Regulation of the Cell Cycle in *Chlamydomonas Reinhardtii* (Chlorophyta). *Eur J Phycol* **2006**, *41* (3), 313–320. <https://doi.org/10.1080/09670260600699920>.
- (17) Acién Fernández, F. G.; Fernández Sevilla, J. M.; Sánchez Pérez, J. A.; Molina Grima, E.; Chisti, Y. *Airlift-Driven External-Loop Tubular Photobioreactors for Outdoor Production of Microalgae: Assessment of Design and Performance*; 2001; Vol. 56.
- (18) Tredici, M. R.; Bassi, N.; Prussi, M.; Biondi, N.; Rodolfi, L.; Chini Zittelli, G.; Sampietro, G. Energy Balance of Algal Biomass Production in a 1-Ha “Green Wall Panel” Plant: How to Produce Algal Biomass in a Closed Reactor Achieving a High Net Energy Ratio. *Appl Energy* **2015**, *154*, 1103–1111. <https://doi.org/10.1016/j.apenergy.2015.01.086>.
- (19) Fernández-Sevilla, J. M.; Molina-Grima, E. ; Garcia-Camacho, F.; Acién Fernández, F. G.; Sánchez-Pérez, J. A. Photolimitation and Photoinhibition

as Factors Determining Optimal Dilution Rate to Produce Eicosapentaenoic Acid from Cultures of the Microalga *Isochrysis Galbana*. **1998**, 199–205.

- (20) Molina Grima, E.; Carnacho, F. G.; Sanchez Perez, J. A.; Fernandez Sevilla, J. M.; Acien Fernandez, F. G.; Contreras Gomez, A. *A Mathematical Model of Microalgal Growth in Light-Limited Chemostat Culture*; 1994; Vol. 61.
- (21) Sánchez, J. F.; Fernández-Sevilla, J. M.; Acién, F. G.; Cerón, M. C.; Pérez-Parra, J.; Molina-Grima, E. Biomass and Lutein Productivity of *Scenedesmus Almeriensis*: Influence of Irradiance, Dilution Rate and Temperature. *Appl Microbiol Biotechnol* **2008**, *79* (5), 719–729. <https://doi.org/10.1007/s00253-008-1494-2>.
- (22) Tredici, M. R. Photobiology of Microalgae Mass Cultures: Understanding the Tools for the Next Green Revolution. *Biofuels* **2010**, *1*, 143.
- (23) Andersen, R. A.; Berges, J. A.; Harrison, P. J.; Watanabe, M. m. Recipes for Freshwater and Seawater Media. In *Algae Culturing Techniques*; Andersen, R. A., Ed.; Elsevier: New York, 2005; pp 429–538.
- (24) Grobbelaar, J. U. *6 Algal Nutrition Mineral Nutrition*; 2004.
- (25) Costache, T. A.; Gabriel Acien Fernandez, F.; Morales, M. M.; Fernández-Sevilla, J. M.; Stamatin, I.; Molina, E. Comprehensive Model of Microalgae Photosynthesis Rate as a Function of Culture Conditions in Photobioreactors. *Appl Microbiol Biotechnol* **2013**, *97* (17), 7627–7637. <https://doi.org/10.1007/s00253-013-5035-2>.
- (26) Murata, N.; Takahashi, S.; Nishiyama, Y.; Allakhverdiev, S. I. Photoinhibition of Photosystem II under Environmental Stress. *Biochimica et Biophysica Acta - Bioenergetics*. June 2007, pp 414–421. <https://doi.org/10.1016/j.bbabi.2006.11.019>.
- (27) Collos, Y.; Harrison, P. J. Acclimation and Toxicity of High Ammonium Concentrations to Unicellular Algae. *Marine Pollution Bulletin*. 2014, pp 8–23. <https://doi.org/10.1016/j.marpolbul.2014.01.006>.
- (28) Ippoliti, D.; Gómez, C.; del Mar Morales-Amaral, M.; Pistocchi, R.; Fernández-Sevilla, J. M.; Acién, F. G. Modeling of Photosynthesis and Respiration Rate for *Isochrysis Galbana* (T-Iso) and Its Influence on the Production of This Strain. *Bioresour Technol* **2016**, *203*, 71–79. <https://doi.org/10.1016/j.biortech.2015.12.050>.

- (29) Bosma, R.; Van Zessen, E.; Reith, J. H.; Tramper, J.; Wijffels, R. H. Prediction of Volumetric Productivity of an Outdoor Photobioreactor. *Biotechnol Bioeng* **2007**, *97* (5), 1108–1120. <https://doi.org/10.1002/bit.21319>.
- (30) Huesemann, M. H.; Van Wagenen, J.; Miller, T.; Chavis, A.; Hobbs, S.; Crowe, B. A Screening Model to Predict Microalgae Biomass Growth in Photobioreactors and Raceway Ponds. *Biotechnol Bioeng* **2013**, *110* (6), 1583–1594. <https://doi.org/10.1002/bit.24814>.
- (31) Brindley, C.; García-Malea López, M. C.; Acien Fernández, F. G.; Fernández Sevilla, J. M.; García Sánchez, J. L.; Molina Grima, E. Influence of Power Supply in the Feasibility of *Phaeodactylum Tricornutum* Cultures. *Biotechnol Bioeng* **2004**, *87* (6), 723–733. <https://doi.org/10.1002/bit.20179>.
- (32) Brindley, C.; Jiménez-Ruiz, N.; Acien, F. G.; Fernández-Sevilla, J. M. Light Regime Optimization in Photobioreactors Using a Dynamic Photosynthesis Model. *Algal Res* **2016**, *16*, 399–408. <https://doi.org/10.1016/j.algal.2016.03.033>.
- (33) Masojídek, J.; Kopecký, J.; Giannelli, L.; Torzillo, G. Productivity Correlated to Photobiochemical Performance of *Chlorella* Mass Cultures Grown Outdoors in Thin-Layer Cascades. *J Ind Microbiol Biotechnol* **2011**, *38* (2), 307–317. <https://doi.org/10.1007/s10295-010-0774-x>.
- (34) Kumar, B. R.; Mathimani, T.; Sudhakar, M. P.; Rajendran, K.; Nizami, A. S.; Brindhadevi, K.; Pugazhendhi, A. A State of the Art Review on the Cultivation of Algae for Energy and Other Valuable Products: Application, Challenges, and Opportunities. *Renewable and Sustainable Energy Reviews*. Elsevier Ltd March 1, 2021. <https://doi.org/10.1016/j.rser.2020.110649>.
- (35) Deprá, M. C.; da Motta Pacheco, L. F. C.; Rossi, R.; Nunes, M.; Goldemberg, S.; Suzuki, S.; Menezes, M.; Jacob-Lopes, E. Hybrid Photobioreactors: The Success-to-Failure Experiences on Pilot Scale. In *3rd Generation Biofuels: Disruptive Technologies to Enable Commercial Production*; Elsevier, 2022; pp 1019–1035. <https://doi.org/10.1016/B978-0-323-90971-6.00014-0>.
- (36) Benemann, J. Microalgae for Biofuels and Animal Feeds. *Energies (Basel)* **2013**, *6* (11), 5869–5886. <https://doi.org/10.3390/en6115869>.
- (37) Chisti, Y. Raceways-Based Production of Algal Crude Oil. *Green* **2013**, *3* (3–4), 195–216. <https://doi.org/10.1515/green-2013-0018>.

- (38) Zerrouki, D.; Henni, A. Outdoor Microalgae Cultivation for Wastewater Treatment. In *Application of Microalgae in Wastewater Treatment*; Springer International Publishing, 2019; pp 81–99. https://doi.org/10.1007/978-3-030-13913-1_5.
- (39) Schenk, P. M.; Thomas-Hall, S. R.; Stephens, E.; Marx, U. C.; Mussgnug, J. H.; Posten, C.; Kruse, O.; Hankamer, B. Second Generation Biofuels: High-Efficiency Microalgae for Biodiesel Production. *Bioenergy Res* **2008**, *1* (1), 20–43. <https://doi.org/10.1007/s12155-008-9008-8>.
- (40) Torzillo, G.; Zittelli, G. C. Tubular Photobioreactors. In *Algal Biorefineries. In: Products and Refinery Design, vol. 2*; Prokop, A., Bajpai, R. K., Zappi, M. E., Eds.; Springer, Switzerland, 2015; pp 187–212. <https://doi.org/10.1007/978-3-319-20200-6>.
- (41) Zittelli, G. C.; Biondi, N.; Rodolfi, L.; Tredici, M. R. Photobioreactors for Mass Production of Microalgae BT - Absorption and Adsorption of Heavy Metals by Microalgae. *Handbook of Microalgal Culture: Applied Phycology and Biotechnology* **2013**, 225–266.
- (42) Camacho-Rubio, F.; Ación Fernández, F. G.; Sánchez Pérez, J. A.; García Camacho, F.; Molina Grima, E. Prediction of Dissolved Oxygen and Carbon Dioxide Concentration Profiles in Tubular Photobioreactors for Microalgal Culture. **1999**.
- (43) Wang, B.; Lan, C. Q.; Horsman, M. Closed Photobioreactors for Production of Microalgal Biomasses. *Biotechnology Advances*. July 2012, pp 904–912. <https://doi.org/10.1016/j.biotechadv.2012.01.019>.
- (44) Tredici, M. R.; Chini Zittelli, G.; Rodolfi, L. Photobioreactors. In *Encyclopedia of Industrial Biotechnology: Bioprocess, Bioseparation, and Cell Technology*; Flickinger, M. C., Ed.; Wiley, Hoboken, NJ, 2010; pp 3821–3838. <https://doi.org/10.1002/9780470054581.eib479>.
- (45) Carvalho, A. P.; Meireles, L. A.; Malcata, F. X. Microalgal Reactors: A Review of Enclosed System Designs and Performances. *Biotechnol Prog* **2006**, *22*, 1490–1506. <https://doi.org/10.1021/bp060065r>.
- (46) Tredici, M. R.; Carlozzi, P.; Chini Zittelli, G.; Materassi, R. A Vertical Alveolar Panel (VAP) for Outdoor Mass Cultivation of Microalgae and Cyanobacteria. *Bioresour Technol* **1991**, *38* (2–3), 153–159. [https://doi.org/10.1016/0960-8524\(91\)90147-C](https://doi.org/10.1016/0960-8524(91)90147-C).

- (47) Jacobi, A.; Ivanova, D.; Posten, C. *Photobioreactors: Hydrodynamics and Mass Transfer*; IFAC, 2010; Vol. 11. <https://doi.org/10.3182/20100707-3-BE-2012.0033>.
- (48) Li, J.; Stamato, M.; Velliou, E.; Jeffryes, C.; Agathos, S. N. Design and Characterization of a Scalable Airlift Flat Panel Photobioreactor for Microalgae Cultivation. *J Appl Phycol* **2015**, *27* (1), 75–86. <https://doi.org/10.1007/s10811-014-0335-1>.
- (49) Sierra, E.; Acién, F. G.; Fernández, J. M.; García, J. L.; González, C.; Molina, E. Characterization of a Flat Plate Photobioreactor for the Production of Microalgae. *Chemical Engineering Journal* **2008**, *138* (1–3), 136–147. <https://doi.org/10.1016/j.cej.2007.06.004>.
- (50) Bazaes, J.; Sepulveda, C.; Acién, F. G.; Morales, J.; Gonzales, L.; Rivas, M.; Riquelme, C. Outdoor Pilot-Scale Production of *Botryococcus Braunii* in Panel Reactors. *J Appl Phycol* **2012**, *24* (6), 1353–1360. <https://doi.org/10.1007/s10811-012-9787-3>.
- (51) Norsker, H.; Barbosa, M. J.; Vermuë, M. H.; Wijffels, R. H. On Energy Balance and Production Costs in Tubular and Flat Panel Photobioreactors. *TATuP - Zeitschrift für Technikfolgenabschätzung in Theorie und Praxis* **2012**, *21* (1), 54–62. <https://doi.org/10.14512/tatup.21.1.54>.
- (52) Blanken, W.; Postma, P. R.; de Winter, L.; Wijffels, R. H.; Janssen, M. Predicting Microalgae Growth. *Algal Res* **2016**, *14*, 28–38. <https://doi.org/10.1016/j.algal.2015.12.020>.
- (53) Quinn, J.; de Winter, L.; Bradley, T. Microalgae Bulk Growth Model with Application to Industrial Scale Systems. *Bioresour Technol* **2011**, *102* (8), 5083–5092. <https://doi.org/10.1016/j.biortech.2011.01.019>.
- (54) Klok, A. J.; Verbaanderd, J. A.; Lamers, P. P.; Martens, D. E.; Rinzema, A.; Wijffels, R. H. A Model for Customising Biomass Composition in Continuous Microalgae Production. *Bioresour Technol* **2013**, *146*, 89–100. <https://doi.org/10.1016/j.biortech.2013.07.039>.
- (55) Slegers, P. M.; Wijffels, R. H.; van Straten, G.; van Boxtel, A. J. B. Design Scenarios for Flat Panel Photobioreactors. *Appl Energy* **2011**, *88* (10), 3342–3353. <https://doi.org/10.1016/j.apenergy.2010.12.037>.
- (56) Geider, R. J.; MacIntyre, H. L.; Kana, T. M. Dynamic Model of Phytoplankton Growth and Acclimation: Responses of the Balanced Growth

Rate and the Chlorophyll a:Carbon Ratio to Light, Nutrient-Limitation and Temperature. *Mar Ecol Prog Ser* **1997**, *148*, 187–200.

- (57) Béchet, Q.; Chambonniè, P.; Shilton, A.; Guizard, G.; Guieysse, B. Algal Productivity Modeling: A Step toward Accurate Assessments of Full-Scale Algal Cultivation. *Biotechnol Bioeng* **2015**, *112*, 987–996. <https://doi.org/10.1002/bit.25517/abstract>.
- (58) Cornet, J.-F.; Dussap, C.-G. A Simple and Reliable Formula for Assessment of Maximum Volumetric Productivities in Photobioreactors. *American Institute of Chemical Engineers Biotechnol. Prog* **2009**, *25*, 424–435. <https://doi.org/10.1021/bp.138>.
- (59) Takache, H.; Pruvost, J.; Cornet, J. F. Kinetic Modeling of the Photosynthetic Growth of *Chlamydomonas Reinhardtii* in a Photobioreactor. *Biotechnol Prog* **2012**, *28* (3), 681–692. <https://doi.org/10.1002/btpr.1545>.
- (60) Lee, E.; Pruvost, J.; He, X.; Munipalli, R.; Pilon, L. Design Tool and Guidelines for Outdoor Photobioreactors. *Chem Eng Sci* **2014**, *106*, 18–29. <https://doi.org/10.1016/j.ces.2013.11.014>.
- (61) Kliphuis, A. M. J.; Janssen, M.; van den End, E. J.; Martens, D. E.; Wijffels, R. H. Light Respiration in *Chlorella Sorokiniana*. *J Appl Phycol* **2011**, *23* (6), 935–947. <https://doi.org/10.1007/s10811-010-9614-7>.
- (62) Geider, R. J.; Osborne, B. A. Respiration and Microalgal Growth: A Review of the Quantitative Relationship between Dark Respiration and Growth. *New Phytologist* **1989**, *112* (3), 327–341. <https://doi.org/10.1111/j.1469-8137.1989.tb00321.x>.
- (63) Pirt, S. J. The Maintenance Energy of Bacteria in Growing Cultures 225. *Proceedings of the Royal Society B: Biological Sciences* **1965**.
- (64) Shi, X.-M.; Chen, F.; Yuan, J.-P.; Chen, H. Heterotrophic Production of Lutein by Selected *Chlorella* Strains. *J Appl Phycol* **1997**, *9*, 445–450.
- (65) Chen, F.; Johns, M. R. Effect of C/N Ratio and Aeration on the Fatty Acid Composition of Heterotrophic *Chlorella Sorokiniana*. *J Appl Phycol* **1991**, *3*, 203–209.
- (66) Li, T.; Zheng, Y.; Yu, L.; Chen, S. Mixotrophic Cultivation of a *Chlorella Sorokiniana* Strain for Enhanced Biomass and Lipid Production. *Biomass Bioenergy* **2014**, *66*, 204–213. <https://doi.org/10.1016/j.biombioe.2014.04.010>.

- (67) Lee, Y.-K.; Ding, S.-Y.; Hoe, C.-H.; Low, C.-S. Mixotrophic Growth of *Chlorella Sorokiniana* in Outdoor Enclosed Photobioreactor. *J Appl Phycol* **1996**, *8*, 163.
- (68) Jassby, A. D.; Platt, T. Mathematical Formulation of the Relationship between Photosynthesis and Light for Phytoplankton. *Limnol Oceanogr* **1976**, *21* (4), 540–547. <https://doi.org/10.4319/lo.1976.21.4.0540>.
- (69) Chalker, B. E. Modelling Light Saturation Curves for Photosynthesis: An Exponential Function. *J. theor. Biol* **1980**, *84*, 205–215. [https://doi.org/10.1016/S0022-5193\(80\)80004-X](https://doi.org/10.1016/S0022-5193(80)80004-X).
- (70) Blunden, J.; Boyer, T. State of the Climate in 2020. *Bulletin of the American Meteorological Society*. American Meteorological Society August 1, 2021, pp 1–481. <https://doi.org/10.1175/2021BAMSSStateoftheClimate.1>.
- (71) Brown, L. M.; Zeiler, K. G. Aquatic Biomass and Carbon Dioxide Trapping. *Energy Convers Manag* **1993**, *34* (9–11), 1005–1013. [https://doi.org/10.1016/0196-8904\(93\)90048-F](https://doi.org/10.1016/0196-8904(93)90048-F).
- (72) Carlsson, A. S.; van Beilen, J. B.; Möller, R.; Clayton, D. *Micro- and Macro-Algae: Utility for Industrial Applications*; Outputs from the EPOBIO Project. CPL Press, Berks., 2007.
- (73) Rosenberg, J. N.; Mathias, A.; Korth, K.; Betenbaugh, M. J.; Oyler, G. A. Microalgal Biomass Production and Carbon Dioxide Sequestration from an Integrated Ethanol Biorefinery in Iowa: A Technical Appraisal and Economic Feasibility Evaluation. *Biomass Bioenergy* **2011**, *35* (9), 3865–3876. <https://doi.org/10.1016/j.biombioe.2011.05.014>.
- (74) Goli, A.; Shamiri, A.; Talaiekhosani, A.; Eshtiaghi, N.; Aghamohammadi, N.; Aroua, M. K. An Overview of Biological Processes and Their Potential for CO₂ Capture. *Journal of Environmental Management*. Academic Press December 1, 2016, pp 41–58. <https://doi.org/10.1016/j.jenvman.2016.08.054>.
- (75) Khan, S. A.; Rashmi; Hussain, M. Z.; Prasad, S.; Banerjee, U. C. Prospects of Biodiesel Production from Microalgae in India. *Renewable and Sustainable Energy Reviews* **2009**, *13* (9), 2361–2372. <https://doi.org/10.1016/j.rser.2009.04.005>.
- (76) Greenwell, H. C.; Laurens, L. M. L.; Shields, R. J.; Lovitt, R. W.; Flynn, K. J. Placing Microalgae on the Biofuels Priority List: A Review of the

- Technological Challenges. *J R Soc Interface* **2010**, *7* (46), 703–726. <https://doi.org/10.1098/rsif.2009.0322>.
- (77) Francisco, É. C.; Neves, D. B.; Jacob-Lopes, E.; Franco, T. T. Microalgae as Feedstock for Biodiesel Production: Carbon Dioxide Sequestration, Lipid Production and Biofuel Quality. *Journal of Chemical Technology and Biotechnology* **2010**, *85* (3), 395–403. <https://doi.org/10.1002/jctb.2338>.
- (78) Vanthoor-Koopmans, M.; Wijffels, R. H.; Barbosa, M. J.; Eppink, M. H. M. Biorefinery of Microalgae for Food and Fuel. *Bioresour Technol* **2013**, *135*, 142–149. <https://doi.org/10.1016/j.biortech.2012.10.135>.
- (79) Cheah, W. Y.; Show, P. L.; Chang, J. S.; Ling, T. C.; Juan, J. C. Biosequestration of Atmospheric CO₂ and Flue Gas-Containing CO₂ by Microalgae. *Bioresour Technol* **2015**, *184*, 190–201. <https://doi.org/10.1016/j.biortech.2014.11.026>.
- (80) Gimpel, J. A.; Henríquez, V.; Mayfield, S. P. In Metabolic Engineering of Eukaryotic Microalgae: Potential and Challenges Come with Great Diversity. *Front Microbiol* **2015**, *6* (DEC), 1–14. <https://doi.org/10.3389/fmicb.2015.01376>.
- (81) Chini Zittelli, G.; Rodolfi, L.; Bassi, N.; Biondi, N.; Tredici, M. R. Photobioreactors for Microalgae Biofuel Production. In *Algae for Biofuels and Energy*; Borowitzka, M. A., Moheimani, N. R., Eds.; Springer, Dordrecht., 2013; pp 115–131. <https://doi.org/10.1007/978-94-007-5479-9>.
- (82) Pandey, A.; Lee, D. J.; Chisti, Y.; Soccol, C. R. *Biofuels From Algae Biofuels From*; Elsevier, Amsterdam, 2014.
- (83) Adesanya, V. O.; Cadena, E.; Scott, S. A.; Smith, A. G. Life Cycle Assessment on Microalgal Biodiesel Production Using a Hybrid Cultivation System. *Bioresour Technol* **2014**, *163*, 343–355. <https://doi.org/10.1016/j.biortech.2014.04.051>.
- (84) Torzillo, G.; Pushparaj, B.; Masojidek, J.; Vonshak, A. Biological Constraints in Algal Biotechnology. *Biotechnology and Bioprocess Engineering* **2003**, *8* (6), 338–348. <https://doi.org/10.1007/BF02949277>.
- (85) Yadav, G.; Sen, R. Microalgal Green Refinery Concept for Biosequestration of Carbon-Dioxide Vis-à-Vis Wastewater Remediation and Bioenergy Production: Recent Technological Advances in Climate Research. *Journal of CO₂ Utilization* **2017**, *17*, 188–206. <https://doi.org/10.1016/j.jcou.2016.12.006>.

- (86) De Vree, J. H.; Bosma, R.; Janssen, M.; Barbosa, M. J.; Wijffels, R. H. Comparison of Four Outdoor Pilot-Scale Photobioreactors. *Biotechnol Biofuels* **2015**, *8* (1), 1–12. <https://doi.org/10.1186/s13068-015-0400-2>.
- (87) Slade, R.; Bauen, A. Micro-Algae Cultivation for Biofuels: Cost, Energy Balance, Environmental Impacts and Future Prospects. *Biomass Bioenergy* **2013**, *53* (0), 29–38. <https://doi.org/10.1016/j.biombioe.2012.12.019>.
- (88) Weise, T.; Reinecke, J. M.; Schuster, S.; Pfaff, M. Optimizing Turbidostatic Microalgal Biomass Productivity: A Combined Experimental and Coarse-Grained Modelling Approach. *Algal Res* **2019**, *39*. <https://doi.org/10.1016/j.algal.2019.101439>.
- (89) Solimeno, A.; Gabriel, F.; García, J. Mechanistic Model for Design, Analysis, Operation and Control of Microalgae Cultures: Calibration and Application to Tubular Photobioreactors. *Algal Res* **2017**, *21*, 236–246. <https://doi.org/10.1016/j.algal.2016.11.023>.
- (90) del Rio-Chanona, E. A.; Wagner, J. L.; Ali, H.; Fiorelli, F.; Zhang, D.; Hellgardt, K. Deep Learning-Based Surrogate Modeling and Optimization for Microalgal Biofuel Production and Photobioreactor Design. *AIChE Journal* **2019**, *65* (3), 915–923. <https://doi.org/10.1002/aic.16473>.
- (91) Vasile, N. S.; Cordara, A.; Usai, G.; Re, A. Computational Analysis of Dynamic Light Exposure of Unicellular Algal Cells in a Flat-Panel Photobioreactor to Support Light-Induced CO₂ Bioprocess Development. *Front Microbiol* **2021**, *12*. <https://doi.org/10.3389/fmicb.2021.639482>.
- (92) Tan, C. H.; Tan, X.; Ho, S. H.; Lam, S. S.; Show, P. L.; Nguyen, T. H. P. Conceptual Design of a Hybrid Thin Layer Cascade Photobioreactor for Microalgal Biodiesel Synthesis. *Int J Energy Res* **2020**, *44* (12), 9757–9771. <https://doi.org/10.1002/er.5699>.
- (93) Chiaramonti, D.; Prussi, M.; Casini, D.; Tredici, M. R.; Rodolfi, L.; Bassi, N.; Zittelli, G. C.; Bondioli, P. Review of Energy Balance in Raceway Ponds for Microalgae Cultivation: Re-Thinking a Traditional System Is Possible. *Appl Energy* **2013**, *102*, 101–111. <https://doi.org/10.1016/j.apenergy.2012.07.040>.
- (94) Yadav, G.; Karemore, A.; Dash, S. K.; Sen, R. Performance Evaluation of a Green Process for Microalgal CO₂ Sequestration in Closed Photobioreactor Using Flue Gas Generated In-Situ. *Bioresour Technol* **2015**, *191*, 399–406. <https://doi.org/10.1016/j.biortech.2015.04.040>.

- (95) Chen, Z.; Jiang, Z.; Zhang, X.; Zhang, J. Numerical and Experimental Study on the CO₂ Gas-Liquid Mass Transfer in Flat-Plate Airlift Photobioreactor with Different Baffles. *Biochem Eng J* **2016**, *106*, 129–138. <https://doi.org/10.1016/j.bej.2015.11.011>.
- (96) Li, J.; Stamato, M.; Velliou, E.; Jeffryes, C.; Agathos, S. N. Design and Characterization of a Scalable Airlift Flat Panel Photobioreactor for Microalgae Cultivation. *J Appl Phycol* **2014**, *27* (1), 75–86. <https://doi.org/10.1007/s10811-014-0335-1>.
- (97) Rodolfi, L.; Zittelli, G. C.; Bassi, N.; Padovani, G.; Biondi, N.; Bonini, G.; Tredici, M. R. Microalgae for Oil: Strain Selection, Induction of Lipid Synthesis and Outdoor Mass Cultivation in a Low-Cost Photobioreactor. *Biotechnol Bioeng* **2009**, *102* (1), 100–112. <https://doi.org/10.1002/bit.22033>.
- (98) Estrada-Graf, A.; Hernández, S.; Morales, M. Biomitigation of CO₂ from Flue Gas by *Scenedesmus Obtusiusculus* AT-UAM Using a Hybrid Photobioreactor Coupled to a Biomass Recovery Stage by Electro-Coagulation-Flotation. *Environmental Science and Pollution Research* **2020**. <https://doi.org/10.1007/s11356-020-08240-2>.
- (99) Reyna-Velarde, R.; Cristiani-Urbina, E.; Hernández-Melchor, D. J.; Thalasso, F.; Cañizares-Villanueva, R. O. Hydrodynamic and Mass Transfer Characterization of a Flat-Panel Airlift Photobioreactor with High Light Path. *Chemical Engineering and Processing: Process Intensification* **2010**, *49* (1), 97–103. <https://doi.org/10.1016/j.cep.2009.11.014>.
- (100) Massart, A.; Mirisola, A.; Lupant, D.; Thomas, D.; Hantson, A. L. Experimental Characterization and Numerical Simulation of the Hydrodynamics in an Airlift Photobioreactor for Microalgae Cultures. *Algal Res* **2014**, *6* (PB), 210–217. <https://doi.org/10.1016/j.algal.2014.07.003>.
- (101) López-Rosales, L.; Sánchez-Mirón, A.; Contreras-Gómez, A.; García-Camacho, F.; Battaglia, F.; Zhao, L.; Molina-Grima, E. Characterization of Bubble Column Photobioreactors for Shear-Sensitive Microalgae Culture. *Bioresour Technol* **2019**, *275*, 1–9. <https://doi.org/10.1016/j.biortech.2018.12.009>.
- (102) Jorquera, O.; Kiperstok, A.; Sales, E. A.; Embiruçu, M.; Ghirardi, M. L. Comparative Energy Life-Cycle Analyses of Microalgal Biomass Production in Open Ponds and Photobioreactors. *Bioresour Technol* **2010**, *101* (4), 1406–1413. <https://doi.org/10.1016/j.biortech.2009.09.038>.

- (103) Stanier, R. Y.; Kunisawa, R.; Mandel, M.; Cohen-Bazire, G. Purification and Properties of Unicellular Blue-Green Algae (Order Chroococcales). *Bacteriol Rev* **1971**, *35* (2), 171–205. <https://doi.org/10.1128/membr.35.2.171-205.1971>.
- (104) Perin, G.; Simionato, D.; Bellan, A.; Carone, M.; Occhipinti, A.; Maffei, M. E.; Morosinotto, T. Cultivation in Industrially Relevant Conditions Has a Strong Influence on Biological Properties and Performances of Nannochloropsis Gaditana Genetically Modified Strains. *Algal Res* **2017**, *28* (June), 88–99. <https://doi.org/10.1016/j.algal.2017.10.013>.
- (105) Lim, Y. A.; Chong, M. N.; Foo, S. C.; Ilankoon, I. M. S. K. Analysis of Direct and Indirect Quantification Methods of CO₂ Fixation via Microalgae Cultivation in Photobioreactors: A Critical Review. *Renewable and Sustainable Energy Reviews* **2021**, *137* (April 2020), 110579. <https://doi.org/10.1016/j.rser.2020.110579>.
- (106) Yang, C.; Mao, Z.-S. Airlift Loop Reactors. In *Numerical Simulation of Multiphase Reactors with Continuous Liquid Phase*; Yang, C., Zai-Sha, M., Eds.; 2014; pp 153–229. <https://doi.org/10.1016/b978-0-08-099919-7.00004-4>.
- (107) Chisti, Y. M. *Airlift Bioreactors*; Elsevier: London, 1989.
- (108) Leupold, M.; Hindersin, S.; Kerner, M.; Hanelt, D. The Effect of Discontinuous Airlift Mixing in Outdoor Flat Panel Photobioreactors on Growth of Scenedesmus Obliquus. *Bioprocess Biosyst Eng* **2013**, *36* (11), 1653–1663. <https://doi.org/10.1007/s00449-013-0939-x>.
- (109) Sousa, C.; de Winter, L.; Janssen, M.; Vermuë, M. H.; Wijffels, R. H. Growth of the Microalgae Nannochloris Oleoabundans at High Partial Oxygen Pressures and Sub-Saturating Light Intensity. *Bioresour Technol* **2012**, *104*, 565–570. <https://doi.org/10.1016/j.biortech.2011.10.048>.
- (110) Kliphuis, A. M. J.; de Winter, L.; Vejrazka, C.; Martens, D. E.; Janssen, M.; Wijffels, R. H. Photosynthetic Efficiency of Chlorella Sorokiniana in a Turbulently Mixed Short Light-Path Photobioreactor. *Biotechnol Prog* **2010**, *26* (3), 687–696. <https://doi.org/10.1002/btpr.379>.
- (111) Tham, P. E.; Ng, Y. J.; Vadivelu, N.; Lim, H. R.; Khoo, K. S.; Chew, K. W.; Show, P. L. Sustainable Smart Photobioreactor for Continuous Cultivation of Microalgae Embedded with Internet of Things. *Bioresour Technol* **2022**, *346*. <https://doi.org/10.1016/j.biortech.2021.126558>.

- (112) Wang, K.; Khoo, K. S.; Leong, H. Y.; Nagarajan, D.; Chew, K. W.; Ting, H. Y.; Selvarajoo, A.; Chang, J. S.; Show, P. L. How Does the Internet of Things (IoT) Help in Microalgae Biorefinery? *Biotechnology Advances*. Elsevier Inc. January 1, 2022. <https://doi.org/10.1016/j.biotechadv.2021.107819>.
- (113) Belohlav, V.; Uggetti, E.; García, J.; Jirout, T.; Kratky, L.; Díez-Montero, R. Assessment of Hydrodynamics Based on Computational Fluid Dynamics to Optimize the Operation of Hybrid Tubular Photobioreactors. *J Environ Chem Eng* **2021**, *9* (5). <https://doi.org/10.1016/j.jece.2021.105768>.
- (114) Wang, L.; Wang, Q.; Zhao, R.; Tao, Y.; Ying, K. Z.; Mao, X. Z. Novel Flat-Plate Photobioreactor with Inclined Baffles and Internal Structure Optimization to Improve Light Regime Performance. *ACS Sustain Chem Eng* **2021**, *9* (4), 1550–1558. <https://doi.org/10.1021/acssuschemeng.0c06109>.
- (115) Hinterholz, C. L.; Trigueros, D. E. G.; Módenes, A. N.; Borba, C. E.; Scheufele, F. B.; Schuelter, A. R.; Kroumov, A. D. Computational Fluid Dynamics Applied for the Improvement of a Flat-Plate Photobioreactor towards High-Density Microalgae Cultures. *Biochem Eng J* **2019**, *151*. <https://doi.org/10.1016/j.bej.2019.107257>.
- (116) Laifa, R.; Morchain, J.; Barna, L.; Guiraud, P. A Numerical Framework to Predict the Performances of a Tubular Photobioreactor from Operating and Sunlight Conditions. *Algal Res* **2021**, *60* (102550).
- (117) Zhang, Q.; Yu, Z.; Jin, S.; Liu, C.; Li, Y.; Guo, D.; Hu, M.; Ruan, R.; Liu, Y. Role of Surface Roughness in the Algal Short-Term Cell Adhesion and Long-Term Biofilm Cultivation under Dynamic Flow Condition. *Algal Res* **2020**, *46*. <https://doi.org/10.1016/j.algal.2019.101787>.
- (118) Frungieri, G.; Carone, M.; Riggio, V.; Buffo, A.; Vanni, M.; Zanetti, M. Numerical Modelling of a Lab-Scale Reactor for Microalgae Growth. *Chem Eng Trans* **2022**, *92*, 127–132. <https://doi.org/10.3303/CET2292022>.
- (119) Fernández del Olmo, P.; Acién, F. G.; Fernández-Sevilla, J. M. Productivity Analysis in Tubular Photobioreactors Using a Dynamic Photosynthesis Model Coupled to Computational Fluid Dynamics Particle Tracking. *Bioresour Technol* **2022**, *344*. <https://doi.org/10.1016/j.biortech.2021.126277>.
- (120) Anye Cho, B.; Grobler, E.; William McClelland Pott, R.; Antonio del Río Chanona, E.; Zhang, D. A CFD Coupled Photo-Bioreactive Transport

Modelling of Tubular Photobioreactor Mixed by Peristaltic Pump. *Chem Eng Sci* **2023**, 270. <https://doi.org/10.1016/j.ces.2023.118525>.

- (121) Carvalho, A. P.; Silva, S. O.; Baptista, J. M.; Malcata, F. X. Light Requirements in Microalgal Photobioreactors: An Overview of Biophotonic Aspects. *Applied Microbiology and Biotechnology*. March 2011, pp 1275–1288. <https://doi.org/10.1007/s00253-010-3047-8>.
- (122) Baer, S.; Heining, M.; Schwerna, P.; Buchholz, R.; Hübner, H. Optimization of Spectral Light Quality for Growth and Product Formation in Different Microalgae Using a Continuous Photobioreactor. *Algal Res* **2016**, 14, 109–115. <https://doi.org/10.1016/j.algal.2016.01.011>.
- (123) Borowitzka, M. A. High-Value Products from Microalgae-Their Development and Commercialisation. *Journal of Applied Phycology*. June 2013, pp 743–756. <https://doi.org/10.1007/s10811-013-9983-9>.
- (124) Koller, M.; Muhr, A.; Braunegg, G. Microalgae as Versatile Cellular Factories for Valued Products. *Algal Research*. Elsevier B.V. October 1, 2014, pp 52–63. <https://doi.org/10.1016/j.algal.2014.09.002>.
- (125) Vadiveloo, A.; Moheimani, N. R.; Cosgrove, J. J.; Bahri, P. A.; Parlevliet, D. Effect of Different Light Spectra on the Growth and Productivity of Acclimated *Nannochloropsis* Sp. (Eustigmatophyceae). *Algal Res* **2015**, 8, 121–127. <https://doi.org/10.1016/j.algal.2015.02.001>.
- (126) Han, P. P.; Shen, S. G.; Wang, H. Y.; Sun, Y.; Dai, Y. J.; Jia, S. R. Comparative Metabolomic Analysis of the Effects of Light Quality on Polysaccharide Production of *Cyanobacterium Nostoc Flagelliforme*. *Algal Res* **2015**, 9, 143–150. <https://doi.org/10.1016/j.algal.2015.02.019>.
- (127) Carone, M.; Alpe, D.; Costantino, V.; Derossi, C.; Occhipinti, A.; Zanetti, M.; Riggio, V. A. Design and Characterization of a New Pressurized Flat Panel Photobioreactor for Microalgae Cultivation and CO₂ Bio-Fixation. *Chemosphere* **2022**, 307. <https://doi.org/10.1016/j.chemosphere.2022.135755>.
- (128) Maluta, F.; Buffo, A.; Marchisio, D.; Montante, G.; Paglianti, A.; Vanni, M. Effect of Turbulent Kinetic Energy Dissipation Rate on the Prediction of Droplet Size Distribution in Stirred Tanks. *International Journal of Multiphase Flow* **2021**, 136, 103547. <https://doi.org/10.1016/j.ijmultiphaseflow.2020.103547>.

- (129) Faria, R.; Ferreira, A. D.; Lopes, A. M. G.; Sousa, A. C. M. Modeling of Turbulent Flows in Rectangular Ducts Using Openfoam®. In *OpenFOAM - Selected Papers of the 11th Workshop*; Springer, 2019; pp 325–340. https://doi.org/10.1007/978-3-319-60846-4_24.
- (130) White, F. M. *Viscous Fluid Flow*, 3rd ed.; McGraw-Hill Higher Education, 2006.
- (131) Ranade, V. V. *Computational Flow Modeling for Chemical Reactor Engineering*, 1st ed.; Academic Press, 2001.
- (132) Schlichting, H. *Boundary Layer Theory*, 7th ed.; McGraw-Hill, 1979.
- (133) Hinze, J. O. Experimental Investigation on Secondary Currents in the Turbulent Flow through a Straight Conduit. *Applied Scientific Research* **1973**, *28* (1), 453–465. <https://doi.org/10.1007/BF00413083>.
- (134) Melling, A.; Whitelaw, J. H. Turbulent Flow in a Rectangular Duct. *J Fluid Mech* **1976**, *78* (2), 289–315. <https://doi.org/10.1017/S0022112076002450>.
- (135) Bradshaw, P. Turbulent Secondary Flows. *Annu Rev Fluid Mech* **1987**, *19* (1), 53–74. <https://doi.org/10.1146/annurev.fl.19.010187.000413>.
- (136) Yao, J.; Zhao, Y.; Fairweather, M. Numerical Simulation of Turbulent Flow through a Straight Square Duct. *Appl Therm Eng* **2015**, *91*, 800–811. <https://doi.org/10.1016/j.applthermaleng.2015.08.065>.
- (137) Stankovic, B.; Belosevic, S.; Crnomarkovic, N.; Stojanovic, A.; Tomanovic, I.; Milicevic, A. Specific Aspects of Turbulent Flow in Rectangular Ducts. *Thermal Science* **2017**, *21* (suppl. 3), 663–678. <https://doi.org/10.2298/TSCI160201189S>.
- (138) Orlandi, P.; Pirozzoli, S. Transitional and Turbulent Flows in Rectangular Ducts: Budgets and Projection in Principal Mean Strain Axes. *Journal of Turbulence* **2020**, *21* (5–6), 286–310. <https://doi.org/10.1080/14685248.2020.1779276>.
- (139) Pope, S. B. *Turbulent Flows*; Cambridge University Press, 2000.
- (140) Allen, M. B. Studies with Cyanidium Caldarium, an Anomalously Pigmented Chlorophyte. *Arch Mikrobiol* **1959**, *32*, 270–277.
- (141) Abiusi, F.; Trompetter, E.; Hoenink, H.; Wijffels, R. H.; Janssen, M. Autotrophic and Mixotrophic Biomass Production of the Acidophilic

- Galdieria Sulphuraria ACUF 64. *Algal Res* **2021**, 60. <https://doi.org/10.1016/j.algal.2021.102513>.
- (142) Pinto, G.; Ciniglia, C.; Cascone, C.; Pollio, A. A. Species Composition of Cyanidiales Assemblages in Pisciarelli (Campi Flegrei, Italy) and Description of Galdieria Phlegrea SP. NOV. In *Algae and Cyanobacteria in Extreme Environments. Cellular Origin, Life in Extreme Habitats and Astrobiology*; Seckbach, J., Ed.; Springer: Dordrecht, 2007; Vol. 11, pp 487–502. https://doi.org/https://doi.org/10.1007/978-1-4020-6112-7_26.
- (143) Graziani, G.; Schiavo, S.; Nicolai, M. A.; Buono, S.; Fogliano, V.; Pinto, G.; Pollio, A. Microalgae as Human Food: Chemical and Nutritional Characteristics of the Thermo-Acidophilic Microalga Galdieria Sulphuraria. *Food Funct* **2013**, 4 (1), 144–152. <https://doi.org/10.1039/c2fo30198a>.
- (144) Oesterhelt, C.; Schmäzlin, E.; Schmitt, J. M.; Lokstein, H. Regulation of Photosynthesis in the Unicellular Acidophilic Red Alga Galdieria Sulphuraria. *Plant Journal* **2007**, 51 (3), 500–511. <https://doi.org/10.1111/j.1365-313X.2007.03159.x>.
- (145) Sloth, J. K.; Wiebe, M. G.; Eriksen, N. T. Accumulation of Phycocyanin in Heterotrophic and Mixotrophic Cultures of the Acidophilic Red Alga Galdieria Sulphuraria. *Enzyme Microb Technol* **2006**, 38 (1–2), 168–175. <https://doi.org/10.1016/j.enzmictec.2005.05.010>.
- (146) Selvaratnam, T.; Pegallapati, A. K.; Montelya, F.; Rodriguez, G.; Nirmalakhandan, N. Bioresource Technology Evaluation of a Thermo-Tolerant Acidophilic Alga , Galdieria Sulphuraria , for Nutrient Removal from Urban Wastewaters. *Bioresour Technol* **2014**, 156, 395–399. <https://doi.org/10.1016/j.biortech.2014.01.075>.
- (147) Carbone, D. A.; Olivieri, G.; Pollio, A.; Melkonian, M. Comparison of Galdieria Growth and Photosynthetic Activity in Different Culture Systems. *AMB Express* **2020**, 10 (1). <https://doi.org/10.1186/s13568-020-01110-7>.
- (148) Atta, M.; Idris, A.; Bukhari, A.; Wahidin, S. Intensity of Blue LED Light: A Potential Stimulus for Biomass and Lipid Content in Fresh Water Microalgae Chlorella Vulgaris. *Bioresour Technol* **2013**, 148, 373–378. <https://doi.org/10.1016/j.biortech.2013.08.162>.
- (149) Baba, M.; Kikuta, F.; Suzuki, I.; Watanabe, M. M.; Shiraiwa, Y. Wavelength Specificity of Growth, Photosynthesis, and Hydrocarbon Production in the Oil-Producing Green Alga Botryococcus Braunii. *Bioresour Technol* **2012**, 109, 266–270. <https://doi.org/10.1016/j.biortech.2011.05.059>.

- (150) Wang, S. K.; Stiles, A. R.; Guo, C.; Liu, C. Z. Microalgae Cultivation in Photobioreactors: An Overview of Light Characteristics. *Engineering in Life Sciences*. Wiley-VCH Verlag November 1, 2014, pp 550–559. <https://doi.org/10.1002/elsc.201300170>.
- (151) Matthijs, H. C. P.; Balke, H.; Van Hes, U. M.; A Kroon, B. M.; Mur, L. R.; Binot, R. A. *Application of Light-Emitting Diodes in Bioreactors: Flashing Light Effects and Energy Economy in Algal Culture (Ch/Ore//a Pyrenoidosa)*; John Wiley & Sons, Inc, 1996; Vol. 50.
- (152) Mohsenpour, S. F.; Willoughby, N. Luminescent Photobioreactor Design for Improved Algal Growth and Photosynthetic Pigment Production through Spectral Conversion of Light. *Bioresour Technol* **2013**, *142*, 147–153. <https://doi.org/10.1016/j.biortech.2013.05.024>.
- (153) Das, P.; Lei, W.; Aziz, S. S.; Obbard, J. P. Enhanced Algae Growth in Both Phototrophic and Mixotrophic Culture under Blue Light. *Bioresour Technol* **2011**, *102* (4), 3883–3887. <https://doi.org/10.1016/j.biortech.2010.11.102>.
- (154) Teo, C. L.; Atta, M.; Bukhari, A.; Taisir, M.; Yusuf, A. M.; Idris, A. Enhancing Growth and Lipid Production of Marine Microalgae for Biodiesel Production via the Use of Different LED Wavelengths. *Bioresour Technol* **2014**, *162*, 38–44. <https://doi.org/10.1016/j.biortech.2014.03.113>.
- (155) Niizawa, I.; Leonardi, R. J.; Irazoqui, H. A.; Heinrich, J. M. Light Wavelength Distribution Effects on the Growth Rate of *Scenedesmus Quadricauda*. *Biochem Eng J* **2017**, *126*, 126–134. <https://doi.org/10.1016/j.bej.2016.09.006>.
- (156) Leonardi, R. J.; Niizawa, I.; Irazoqui, H. A.; Heinrich, J. M. Modeling and Simulation of the Influence of Fractions of Blue and Red Light on the Growth of the Microalga *Scenedesmus Quadricauda*. *Biochem Eng J* **2018**, *129*, 16–25. <https://doi.org/10.1016/j.bej.2017.10.014>.
- (157) Kula, M.; Rys, M.; Mozdzeń, K.; Skoczowski, A. Metabolic Activity, the Chemical Composition of Biomass and Photosynthetic Activity of *Chlorella Vulgaris* under Different Light Spectra in Photobioreactors. *Eng Life Sci* **2014**, *14* (1), 57–67. <https://doi.org/10.1002/elsc.201200184>.
- (158) Dikicioglu, D.; Wood, V.; Rutherford, K. M.; McDowall, M. D.; Oliver, S. G. Improving Functional Annotation for Industrial Microbes: A Case Study with *Pichia Pastoris*. *Trends in Biotechnology*. Elsevier Ltd 2014, pp 396–399. <https://doi.org/10.1016/j.tibtech.2014.05.003>.

- (159) Eriksen, N. T. Production of Phycocyanin - A Pigment with Applications in Biology, Biotechnology, Foods and Medicine. *Applied Microbiology and Biotechnology*. August 2008, pp 1–14. <https://doi.org/10.1007/s00253-008-1542-y>.
- (160) Jordan, P.; Fromme², P.; Witt², H. T.; Klukas, O.; Saenger, W.; Krauß, N. Three-Dimensional Structure of Cyanobacterial Photosystem I at 2.5 Å Resolution. *Nature* **2001**, 411.
- (161) Stadnichuk, I. N.; Bulychev, A. A.; Lukashev, E. P.; Sinetova, M. P.; Khristin, M. S.; Johnson, M. P.; Ruban, A. V. Far-Red Light-Regulated Efficient Energy Transfer from Phycobilisomes to Photosystem i in the Red Microalga *Galdieria Sulphuraria* and Photosystems-Related Heterogeneity of Phycobilisome Population. *Biochim Biophys Acta Bioenerg* **2011**, 1807 (2), 227–235. <https://doi.org/10.1016/j.bbabi.2010.10.018>.
- (162) Marquardt, J. Effects of Carotenoid-Depletion on the Photosynthetic Apparatus of a *Galdieria Sulphuraria* (Rhodophyta) Strain That Retains Its Photosynthetic Apparatus in the Dark. *J Plant Physiol* **1998**, 152 (4–5), 372–380. [https://doi.org/10.1016/S0176-1617\(98\)80250-2](https://doi.org/10.1016/S0176-1617(98)80250-2).
- (163) Carfagna, S.; Bottone, C.; Cataletto, P. R.; Petriccione, M.; Pinto, G.; Salbitani, G.; Vona, V.; Pollio, A.; Ciniglia, C. Impact of Sulfur Starvation in Autotrophic and Heterotrophic Cultures of the Extremophilic Microalga *Galdieria Phlegrea* (Cyanidiophyceae). *Plant Cell Physiol* **2016**, 57 (9), 1890–1898. <https://doi.org/10.1093/pcp/pcw112>.
- (164) Abiusi, F.; Moñino Fernández, P.; Canziani, S.; Janssen, M.; Wijffels, R. H.; Barbosa, M. Mixotrophic Cultivation of *Galdieria Sulphuraria* for C-Phycocyanin and Protein Production. *Algal Res* **2022**, 61. <https://doi.org/10.1016/j.algal.2021.102603>.
- (165) Wan, M.; Wang, Z.; Zhang, Z.; Wang, J.; Li, S.; Yu, A.; Li, Y. A Novel Paradigm for the High-Efficient Production of Phycocyanin from *Galdieria Sulphuraria*. *Bioresour Technol* **2016**, 218, 272–278. <https://doi.org/10.1016/j.biortech.2016.06.045>.
- (166) Canelli, G.; Abiusi, F.; Vidal Garcia, A.; Canziani, S.; Mathys, A. Amino Acid Profile and Protein Bioaccessibility of Two *Galdieria Sulphuraria* Strains Cultivated Autotrophically and Mixotrophically in Pilot-Scale Photobioreactors. *Innovative Food Science and Emerging Technologies* **2023**, 84. <https://doi.org/10.1016/j.ifset.2023.103287>.

- (167) Blanken, W.; Magalhães, A.; Sebestyén, P.; Rinzema, A.; Wijffels, R. H.; Janssen, M. Microalgal Biofilm Growth under Day-Night Cycles. *Algal Res* **2017**, *21*, 16–26. <https://doi.org/10.1016/j.algal.2016.11.006>.
- (168) de Mooij, T.; Janssen, M.; Cerezo-Chinarro, O.; Mussgnug, J. H.; Kruse, O.; Ballottari, M.; Bassi, R.; Bujaldon, S.; Wollman, F. A.; Wijffels, R. H. Antenna Size Reduction as a Strategy to Increase Biomass Productivity: A Great Potential Not yet Realized. *J Appl Phycol* **2015**, *27* (3), 1063–1077. <https://doi.org/10.1007/s10811-014-0427-y>.
- (169) Graverholt, O. S.; Eriksen, N. T. Heterotrophic High-Cell-Density Fed-Batch and Continuous-Flow Cultures of *Galdieria Sulphuraria* and Production of Phycocyanin. *Appl Microbiol Biotechnol* **2007**, *77* (1), 69–75. <https://doi.org/10.1007/s00253-007-1150-2>.
- (170) Zijffers, J. W. F.; Schippers, K. J.; Zheng, K.; Janssen, M.; Tramper, J.; Wijffels, R. H. Maximum Photosynthetic Yield of Green Microalgae in Photobioreactors. *Marine Biotechnology* **2010**, *12* (6), 708–718. <https://doi.org/10.1007/s10126-010-9258-2>.
- (171) Suparmaniam, U.; Lam, M. K.; Uemura, Y.; Lim, J. W.; Lee, K. T.; Shuit, S. H. Insights into the Microalgae Cultivation Technology and Harvesting Process for Biofuel Production: A Review. *Renewable and Sustainable Energy Reviews*. Elsevier Ltd November 1, 2019. <https://doi.org/10.1016/j.rser.2019.109361>.
- (172) Batan, L.; Quinn, J. C.; Bradley, T. H. Analysis of Water Footprint of a Photobioreactor Microalgae Biofuel Production System from Blue, Green and Lifecycle Perspectives. *Algal Res* **2013**, *2* (3), 196–203. <https://doi.org/10.1016/j.algal.2013.02.003>.
- (173) Barros, A. I.; Gonçalves, A. L.; Simões, M.; Pires, J. C. M. Harvesting Techniques Applied to Microalgae: A Review. *Renewable and Sustainable Energy Reviews*. Elsevier Ltd 2015, pp 1489–1500. <https://doi.org/10.1016/j.rser.2014.09.037>.
- (174) *Italian Legislative Decree No. 152 Approving the Code on the Environment*; FAO, FAOLEX. <http://faolex.fao.org/docs/pdf/ita64213.pdf>.
- (175) Carone, M.; Frungieri, G.; Costamagna, L.; Zanetti, M.; Vanni, M.; Riggio, V. A. Advanced Design and Characterization of a Flat Panel Photobioreactor Equipped with a Customizable Light-Emitting Diode Lighting System. *ACS Sustain Chem Eng* **2024**, *12* (7), 2550–2562. <https://doi.org/10.1021/acssuschemeng.3c05176>.

- (176) Ricceri, F.; Malaguti, M.; Derossi, C.; Zanetti, M.; Riggio, V.; Tiraferri, A. Microalgae Biomass Concentration and Reuse of Water as New Cultivation Medium Using Ceramic Membrane Filtration. *Chemosphere* **2022**, *307*, 135724. <https://doi.org/10.1016/j.chemosphere.2022.135724>.
- (177) Malaguti, M.; Craveri, L.; Ricceri, F.; Riggio, V.; Zanetti, M.; Tiraferri, A. Dewatering of *Scenedesmus Obliquus* Cultivation Substrate with Microfiltration: Potential and Challenges for Water Reuse and Effective Harvesting. *Engineering* **2023**. <https://doi.org/10.1016/j.eng.2023.07.010>.
- (178) Kursar, T. A.; Alberte, R. S. *Photosynthetic Unit Organization in a Red Alga' RELATIONSHIPS BETWEEN LIGHT-HARVESTING PIGMENTS AND REACTION CENTERS*; 1983; Vol. 72.
- (179) Sha, J.; Lu, Z.; Ye, J.; Wang, G.; Hu, Q.; Chen, Y.; Zhang, X. The Inhibition Effect of Recycled *Scenedesmus Acuminatus* Culture Media: Influence of Growth Phase, Inhibitor Identification and Removal. *Algal Res* **2019**, *42*. <https://doi.org/10.1016/j.algal.2019.101612>.
- (180) Gerardo, M. L.; Zanain, M. A.; Lovitt, R. W. Pilot-Scale Cross-Flow Microfiltration of *Chlorella Minutissima*: A Theoretical Assessment of the Operational Parameters on Energy Consumption. *Chemical Engineering Journal* **2015**, *280*, 505–513. <https://doi.org/10.1016/j.cej.2015.06.026>.
- (181) Khan, S.; Das, P.; Abdulquadir, M.; Thaher, M.; Al-Ghasal, G.; Hafez Mohammed Kashem, A.; Faisal, M.; Sayadi, S.; Al-Jabri, H. Pilot-Scale Crossflow Ultrafiltration of Four Different Cell-Sized Marine Microalgae to Assess the Ultrafiltration Performance and Energy Requirements. *Sep Purif Technol* **2023**, *315*. <https://doi.org/10.1016/j.seppur.2023.123681>.
- (182) Najjar, Y. S. H.; Abu-Shamleh, A. Harvesting of Microalgae by Centrifugation for Biodiesel Production: A Review. *Algal Research*. Elsevier B.V. October 1, 2020. <https://doi.org/10.1016/j.algal.2020.102046>.
- (183) Coons, J. E.; Kalb, D. M.; Dale, T.; Marrone, B. L. Getting to Low-Cost Algal Biofuels: A Monograph on Conventional and Cutting-Edge Harvesting and Extraction Technologies. *Algal Res* **2014**, *6* (PB), 250–270. <https://doi.org/10.1016/j.algal.2014.08.005>.
- (184) Wang, H.; Zhang, Z.; Wan, M.; Wang, R.; Huang, J.; Zhang, K.; Guo, J.; Bai, W.; Li, Y. Comparative Study on Light Attenuation Models of *Galdieria Sulphuraria* for Efficient Production of Phycocyanin. *J Appl Phycol* **2020**, *32* (1), 165–174. <https://doi.org/10.1007/s10811-019-01982-8>.

Appendix

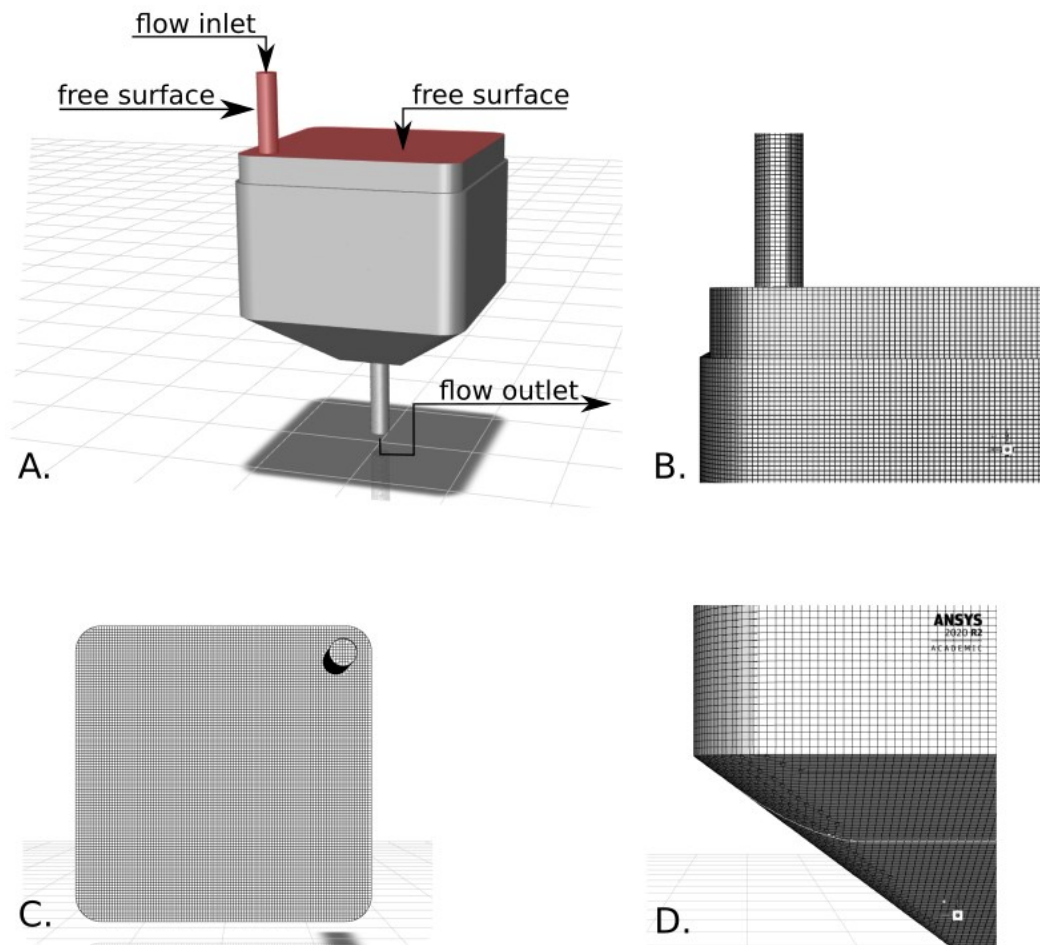


Figure A.1: Detailed view of the geometry of the mixing tank. A. Three-dimensional representation. The red-shaded surface are free surfaces, *i.e.*, liquid surfaces not bounded by walls. The top free surface has side length equal to 30 cm. The inlet and the outlet have diameter of 2.5 cm and 2.6 cm, respectively. B. Top side view including the inlet flow. C. View from the top. D. Bottom side view.

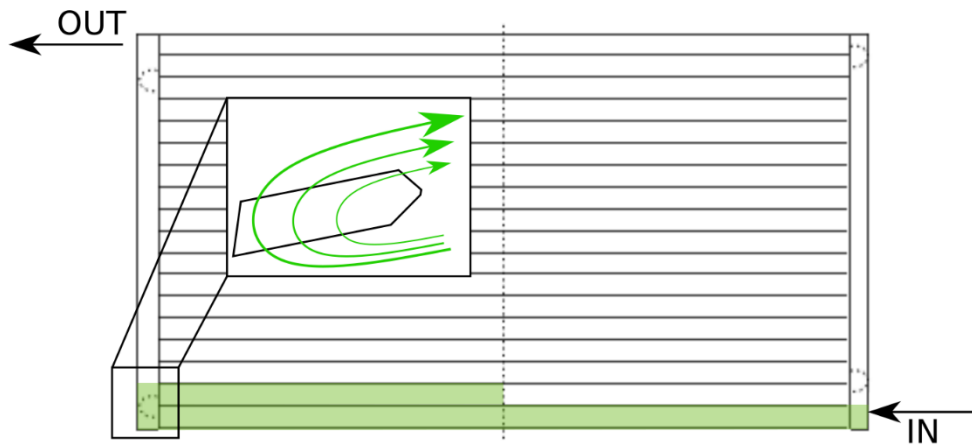


Figure A.2: Qualitative representation of the flat panel. The actual system is composed of 28 parallel channels. The cross section of each is 2 cm wide in the vertical direction, and 1.3 cm in the transversal direction. The geometry of the passage hole is shown in the inset. The green shaded region is the actual simulated volume.

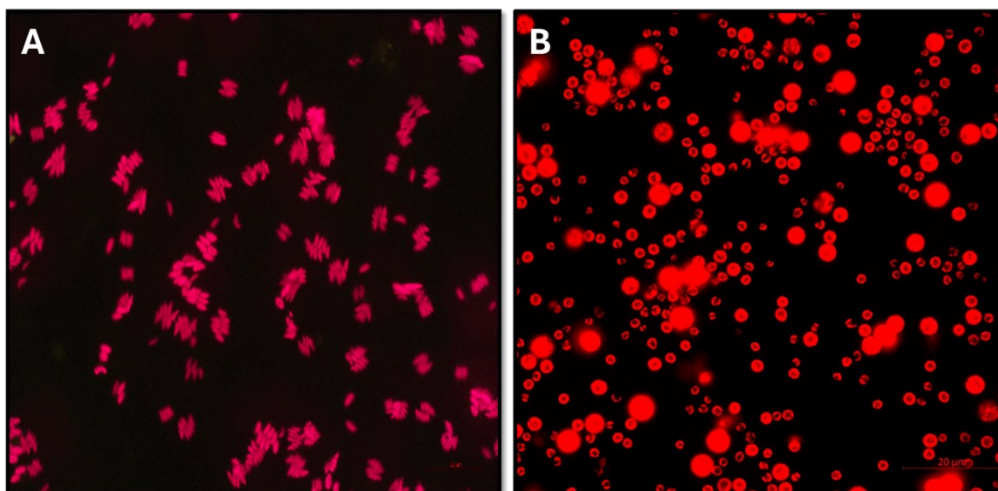


Figure A.3: Fluorescence microscopy images of *Acutodesmus obliquus* (A – 20X) and *G. sulphuraria* (B – 40X). Pictures were taken during the batch cultivations described in Chapter 3.

Table A.1: Product performances of LUXEON CZ Colors at current 350 mA and junction Temperature 85°C. (Reproduced from LUXEON CZ Color Line Datasheet, LUMILEDS).

Color	Dominant or Peak		Luminous Flux [<i>lm</i>] or	
	Wavelength Range ^[1] [<i>nm</i>]		Radiometric Power ^[2] [<i>mW</i>]	
	Minimum	Maximum	Minimum	Typical
Far-Red	720	750	150	200
Deep-Red	655	675	190	225
Red	624	634	20	31
Red-Orange	614	624	25	37
Amber	585	600	10	16
Green	520	540	80	99
Cyan	490	510	60	73
Blue	465	485	25	33
Royal Blue	440	460	360	425
Violet	420	430	400	458
White LEDs				
Nominal CCT	Luminous Flux [<i>lm</i>]		Typical Luminous Efficiency	
	Minimum	Typical	[<i>lm W⁻¹</i>]	
4000K	100	109	113	
5000K	100	109	113	

[1] Far-Red, Deep-Red, Royal Blue and Violet are binned by peak wavelength. All other colours are binned by dominant wavelength. [2] Far-Red, Deep-Red, Royal Blue and Violet are binned by radiometric power. All other colours are binned by luminous flux.

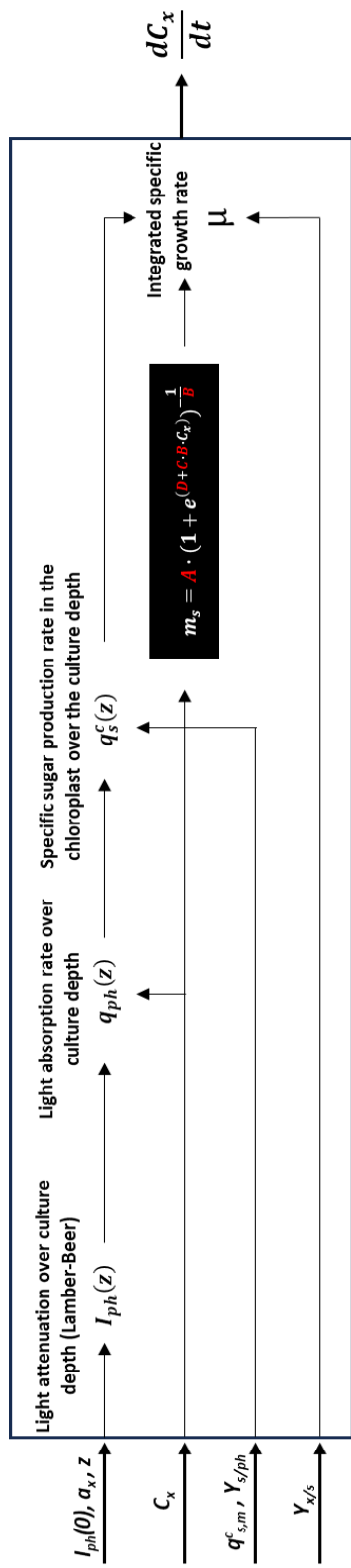


Figure A.4: Schematic diagram of the developed model. The parameters on the left arrows are the input parameters derived experimentally and/or from the literature. The white box shows the output of the intermediate equations as reported in Chapter 4 (Eq. 4.1 – 4.5). The black box shows the equation with the fitted parameters (in red) to retrieve the adaptive m_s as function of C_x . The final output of the model for batch cultivations is specified on the right arrow. The core Python scripts are available as annexes to this PhD thesis.